Master's thesis

NTNU
Norwegian University of Science and Technology
Faculty of Natural Sciences
Department of Physics

Anders Christian Mathisen

# Scanning Precession Electron Diffraction of Ferroelectric Polycrystalline h-$ErMnO_3$

Master's thesis in Nanotechnology
Supervisor: Antonius T. J. van Helvoort
June 2023

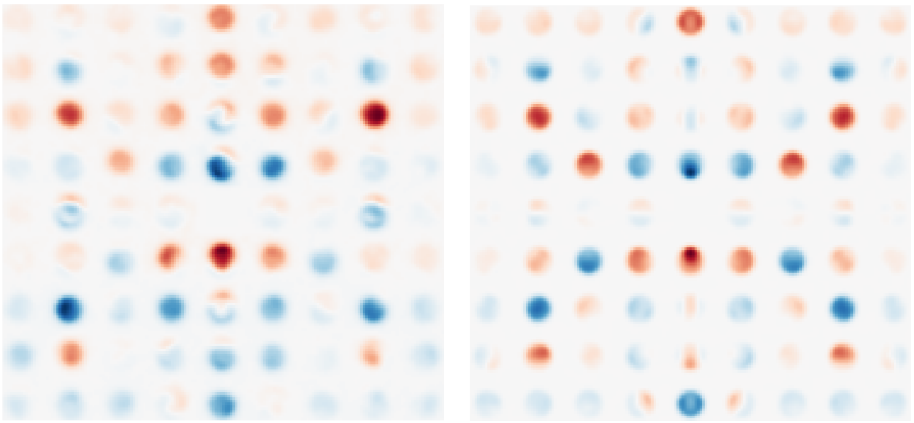

NTNU
Norwegian University of
Science and Technology

Anders Christian Mathisen

# Scanning Precession Electron Diffraction of Ferroelectric Polycrystalline h-$ErMnO_3$

Master's thesis in Nanotechnology
Supervisor: Antonius T. J. van Helvoort
June 2023

Norwegian University of Science and Technology
Faculty of Natural Sciences
Department of Physics

NTNU
Norwegian University of
Science and Technology

# Abstract

Ferroelectric domain walls have in recent years attracted attention as a candidate for novel 2D functional data-storage and computational devices. At charged domain walls, the conductance may be altered due to accumulation or depletion of mobile charge carriers. By applying electrical fields, it is possible to controllably move the domain walls, making them attractive for novel electronic devices. Improper ferroelectrics, such as hexagonal manganites (h-$RMnO_3$, R = Er, Sc, Y, In, Dy), are especially interesting in this regard because they allow the formation of charged head-to-head and tail-to-tail domain walls. While single crystals of the hexagonal manganite $ErMnO_3$ are well-studied, polycrystalline $ErMnO_3$ has recently entered the spotlight because the combination of domain walls and grain boundaries increase the degrees of freedom in tailoring material properties for specific applications.

In this thesis, transmission electron microscopy (TEM) has been used to investigate the grains and ferroelectric domains in a fine-grained, electron transparent, polycrystalline $ErMnO_3$ lamella with a mean grain size of approximately 1 µm. The crystallographic orientation of grains in the lamella has been mapped out using open-source Python-based template matching applied on scanning precession electron diffraction (SPED) data. No preferred crystallographic orientation was found from the limited number of grains (26) in the lamella. The quantification of orientations enabled mapping out the angle between polar *c*-axes across grain boundaries, the in-plane component of the *c*-axes and misorientation relationships. The orientation maps were used to develop a semi-automatic method for orienting the specimen to desired zone axes. The angular accuracy of template matching was determined to be less than 1° for most crystallographic orientations, but higher for some orientations due to misindexations. Methods for avoiding misindexations have also been developed and discussed.

In-grain ferroelectric domains have been visualized using virtual dark-field (VDF) imaging from SPED data, where ferroelectric domain contrast has been observed for the majority of the investigated grains. Through a tilt series, it was found that domain contrast decreases as the angle between the crystallographic *c*-axis and the imaging plane increases. No ferroelectric domain contrast was observed for angles above approximately 72°. The results of this analysis indicated that some smaller grains are single domain. Dynamical multislice simulations of convergent beam electron diffraction and precession electron diffraction of $ErMnO_3$ in the $[2\bar{1}\bar{1}0]$ zone axis were compared to S(P)ED data to determine the ferroelectric polarization directions and specimen thickness. These simulation results were verified with experimental atomic resolution high-angle annular dark-field scanning TEM imaging and the thickness was estimated with electron energy loss spectroscopy. This work demonstrates that SPED combined with open-source template matching and dynamical simulations can give quantitative crystallographic orientation information over large areas, as well as domain structure and polarization directions.

## Sammendrag

Ferroelektriske domenevegger har nylig fått mye oppmerksomhet for deres potensiale innenfor nye 2D funksjonelle datalagrings og beregningssystemer. Den elektriske ledningsevnen ved ladde domenevegger kan endre seg på grunn av akkumulasjon eller mangel på mobile ladningsbærere. Ved å påtrykke elektriske felt kan man flytte domeneveggene på en kontrollert måte, hvilket gjør dem innbydende for nye elektroniske systemer. I denne sammenhengen er uekte ferroelektriske materialer, som for eksempel heksagonale manganitter (h-$RMnO_3$, R = Er, Sc, Y, In, Dy), spesielt interessante fordi elektrisk ladde hode-mot-hode og hale-mot-hale domenevegger kan oppstå. Mens enkrystaller av den heksagonale manganitten $ErMnO_3$ har blitt grundig undersøkt, har polykrystallinsk $ErMnO_3$ nylig havnet i søkelyset fordi kombinasjonen av domenevegger og krystallgrenseflater øker mulighetsrommet for å skreddersy materialer for spesifikke applikasjoner.

I denne masteroppgaven ble transmisjonselektronmikroskopi (TEM) brukt til å undersøke korn og ferroelektriske domener i en finkornet, elektrontransparent, polykrystallinsk $ErMnO_3$ lamell med gjennomsnittlig kornstørrelse på ca. 1 µm. Den krystallografiske orienteringen til korn i lamellen ble kartlagt med en åpen kildekode Python-basert mønstersammenlikning brukt på sveipepresesjonselektrondiffraksjon (SPED) data. Basert på det begrensede antallet korn i prøven (26), ble det ikke funnet noen foretrukket krystallografisk orientering. Kvantifisering av krystallografisk orientering muliggjorde kartlegging av vinkelen mellom polare $c$-akser på tvers as korngrenser, komponenten av $c$-aksen i planet, og misorienteringsforhold. Orienteringskartene ble også brukt til å utvikle en halvautomatisk metode for å orientere prøven til ønskede soneakser. Vinkelpresisjonen til mønstersammenlikningen ble bestemt til å være mindre enn 1° for de fleste krystallografiske orienteringer, men høyere for noen orienteringer på grunn av misindekseringer. Metoder for å unngå misindekseringer ble også utviklet og diskutert.

Ferroelektriske domener innad i korn ble avbildet ved bruk av virtuell mørkefeltsavbildning basert på SPED data, hvor ferroelektrisk domenekontrast ble observert for de fleste av de undersøkte kornene. Ved å systematisk endre prøvehelning ble det funnet at domenekontrast avtar når vinkelen mellom den krystallografiske $c$-aksen og bildeplanet øker. Det ble ikke observert noen ferroelektrisk domenekontrast for vinkler over omlag 72°. Resultatene av denne analysen indikerte at noen av de mindre kornene kun har ett domene. Dynamiske flersnittssimuleringer av konvergent elektronstråle diffraksjon og presesjonselektrondiffraksjon av $ErMnO_3$ ved $[2\bar{1}\bar{1}0]$ soneaksen ble sammenliknet med S(P)ED data for å bestemme ferroelektriske polariseringsretninger og prøvetykkelse. Simuleringsresultatene ble verifisert med eksperimentell atomisk oppløst høyvinkel-annulær-mørkefelts sveipe TEM avbildning og tykkelsen ble målt med elektronenergitapspektroskopi. Dette arbeidet at viser at SPED kombinert med åpen kildekode mønstersammenlikning og dynamiske simuleringer kan gi kvantitativ krystallografisk orienterings informasjon over store områder, samt domenestrukturer og polariseringsretninger.

# Preface

This thesis is the conclusion to my 5-year Master of Science degree in Nanotechnology with specialization within nanoelectronics in the spring of 2023. The work presented here has been carried out at the TEM Group in the Department of Physics at the Norwegian University of Science and Technology (NTNU). This thesis is a continuation of my specialization project for "TFY4520 Nanoteknologi Fordypningsprosjekt", both of which were supervised by Professor Antonius (Ton) T.J. van Helvoort.

Although the work presented in this thesis is my own, independent work, it would not have been possible without the help of others, whom I would like to thank. Most importantly, I would like to thank Ton for the excellent and valuable feedback and guidance throughout this semester and the previous. Our weekly meetings and your genuine interest in my work have been truly rewarding and pushed me to go further. I would also like to thank Dr. Jan Schultheiß and PhD. candidate Kasper Aas Hunnestad for doing the sample synthesis and FIB specimen preparation. Thank you, Dr. Emil Frang Christiansen for teaching me to operate the TEM, and helping me acquire data on the ARM TEM microscope. Thank you, Håkon Wiik Ånes for the excellent discussions about crystallographic orientations and rotations. A very special thanks goes to my dear Ida. Thank you, Ida, for taking interest in my project, for our fruitful discussions and your valuable feedback.

Anders Christian Mathisen
June 15, 2023

## List of Abbreviations

**ADF** Annular dark-field

**BF** Bright-field

**c-AFM** Conductive atomic force microscopy

**CBED** Convergent beam electron diffraction

**CDW** Charged domain wall

**DF** Dark-field

**EBSD** Electron backscatter diffraction

**EELS** Electron energy loss spectroscopy

**FCC** Face centered cubic

**FIB** Focused ion beam

**HAADF** High angle annular dark-field

**HRTEM** High resolution transmission electron microscopy

**IPF** Inverse pole figure

**NCC** Normalized cross-correlation

**PED** Precession electron diffraction

**PFM** Piezoresponse force microscopy

**SAD** Selected area diffraction

**SED** Scanning electron diffraction

**SEM** Scanning electron microscopy

**SPED** Scanning precession electron diffraction

**STEM** Scanning transmission electron microscopy

**TEM** Transmission electron microscopy

**VBF** Virtual bright-field

**VDF** Virtual dark-field

**VSA** Virtual selected area

**VSAD** Virtual selected area diffraction

**ZLP** Zero loss peak

**X-PEEM** X-ray photoemission electron microscopy

# Contents


**1 Introduction** **1**
- 1.1 Motivation and Background . . . 1
- 1.2 Problem Statement and Aim of Study . . . 2
- 1.3 Outline . . . 3

**2 Theory** **5**
- 2.1 Crystalline Materials . . . 5
- 2.2 Diffraction . . . 8
- 2.3 Descriptions of Crystal Orientations . . . 11
- 2.4 Transmission Electron Microscopy . . . 14
- 2.5 TEM Micrograph and Electron Diffraction Simulations . . . 23
- 2.6 Data Processing . . . 26
- 2.7 $ErMnO_3$ . . . 29

**3 Methods** **33**
- 3.1 Sample Synthesis and Specimen Preparation . . . 33
- 3.2 The Transmission Electron Microscopes . . . 34
- 3.3 S(P)ED Data Collection and Processing . . . 35
- 3.4 PED Multislice Simulations . . . 37
- 3.5 Code . . . 40

**4 Results** **41**
- 4.1 Sample Overview . . . 41
- 4.2 Crystal Orientations . . . 43
- 4.3 Visualization of Ferroelectric Domains . . . 51
- 4.4 CBED and PED Simulations . . . 56
- 4.5 Verification of Simulation Results . . . 64

**5 Discussion** **67**
- 5.1 The Specimen . . . 67
- 5.2 Orientation Mapping . . . 67
- 5.3 Orienting to a Zone Axes . . . 74
- 5.4 Visualizing Ferroelectric Domains . . . 75
- 5.5 Simulations . . . 79
- 5.6 Sample and Material Specific Results . . . 84

**6 Conclusion** **85**

**7 Further Work** **87**
7.1 Material . . . . . 87
7.2 Methods . . . . . 88

**A Complementary Results** **97**
A.1 Descan Off SPED . . . . . 97
A.2 Verification of Predicted Gonio Tilts For Target Zone Axes . . . . . 98
A.3 Conventional DF-TEM Domain Contrast . . . . . 98
A.4 Contrast Inversion in VDF Images From Friedel Pairs . . . . . 101
A.5 VDF Image Contrast With Increasing Out-of-Plane $c$-axis . . . . . 102
A.6 PED $\phi = 1^\circ$ Simulation . . . . . 107

**B Finding The Tilt Axes of a TEM** **109**

**C Presentations of the Work** **113**

# Chapter 1

# Introduction

## 1.1 Motivation and Background

While the improvements in conventional semiconductor technologies have started reaching both practical and fundamental limits, the demand for efficient low-power data-storage and computational devices is ever-increasing [1]. This has lead to a widespread search for alternative ways to continue the unprecedented technological progress lead by the transistor in the last seven decades. The field of functional oxide materials has in this regard become a very active research field, where interfaces, such as oxide heterostructures, exhibiting emergent phenomena are studied and utilized to control electronic transport [2]. In the past decade, other interfaces in **homogeneous** functional oxides, such as ferroelectric domain walls, have attracted a lot of attention [3, 4]. In contrast to heterostructures, the ferroelectric domain wall separates areas that are chemically identical, only differing in their electric polarization. Ferroelectric domain walls can, unlike heterostructure interfaces, be created, deleted and moved inside the bulk by external influences, such as electric fields [5] or strain [6]. The domain wall generally carries a bound charge due to the change in polarization at the interface [4]. In most ferroelectrics, this bound charge is screened by free charge carriers, altering the conductivity at the wall substantially compared to the bulk. Charged domain walls can be viewed as ultrathin, movable, highly conductive quasi two-dimensional sheets embedded in the bulk, which can guide an electric current. This feature is highly attractive for applications in nanoelectronic devices [4].

Differences in the electrical conductivity at charged domain walls (CDW) has been observed for a wide range of materials. In the 1970s, CDW were occasionally studied [7], but the real interest in the field started with a study in 2009, which currently has well over 1000 citations, of $BiFeO_3$, where a significant (five to six orders of magnitude) increase in conductivity at domain walls was observed [8]. This lead to observations of conducting domain walls in many other materials ($BaTiO_3$, $LiNbO_3$, $PbZr_{1-x}Ti_xO_3$) including, especially important for this thesis, $ErMnO_3$ [3].

$ErMnO_3$ belongs to a class of materials known as hexagonal manganites, with the general formula h-$RMnO_3$ (R = Sc, Y, In, Dy, Er). Unlike proper ferroelectrics, where electric ordering is the primary driving force for polarization, the ferroelectricity in $ErMnO_3$ arises as a by-product of a structurally driven phase transition [3]. Consequently, charged domain walls, where the polarizations meet head-to-head or tail-to-tail are formed spontaneously in the as-grown state, which does not occur in proper ferroelectrics [3, 4].

Single crystals of $ErMnO_3$ have been studied extensively using a range of different techniques including transmission electron microscopy (TEM) [5], scanning probe microscopy techniques like piezoresponse force microscopy (PFM) and conductive atomic force mi-

croscopy (c-AFM) [9], scanning electron microscopy (SEM) [10], focused ion beam (FIB) [11], and X-ray photoemission electron microscopy (X-PEEM) [12]. However, only a few studies have explored the additional domain engineering possibilities in polycrystals [6, 13]. In polycrystals, size confinement and strain from grain boundaries provide additional degrees of freedom in tailoring the domain wall properties. An inverse relationship between the size of domains and grains in polycrystalline $ErMnO_3$ has been reported [13], which is fundamentally different from domain scaling laws in proper ferroelectrics. The limited studies on polycrystalline $ErMnO_3$ have used PFM and c-AFM correlated with electron back scattered diffraction in SEM, where the spatial resolution limited to a few nm [13]. To study the atomically sharp domain walls in $ErMnO_3$, a better spatial resolution is required, which is why this work aims to use TEM to study polycrystalline $ErMnO_3$. Compared to a well-oriented single crystal, the interesting aspects here lie in how the spatial orientation and morphology of grains affects domain shape and sizes.

Polycrystals of $ErMnO_3$ do not only have ferroelectric domain walls which show potential in novel electronic devices, but also grain boundaries. Although the grain boundaries in $ErMnO_3$ remain mostly unexplored [13], they can, in the same way as domain walls, carry a bound charge which may change the electronic properties at the interface. In contrast to domain walls, the polarization at grain boundaries can meet at arbitrary angles. In combination with a possibly altered chemical environment at the boundaries [14], the potential for exciting new properties deserves exploration. While in-grain domain wall interfaces are mobile and can be created and removed on demand, the grain boundaries are stable and stationary (at room temperature). In proper ferroelectrics, ferroelectric domains tend to move across grains, meaning that a domain wall in one grain will continue into neighboring grains. A fundamentally different structure is reported for polycrystalline $ErMnO_3$, where domain walls appear to terminate at the grain boundaries [13].

An initial TEM study of polycrystalline $ErMnO_3$ for the project report preceding this thesis [15] gave qualitative impressions about the material. Grain boundaries were examined and determined to be crystalline with no intergranular phases. Scanning precession electron diffraction showed especially promising results and could be used to map crystal orientations and qualitatively visualize ferroelectric domains in grains. These promising initial results have made scanning precession electron diffraction a large focus of this thesis for the further studies of polycrystalline $ErMnO_3$.

## 1.2 Problem Statement and Aim of Study

The aim of this work is to investigate polycrystalline $ErMnO_3$ using TEM with improved spatial resolution compared to previous SPM and SEM studies. In this thesis, multiple TEM techniques will be used with a focus on finding crystallographic orientation, orientation relationships, and polarization directions within grains. This will be done using experimental scanning (precession) electron diffraction in TEM, as this technique efficiently gathers large amounts of information about the imaged specimen. To extract, understand and quantify the information contained in the data, a refined analysis compared to the methods presented in the project report preceding this thesis [15] needs to be developed. In particular, to determine the polarization direction of domains, the observed domain contrast needs to be analyzed using complementary simulations. Applying the refined analysis of scanning (precession) electron diffraction data is an important step towards understanding how the potential new properties of grain boundaries and grain size confinement in polycrystalline $ErMnO_3$ can be used in novel electronic devices.

## 1.3 Outline

This thesis is divided into seven chapters. In chapter 2, theory relevant for this work is introduced, starting with basic crystallography and moving on to some general aspects of diffraction and how to describe crystal orientations. The theory chapter further gives a brief introduction to transmission electron microscopy with emphasis on the techniques used, and some theory on simulations of TEM micrographs and diffraction patterns, and data processing. Finally, the material investigated throughout this thesis, $ErMnO_3$, is presented.

In chapter 3, experimental details on data acquisition and processing are presented, followed by chapter 4 and chapter 5 where results are presented and discussed. Conclusions from this study are presented in chapter 6. Finally, suggestions for further studies based on this work are presented in chapter 7.

Appendix A includes additional relevant results which complement and extend the findings in the main text, and Appendix B presents a procedure for determining the position of the gonio tilt axes in the TEM. The work presented in this thesis has contributed to one submitted manuscript (which I have co-authored) and two talks; *Quantitative mapping of chemical defects at charged grain boundaries in a ferroelectric oxide* [14] submitted to *Advanced Materials*, *4DSTEM for a more complete characterization of ferroelectrics* given by Antonius van Helvoort at the Ferroelectrics Domains and Domain Walls Workshop organized by the Department of Physics and the Department of Materials Science and Engineering (NTNU) in April 2023, and *Scanning precession electron diffraction for structural analysis of polycrystalline ferroelectrics* to be given by Antonius van Helvoort at the IoP-EMAG 2023 conference (Institute of Physics's Electron Microscopy and Analysis Group, given in conjunction with mmc series from the Royal Microscopical Society) in July 2023. The abstracts of the manuscript and both talks are included in Appendix C.

# Chapter 2

# Theory

In this chapter, relevant background theory for this study is presented. The two first sections introduce some basic crystallography and a commonly used method for studying crystals, namely diffraction. These two sections are mainly based on *Introduction to Solid State Physics* by Charles Kittel [16]. In the third section, common ways to describe and visualize the orientation of crystals are introduced. The fourth section gives a brief introduction to transmission electron microscopy with emphasis on the techniques used in this thesis. The fifth section presents the multislice solution for simulating TEM results. The sixth section gives a brief overview of the data processing and how to get an orientation map from a 4D SPED data stack by template matching. In the final section, the material $ErMnO_3$ is introduced along with a brief overview of ferroelectricity and ferroelectric domain walls. Much of the theory presented in this chapter is reused from my project report for TFY4520 preceding this thesis [15].

## 2.1 Crystalline Materials

Crystals are periodic materials consisting of atoms or groups of atoms arranged in a repetitive and organized manner. The force that holds the atoms in the crystal together can largely be categorized into four different categories: Van der Waals, ionic, metallic and covalent bonds. In this work, the ionic bonds, where the crystal consists of positively charged cations and negatively charged anions, are of particular interest.

The crystal is mathematically defined as an atom or a group of atoms, known as a basis, repeated on an infinite lattice in all three dimensions. The lattice is defined by three translation vectors $\mathbf{a}_1$, $\mathbf{a}_2$ and $\mathbf{a}_3$, corresponding to the three directions the basis is repeated. This means that any point $\mathbf{R}$ is equivalent to $\mathbf{R}'$ when the two are related through the equation

$$\mathbf{R}' = \mathbf{R} + u_1\mathbf{a}_1 + u_2\mathbf{a}_2 + u_3\mathbf{a}_3 \tag{2.1}$$

where $u_i$ are integers.

The unit cell spanned by the three translation vectors is usually the smallest building block of the crystal and has a volume of $|\mathbf{a}_1 \cdot \mathbf{a}_2 \times \mathbf{a}_3|$. For some crystals a larger unit cell can be chosen to make crystal symmetries more apparent. Conventionally, the unit cell is chosen so that the lattice points are placed in the corner of the cell. There are other possibilities such as the Wigner-Seitz primitive unit cell where the lattice points are placed in the center. In addition to the length of the three translational vectors, unit cells are often described by

the angles between them,

$$\mathbf{a}_1 \angle \mathbf{a}_2 = \gamma \qquad \mathbf{a}_1 \angle \mathbf{a}_3 = \beta \qquad \mathbf{a}_2 \angle \mathbf{a}_3 = \alpha. \tag{2.2}$$

The basis is typically defined by placing a single atom on a lattice point, and describing any other atoms in the basis by a translation,

$$\mathbf{r}_j = x_j \mathbf{a}_1 + y_j \mathbf{a}_2 + z_j \mathbf{a}_3 \tag{2.3}$$

from the first atom, where $0 \leq x_j, y_j, z_j \leq 1$. The entire crystal is described by the convolution of the lattice with the basis.

An important characteristic property of crystals for x-ray scattering is the electron density, $n(\mathbf{r})$. The electron density is a periodic function describing the number density of electrons in the crystal. It is conveniently described by a Fourier series. In general terms, the electron density in three dimensions is described as

$$n(\mathbf{r}) = \sum_{\mathbf{G}} n_{\mathbf{G}} e^{i\mathbf{G}\cdot\mathbf{r}} \tag{2.4}$$

with the Fourier coefficients

$$n_{\mathbf{G}} = \frac{1}{V_c} \int_{\text{cell}} \mathrm{d}V \, n(\mathbf{r}) e^{-i\mathbf{G}\cdot\mathbf{r}}, \tag{2.5}$$

where $V_c$ is the volume of the unit cell. The set of reciprocal lattice vectors $\mathbf{G}$ define a reciprocal lattice related to the real lattice. The vectors in $\mathbf{G}$ are defined as

$$\mathbf{G}_{hkl} = h\mathbf{b}_1 + k\mathbf{b}_2 + l\mathbf{b}_3, \qquad \mathbf{b}_i = \epsilon_{ijk} \frac{2\pi}{V_c} \mathbf{a}_j \times \mathbf{a}_k, \qquad \epsilon_{123} = 1, \tag{2.6}$$

where $h$, $k$ and $l$ are integers and $\mathbf{b}_i$ are the reciprocal lattice vectors. Equation 2.4 only sums over the vectors in $\mathbf{G}$ because they are the only vectors with the same periodicity as the crystal, and the Fourier coefficients of any other vector would be zero. Using the description of $\mathbf{G}$ in Equation 2.6, it can be shown that $n(\mathbf{r})$ is a real function, and that it obeys translational invariance under a translational vector $\mathbf{T} = u_1\mathbf{a}_1 + u_2\mathbf{a}_2 + u_3\mathbf{a}_3$, as required.

### 2.1.1 Crystal Directions and Planes

Miller indices are used to describe crystal directions and planes. For a given plane, the Miller indices are found by finding the intercept of the plane with the crystal axes in terms of the translation vectors. The Miller indices are the reciprocals of the three intercepts, multiplied by the smallest common denominator. The resulting three integers, $h$, $k$ and $l$, describe a unique crystal plane which Miller index is given by $(hkl)$. As an example, the plane in Figure 2.1(a) intersects the $\mathbf{a}_1$ (x)-axis at -2, the $\mathbf{a}_2$ (y)-axis at 2/3, and is parallel to the $\mathbf{a}_3$ (z)-axis and is thus described by the Miller index $(\bar{1}30)$.

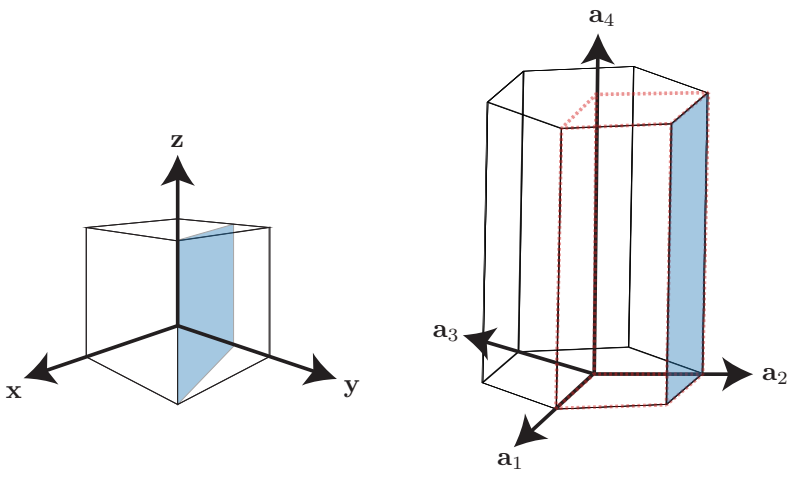


(a) (b)

Figure 2.1: (a) A cubic unit cell with a $(\bar{1}30)$ plane in blue. (b) A hexagonal unit cell marked with the red dashed line with a $(01\bar{1}0)$ plane in blue. For illustrative purposes, the unit cell vectors have been extended, instead of that they terminate at the surface of the unit cell.

Crystal directions are indexed so that the vector $[uvw]$ describe the vector $\mathbf{v} = u\mathbf{a}_1 + v\mathbf{a}_2 + w\mathbf{a}_3$. For cubic systems, the normal vector to the plane $(hkl)$ is conveniently described by $[hkl]$.

For the hexagonal system, it can be convenient to introduce a redundant axis and use 4 instead of 3 indices. This Miller-Bravais notation is shown in Figure 2.1(b). Three axes are placed in the basal plane with 120° between them, and the fourth is placed normal to the basal plane. Plane indices are found as before, and are given by $(hkil)$, where $h + k = -i$ to ensure uniqueness. A vector is indexed as $[UVTW]$, with $U + V = -T$. Without this rule, [2000], [3110] and $[4\bar{2}\bar{2}0]$ would all describe the same vector, which can cause confusion. In Figure 2.1(b), the blue plane is parallel to $\mathbf{a}_1$ and $\mathbf{a}_4$, and intersects $\mathbf{a}_2$ at 1, and $\mathbf{a}_3$ at -1, so that the index for this plane is $(01\bar{1}0)$.

The main reason Miller-Bravais is used for hexagonal systems is that families of planes appear more similar in their notation. Families of planes are described similar to crystal planes but placed in curly brackets and describe several crystal planes which are similar due to crystal symmetry. In the three axis Miller index for a hexagonal system, the {100} family of planes includes (100), (010), $(\bar{1}00)$, $(0\bar{1}0)$, $(\bar{1}10)$ and $(1\bar{1}0)$. It is not immediately obvious that all these are in the same family, while in the Miller-Bravais system, the equivalent family of planes $\{10\bar{1}0\}$ includes $(10\bar{1}0)$, $(01\bar{1}0)$, $(\bar{1}010)$, $(0\bar{1}10)$, $(\bar{1}100)$ and $(1\bar{1}00)$.

Both the Miller-Bravais and the Miller indexing systems are valid descriptions of lattice planes and crystal vectors in the hexagonal unit cell, and both will be used in this thesis. For lattice planes, $(hkil)$ can easily be converted to $(hkl)$ by removing $i$. For vectors, $[UVTW]$ and $[uvw]$ are related through

$$u = U - T \qquad v = V - T \qquad w = W. \tag{2.7}$$

A normal vector, $\mathbf{n}$, to a plane $(hkil)$ is found by

$$\mathbf{n} = h\mathbf{a}_1 + k\mathbf{a}_2 - (h + k)\mathbf{a}_3 + \frac{3|\mathbf{a}_1|^2}{2|\mathbf{a}_4|^2} l\mathbf{a}_4. \tag{2.8}$$

In many cases, such as for calculating angles between crystal directions, it is useful to express crystal vectors in a Cartesian coordinate system. Here, the convention used by Rowenhorst *et al.* [17],

$$\mathbf{e}_1 \| \frac{\mathbf{a}_1}{|\mathbf{a}_1|} \qquad \mathbf{e}_2 \| \mathbf{e}_3 \times \mathbf{e}_1 \qquad \mathbf{e}_3 \| \frac{\mathbf{a}_4^*}{|\mathbf{a}_4^*|}, \tag{2.9}$$

will be used. For the hexagonal unit cell of $ErMnO_3$, this gives the following equation for converting a crystal direction $[uvw]$ to a Cartesian vector $(x, y, z)$.

$$(x, y, z) = [uvw] \cdot \begin{bmatrix} 6.115 & 0 & 0 \\ -3.0575 & 5.2957 & 0 \\ 0 & 0 & 11.41 \end{bmatrix} \tag{2.10}$$

The interplanar spacing, $d_{hkl}$, for a plane $(hkl)$ in a hexagonal unit cell can be calculated from the equation,

$$\frac{1}{d_{hkl}^2} = \frac{4}{3}\left(\frac{h^2 + hk + k^2}{|\mathbf{a}_1|^2}\right) + \frac{l^2}{|\mathbf{a}_4|^2}. \tag{2.11}$$

This formula shows that higher values of $h$, $k$ and $l$ generally describe closer spaced crystallographic planes.

### 2.1.2 Crystal Symmetries

Crystalline materials may also be described by their symmetries. A point group is a set of symmetry operations such as reflections, inversions or rotations, which can be performed on a crystal and leaves it in the original configuration. In total, there are 32 point groups in three dimensions. $ErMnO_3$ has the point group 6mm, which means that it has a six-fold rotation symmetry, along the $\mathbf{a}_4$ axis, and two mirror planes with normal perpendicular to the six-fold rotation axis. In three dimensions, the 32 point groups may be combined with the 14 different Bravais lattices to form a total of 230 space groups. The space groups combine the point group symmetries with the symmetries of the Bravais lattices which introduces additional symmetries like screw axes and glide planes. These are combinations of rotations and translations, and combinations of mirror planes and translations, respectively. The International Union of Crystallography has standardized the notation for point groups and space groups [18]. In this report, the Hermann-Mauguin (international) notation will be used for point and space groups.

Crystal symmetries are important for physical properties. For instance, the point group 6/mmm, which is similar to 6mm, but also has a mirror plane with normal parallel to the six-fold rotation axis, describes a centrosymmetric crystal structure. This means that there is an inversion center in the crystal, and properties described by a vector, such as ferroelectricity, can not occur. Crystals with the 6mm point group are non-centrosymmetric, and so they can exhibit ferroelectricity.

The point group 6/mmm is the Laue group of 6mm. The Laue group of a point group is the result of adding an inversion center, and is the observed symmetry in kinematic diffraction patterns. While there are 32 point groups, there are only 11 Laue groups.

## 2.2 Diffraction

Lattice spacings, elements, symmetries and deviations from the ideal structure in crystalline materials are widely studied using diffraction. Diffraction based techniques broadly involve sending a coherent wave, usually in the form of x-rays, electrons or neutrons, towards the specimen and observing the resulting diffraction pattern. Diffractograms and diffraction

patterns include information on the specimen such as orientation, lattice parameters and crystal structure. To understand how this information is encoded in the diffraction pattern, one needs to have a good understanding of how the diffraction pattern is formed. As this project involves TEM, the focus here will be on 2D electron diffraction patterns, although first the general aspects of diffraction are introduced.

### 2.2.1 Braggs Law

A simple model of diffraction focuses on the path difference of electrons reflecting of different lattice planes. The coherent electron beam hits a set of planes separated by a distance $d_{hkl}$ at an angle $\theta$ and is reflected by the same angle $\theta$. The additional distance which the wave scattering of the second plane travels is given by $2d_{hkl}\sin\theta$. For the two reflected waves to have constructive interference, this additional path distance must be equal to an integer number of wavelengths. This equality is known as Braggs Law,

$$2d_{hkl}\sin\theta = n\lambda, \tag{2.12}$$

and implies that closer spaced crystal planes will reflect the beam to a larger angle.

### 2.2.2 Laue Equations

Braggs law is a simple, and somewhat inaccurate model of diffraction. The coherent wave is not generally reflecting off planes as assumed in the derivation of Braggs law, but rather scattering or diffracting of them. Braggs law also completely fails to explain how the intensities of the diffraction peaks might vary, or how a multi-atom basis will affect the resulting diffraction pattern. Another description of diffraction is needed.

The phase difference between waves scattered at two points separated by $\mathbf{r}$ is $(\mathbf{k}-\mathbf{k}')\cdot\mathbf{r}$, where $\mathbf{k}$ and $\mathbf{k}'$ are the wave vectors of the incoming and scattered waves, respectively. It is assumed that the amplitude of the scattered wave is proportional to a scattering density, $\rho(\mathbf{r})$, so that the total amplitude of the scattered wave, $F$, in the direction of $\mathbf{k}'$ is given by,

$$F = \int \mathrm{d}V\, \rho(\mathbf{r}) e^{i(\mathbf{k}-\mathbf{k}')\cdot\mathbf{r}} \tag{2.13}$$

In x-ray diffraction, the scattering density is the electron density. By inserting Equation 2.4 into Equation 2.13 we get

$$F = \sum_{\mathbf{G}} \int \mathrm{d}V\, n_{\mathbf{G}} e^{i(\mathbf{G}-\mathbf{Q})\cdot\mathbf{r}}. \tag{2.14}$$

In this equation $\mathbf{Q}$ is the scattering wave, and it is defined as $\mathbf{k}'-\mathbf{k}$. When integrating over the entire crystal, the phase term $\exp\{i(\mathbf{k}-\mathbf{k}')\cdot\mathbf{r}\}$ will in general average out to zero and thus no give no diffraction intensity. The exception to this occurs when the scattering wave is equal to the reciprocal lattice vector $\mathbf{G}$ (Equation 2.6). The Laue equations are derived from this diffraction condition by taking the inner product with $\mathbf{a}_1$, $\mathbf{a}_2$ and $\mathbf{a}_3$ on both sides of the equation.

$$\mathbf{a}_1\cdot\mathbf{Q} = 2\pi h \qquad \mathbf{a}_2\cdot\mathbf{Q} = 2\pi k \qquad \mathbf{a}_2\cdot\mathbf{Q} = 2\pi l \tag{2.15}$$

The intensity, $I(\mathbf{k})$, of the diffraction pattern is proportional to the absolute square of the scattering amplitude, consequently the diffraction pattern is centrosymmetric (Laue group symmetry), even for non-centrosymmetric crystals, under kinematic conditions.

The Ewald sphere construction shown in Figure 2.2 is a useful geometric interpretation of the diffraction conditions. Because $|\mathbf{k}'| = |\mathbf{k}|$ under kinematic conditions, the set of all possible $\mathbf{k}'$s forms a sphere in reciprocal space. This sphere is the Ewald sphere. By letting $\mathbf{k}'$ and $\mathbf{k}$ have the same origin so that $\mathbf{k}$ terminates in the origin of reciprocal space, the diffraction condition is met when a reciprocal lattice point intersects with the Ewald sphere. Electrons in a TEM have very short wavelength which means that the Ewald sphere has a large radius compared to the repetition distances in reciprocal space. Furthermore, because the sample is thin, the "points", or relrods, in reciprocal space are extended in the direction of the beam. This means that many relrods meet the diffraction criteria, and diffraction patterns in TEM have many reflections.

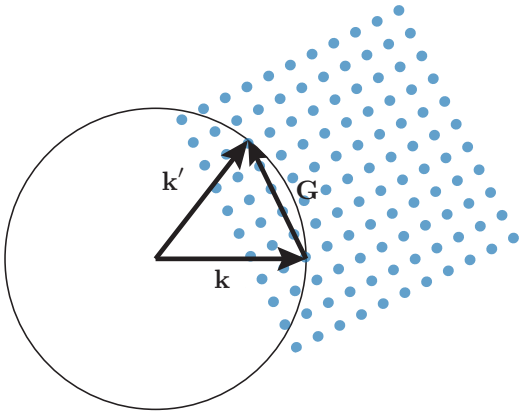


Figure 2.2: The Ewald sphere construction in 2D. Where the blue reciprocal lattice points intersect the sphere formed by $\mathbf{k}$ and $\mathbf{k}'$, the diffraction condition is fulfilled. The Ewald sphere here is, for illustrative purposes, drawn with a smaller radius than it would have in TEM. This schematic is inspired by Figure 8 in chapter 2 of Kittel [16].

### 2.2.3 Structure Factor and Atomic Form Factor

When the diffraction condition, $\mathbf{Q} = \mathbf{G}$, is met, Equation 2.14 can be simplified to $NS_{\mathbf{G}}$, where $N$ is the number of unit cells contributing to the diffraction and $S_{\mathbf{G}}$ is the structure factor defined as an integral over a single cell. Since a single cell can consist of multiple and possibly different atoms, it is useful to decompose the electron density to a sum over the $s$ atoms in the unit cell. Each atom $j$ then has a contribution to the electron density equal to $n_j(\mathbf{r} - \mathbf{r}_j)$, where $\mathbf{r}_j$ is the position of atom $j$ in the unit cell. Instead of expressing $\rho(\mathbf{r})$ in terms of the Fourier expansion of the electron density, $n(\mathbf{r}) = \sum_j n_j(\mathbf{r} - \mathbf{r}_j)$ can be used to obtain the expression for $S_{\mathbf{G}}$,

$$S_{\mathbf{G}} = \sum_j f_j e^{-i\mathbf{G}\cdot\mathbf{r}_j}, \tag{2.16}$$

where $\mathbf{r}_j$ is defined by Equation 2.3 and $f_j$ is the atomic form factor given by

$$f_j = \int \mathrm{d}V\, n_j(\mathbf{r}')e^{-i\mathbf{G}\cdot\mathbf{r}'}, \qquad \mathbf{r}' = \mathbf{r} - \mathbf{r}_j. \tag{2.17}$$

From the definition of **G** in Equation 2.6, the structure factor can be simplified to the more practical form

$$F(hkl) = \sum_j f_j \exp\{-2\pi i(hx_j + ky_j + lz_j)\}. \tag{2.18}$$

A classical application of Equation 2.18 is deriving the extinction rules for the face-centered cubic lattice, which has identical atoms at 000, $\frac{1}{2}\frac{1}{2}0$, $\frac{1}{2}0\frac{1}{2}$ and $0\frac{1}{2}\frac{1}{2}$. By insertion into Equation 2.18, the structure factor becomes $F(hkl) = f_j(1+e^{-i\pi(h+k)}+e^{-i\pi(h+l)}+e^{-i\pi(k+l)})$. From this equation, one can see that any combination of $hkl$ where the indices are not all even, or all odd will result in a structure factor of zero and thus a kinematically extinct reflection. For more complex crystals, like $ErMnO_3$, the structure factor expression not as easy to study analytically.

### 2.2.4 Dynamical Diffraction

The mathematical formalism of diffraction presented so far assumes kinematic diffraction. For certain types of diffraction, such as x-ray diffraction, this is usually a good model. However, for electron diffraction, it may break down. The key assumption in kinematic theory is that the incoming wave only participates in a single scattering event. The interaction between the electrons and the sample is so strong that this not necessarily holds true. Multiple scattering events is called dynamical diffraction and can not be described by the kinematic diffraction theory presented above.

In the case of dynamical diffraction, the sample may be modeled as a stack of thin layers where each layer acts kinematically (known as the multislice solution), or a quantum mechanical Bloch wave description may be used. Both these approaches are used for simulations of TEM micrographs and will be covered in greater detail in section 2.5.

While kinematic diffraction theory predicts a centrosymmetric diffraction pattern, even for non-centrosymmetric crystal structures, dynamical diffraction theory can more correctly predict the intensity variations in diffraction patterns, allowing non-centrosymmetric crystals to be explored.

## 2.3 Descriptions of Crystal Orientations

The process of describing the orientations of crystals need a rigorous mathematical framework, and there are several conventions and descriptions to choose from. This report will follow the conventions presented in *Introduction to Texture Analysis* by Olaf Engler and Valerie Randle [19].

To specify the orientation of crystals, two sets of orthonormal coordinate systems are used, and the orientation is defined as the transformation between them. These are the sample coordinate system, $C_s$, and the crystal coordinate system, $C_c$. The sample coordinate system is chosen in respect to (some aspect of) the bulk sample. For some types of sample, the choice of sample coordinate system is easy. An example of this is samples that have been rolled so that the rolling direction, transverse direction and the normal to the rolling plane form an orthonormal set. When investigating a lamella sample in TEM, the choice of the TEM optical axis as the $C_s$ $z$-axis is natural, but the choice of $x$ and $y$ directions are more arbitrary. In this report, the $x$ and $y$ direction of the sample coordinate system is chosen as the fast and slow scanning directions of the image forming scan, respectively.

The second coordinate system, $C_c$, is conventionally chosen in respect to the crystal symmetry. If the translational lattice vectors are orthogonal, these become a natural coordinate

system choice. In the hexagonal system this is not the case and the choice of $C_c$ usually falls on $[2\bar{1}\bar{1}0]$, $[01\bar{1}0]$, $[0001]$ with normalization as these are high symmetry directions.

As mentioned, the crystal orientation is defined as the rotation, $g$, which satisfies the following relation,

$$C_c = g \cdot C_s. \tag{2.19}$$

According to Euler's rotation theorem, any rotation of a rigid body such as $C_s$, may be described by an axis of rotation, and an angle of rotation about that axis, resulting in three degrees of freedom. Still, the orientation, $g$, is in crystallography often represented in many, often over-specified, ways. A choice of representation is a rotation matrix,

$$g = \begin{bmatrix} \cos\alpha_1 & \cos\beta_1 & \cos\gamma_1 \\ \cos\alpha_2 & \cos\beta_2 & \cos\gamma_2 \\ \cos\alpha_3 & \cos\beta_3 & \cos\gamma_3 \end{bmatrix}, \tag{2.20}$$

where $\alpha_i$, $\beta_i$ and $\gamma_i$ are the angles between the $i^{\text{th}}$ element of $C_c$ and the first, second and third element of $C_s$, respectively.

The matrix representation of $g$ can be useful for calculations, however it is an over-specified representation of $g$. For instance, any pair of two rows or columns give the third by a cross product. A different representation of $g$ is the ideal orientation in which the first and last columns of the orientation matrix are extracted and multiplied with a factor to make them whole numbers. These numbers are then written as $(hkl)[uvw]$. Because the first and last column of the orientation matrix correspond to the specimen x and y directions in the crystal coordinates, this representation highlights which planes and directions are parallel to the sample directions.

Euler angles are another common representation of orientations, which only uses three numbers. Again, there are several conventions to choose from, but the most used in crystallography is the Bunge convention [20]. The Bunge convention uses a triplet $\{\phi_1, \Phi, \phi_2\}$ where the three numbers correspond to sequential rotations, each described by the rotation matrices,

$$g_{\phi_{1,2}} = \begin{bmatrix} \cos\phi_{1,2} & \sin\phi_{1,2} & 0 \\ -\sin\phi_{1,2} & \cos\phi_{1,2} & 0 \\ 0 & 0 & 1 \end{bmatrix} \qquad g_{\Phi} = \begin{bmatrix} 1 & 0 & 0 \\ 0 & \cos\Phi & \sin\Phi \\ 0 & -\sin\Phi & \cos\Phi \end{bmatrix}, \tag{2.21}$$

with $\phi_{1,2} \in [0, 2\pi]$ and $\Phi \in [0, \pi]$, so that the orientation is given as $g = g_{\phi_2} \cdot g_{\Phi} \cdot g_{\phi_1}$. The Bunge convention is often referred to as ZXZ, because the first rotation, $g_{\phi_1}$, describes a rotation about the Z axis, the second, $g_{\Phi}$, a rotation about the X axis (in the new coordinate system after the first rotation), and the final rotation, $g_{\phi_2}$, a rotation about the Z axis, again in the new coordinate system.

While Euler angles give a somewhat intuitive representation of orientations, performing calculations such as combining rotations is not trivial in this representation. The unit quaternions have proved to be a useful representation of orientations in this regard. In this representation, the orientation $g$ is represented as a four-dimensional vector $g = q_0 + iq_1 + jq_2 + kq_3 = \cos\frac{\theta}{2} + \sin\frac{\theta}{2}(c_1 i + c_2 j + c_3 k)$. Where $[c_1,\ c_2,\ c_3]$ is the axis of rotation and $\theta$ is the angle of rotation. The quaternion representation is often used as a back-end representation in software because it is a compact notation compared to rotation matrices, its elements vary continuously as the orientation changes, and combinations of rotations may be calculated using simple quaternion algebra similar to complex numbers [17, 21].

The relationship between different crystal orientations may be described by a misorientation, describing the rotation between one orientation and another [22]. The misorientation $m_{\alpha\beta}$ between two crystal orientations, $g_\alpha$ and $g_\beta$, is defined as

$$m_{\alpha\beta} = g_\alpha^{-1} g_\beta. \tag{2.22}$$

As the misorientation is simply another rotation, it may be represented similar to the rotations presented above. The misorientation angle is defined as angle of rotation, $\theta$, about the rotation axis.

A general remark when it comes to crystal (mis)orientations is that different research groups and software packages might use different definitions. For instance, the commonly used MTEX software in Matlab uses the inverse definition of orientations compared to the definition used in this project, transforming $C_c$ to $C_s$ [23]. This can cause confusion in comparing methods and results, and is the motivation behind the work of Rowenhorst *et al.* [17].

### 2.3.1 Symmetry Reduced Orientations

One of the key defining properties about crystals are their symmetries, operations such as rotation, inversion or mirroring which leaves the crystal looking the same as before the operation was applied. The symmetries present in a crystal reduces the amount of possible orientations. For instance, if a crystal has a rotation hexad (six-fold rotational symmetry) along $\mathbf{a}_4$, then each orientation has 5 other equivalent orientations, corresponding to the operating with the hexad a number of times. These six orientations are in fact not just equivalent, but describe the exact same orientation. The difference between them only reflects our choice in unit cell, and not any physical difference in the crystal. Considering crystal symmetries is therefore essential when analyzing crystal (mis)orientations [22].

### 2.3.2 Inverse Pole Figures

The direction of any 3D vector can be described as a point on a unit sphere, and may also be projected to a 2D figure. In the stereographic projection, which is widely used in crystallography, points on the sphere are projected down to its equatorial plane by the intersection of that plane and a line between the north pole and the given point. This intersection gives the pole of that direction in the stereographic projection. This process is illustrated in Figure 2.3(a).

A common way of visualizing a crystallographic orientation is to express the three sample directions $C_s$ in terms of $C_c$ and plotting them in a stereographic projection. This is known as an inverse pole figure (IPF). The stereographic projection generally includes the full circle of the equatorial plane, however crystal symmetries will make areas in the stereographic projection equivalent. In Figure 2.3(b) the symmetry reduced area of an inverse pole figure for the 6/mmm symmetry is shown. The stereographic projection has some key advantages compared to other projections of a sphere to a plane. For instance, a circle on the sphere remains a circle in the projection, and angles between directions can directly be read of the projection.

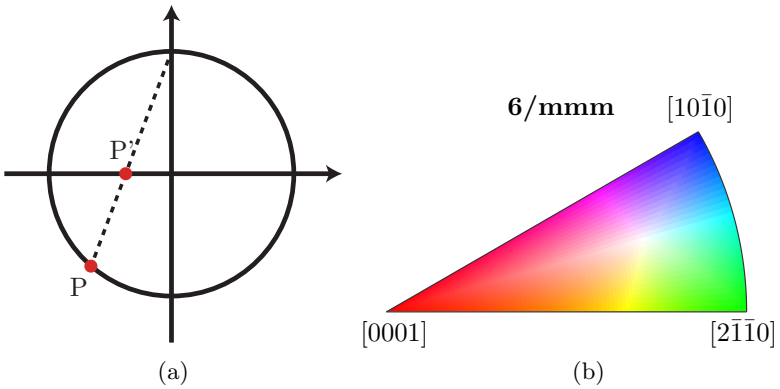


Figure 2.3: (a) A 2D visualization of the stereographic projection. The point P on the circle is projected to the point P' on the equatorial line. (b) The symmetry reduced area of the stereographic projection for the 6/mmm symmetry. For this symmetry, the full orientation sphere has 24 equivalent regions where 12 are in the northern hemisphere and 12 are in the southern. The colors describe different crystallographic directions.

## 2.4 Transmission Electron Microscopy

The transmission electron microscope (TEM) is a versatile electron microscope used to investigate small volumes. Similar to other electron microscopes, the sample is probed with an electron beam. However, in TEM the sample is so thin (<100 nm) that the electrons are transmitted though the sample and detected on the other side. This section gives a brief overview of the microscope and a few commonly used techniques. The text is based on *Transmission Electron Microscopy* by D. Williams and C. Carter [24].

The four main components of a TEM are the illumination system, objective lenses including specimen stage, and the intermediate and projector lenses. A schematic of a TEM column is shown in Figure 2.4. The electrons start their journey towards the specimen in the illumination system where electrons are accelerated from the electron gun by an electric field (∼80 kV-300 kV, this work used 200 kV). It is desired to have an electron gun with as sharp of a tip as possible because this improves resolution. The electrons pass through a set of magnetic condenser lenses, deflectors and a condenser aperture, constituting the rest of the illumination system.

Magnetic lenses have much the same effect on electrons as optical lenses have on photons, they bend electrons due to the Lorentz force and will focus parallelly incoming electrons to a disk of least confusion. This disk is the closest thing to a focal point in a magnetic lens due to low convergence angles and high aberrations, when compared to optical lenses. Through the illumination system the beam is demagnified, and the spot size, shape, brightness, shift and tilt (i.e. beam path though the column) can be controlled. Near the optical axis the magnetic lenses are less susceptible to spherical aberrations, and so the condenser aperture removes electrons far from the optical axis, reducing the size of the disk of least confusion.

In conventional TEM, where a broad static beam is illuminating the sample, it is usually desired to have the electrons travel parallel to the optical axis as this usually gives better image contrast and sharper diffraction patterns. In scanning transmission electron microscopy, which is covered in more detail in subsection 2.4.4, the electron beam is made to converge on the sample, and is scanned across the sample. It is the illumination system, along with the objective lenses which control this behavior.

The objective lenses are the strongest lenses in the TEM, controlling together with the illumination system how the electron beam hits the sample. In the back focal plane, a

diffraction plane, of the objective lenses, we find the objective aperture. This aperture can be used to exclude electrons scattered to high angles or only include certain reflections, forming the foundation for bright-field and dark-field imaging.

The sample is placed in between the objective lenses on the specimen stage / sample holder. There are several types of sample holders for different purposes. In this work, a double tilt holder was used. With this holder, the sample can be moved in all three spatial directions, as well as tilted about two perpendicular tilt axes. The space between the pole pieces of the objective lenses is small, limiting the sample orientations that can be reached by tilting. The sample holder used here could be tilted to $\pm 30^\circ$ about both tilt axes.

Below the specimen stage and the objective lenses, in an image plane of the objective lens, a selected area aperture can be inserted. Being placed in an image plane, the aperture creates a virtual aperture in the specimen plane, and can thus be used to only include electrons from a particular region of the sample. The selected area aperture is used for selected area diffraction. Due to practical limitations of how small the selected area aperture can be made, and how accurately it can be positioned, the spatial resolution of the aperture in the specimen plane is about 100 nm. Higher spatial resolution of diffraction patterns can be obtained by a scanning focused probe.

Finally, after the selected area aperture, the electrons enter the intermediate lenses, stigmators and projector lens. These lenses project either the image plane or the back focal plane down to a viewing screen. This set of lenses allow for controlling magnification in real space and diffraction patterns.

### 2.4.1 Sample Holder

The double tilt holder can move the sample in all three spatial directions, but also has two axes $T_1$ and $T_2$ about which the sample can be tilted. These two additional degrees of freedom are very useful for orientation of the sample during imaging and diffraction. A schematic of the geometry of a double tilt holder is shown in Figure 2.5.

The act of tilting the sample may be described by a rotation matrix. When the sample is tilted from $\beta_0$ to $\beta_0 + \beta$ about the $T_2$ axis ($y$-tilt), followed by a tilt from $\alpha_0$ to $\alpha_0 + \alpha$ about the $T_1$ axis ($x$-tilt), the rotation can be described by two rotation matrices

$$T_1(\alpha) = \begin{bmatrix} 1 & 0 & 0 \\ 0 & \cos\alpha & -\sin\alpha \\ 0 & \sin\alpha & \cos\alpha \end{bmatrix} \tag{2.23}$$

$$T_2(\beta;\alpha_0) = \begin{bmatrix} \cos\beta & -\sin\beta\sin\alpha_0 & \sin\beta\cos\alpha_0 \\ \sin\beta\sin\alpha_0 & \cos^2\alpha_0 + \sin^2\alpha_0\cos\beta & \sin\alpha_0\cos\alpha_0(1-\cos\beta) \\ -\sin\beta\cos\alpha_0 & \sin\alpha_0\cos\alpha_0(1-\cos\beta) & \sin^2\alpha_0 + \cos^2\alpha_0\cos\beta \end{bmatrix} \tag{2.24}$$

so that the new position of a vector, $\mathbf{v}$, is given as $\mathbf{v}' = T_1(\alpha) \cdot T_2(\beta) \cdot \mathbf{v}$ [25]. The matrix product $T_1(\alpha) \cdot T_2(\beta)$ is referred to as $T(\alpha, \beta; \alpha_0, \beta_0)$.

$T(\alpha, \beta; \alpha_0, \beta_0)$ can be used to calculate the crystallographic orientation a grain will be in for any $x$- and $y$-tilt, given that the orientation in a reference sample tilt is known. If the orientation of a grain in the reference tilt $(x_0, y_0)$ is $g_0$, then by applying the effect of $T(x - x_0, y - y_0; x_0, y_0)$ on $g_0$, the new orientation $g$ is found for the new sample tilt $(x, y)$. $T(x - x_0, y - y_0; x_0, y_0)$ can, however, not simply be multiplied with $g_0$ as the two are defined in completely different reference frames. The orientation $g$ is defined as the rotation which takes $C_s$ (defined by the directions of a SPED scan) to the crystal reference frame, $C_c$, while $T(x - x_0, y - y_0; x_0, y_0)$ is defined to operate on $C_s$ expressed in the basis of the tilt axes

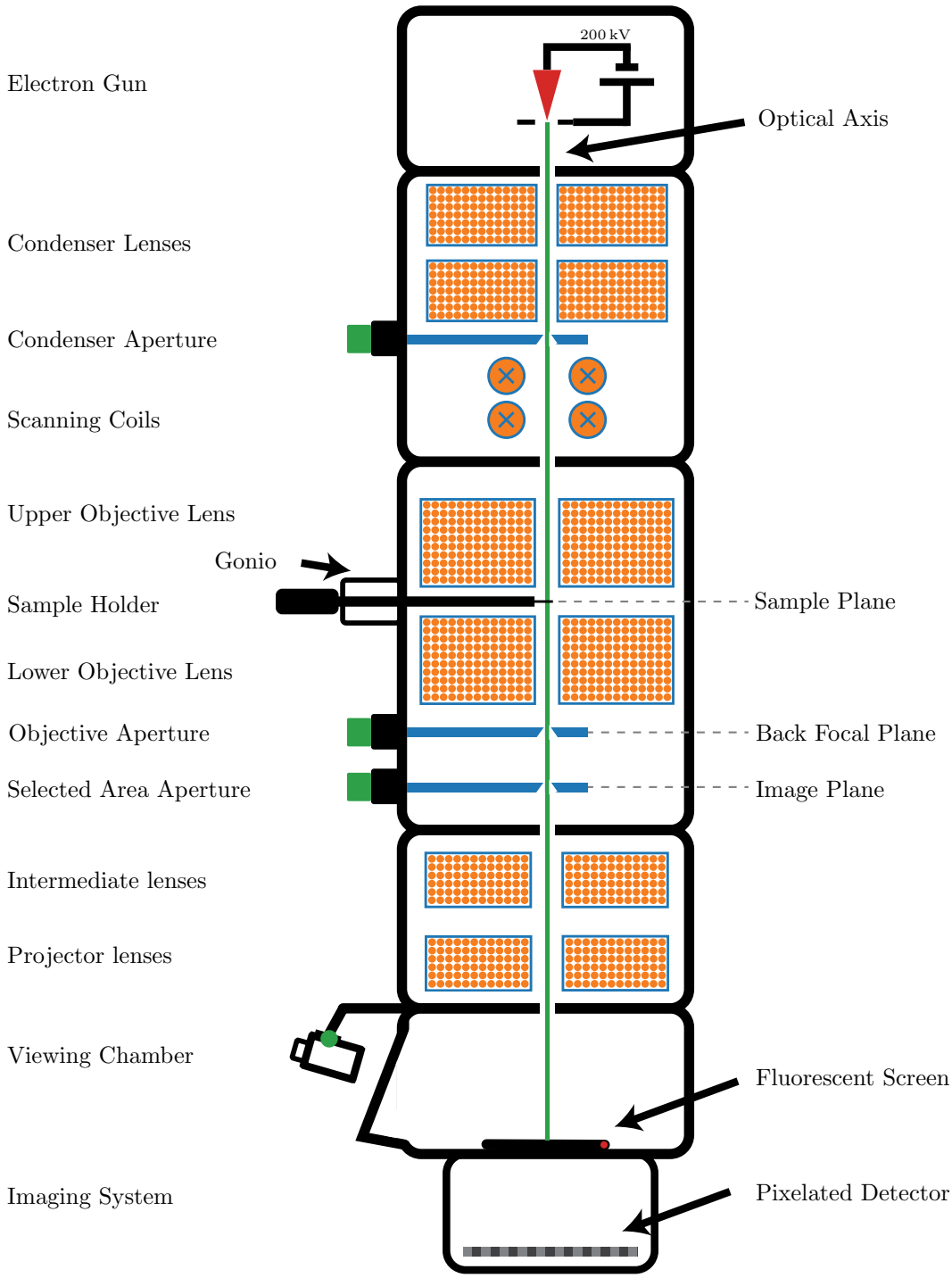


Figure 2.4: Schematic of a TEM column highlighting some of the most important parts. The layout of an actual TEM will vary from model to model. The TEM is mostly operated electronically, but the apertures, which are colored green, are operated manually by mechanical screws.

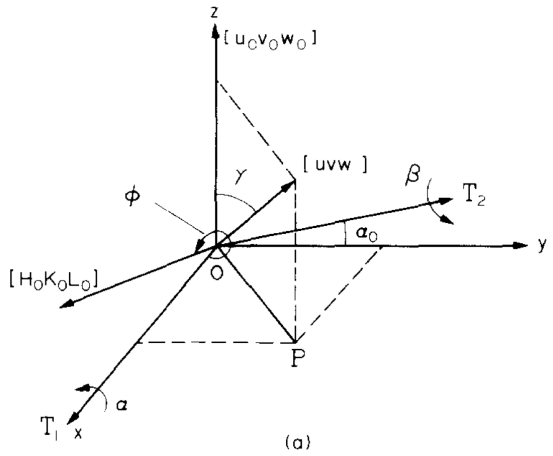


Figure 2.5: Relationship of crystal in adjustment of double tilt holder. Figure is taken from Qing *et al.* [25].

$T_1$ and $T_2$. We therefore have to express $g_0$ in the $T_1$ and $T_2$ basis in order to operate with $T(x - x_0, y - y_0; x_0, y_0)$, before converting back the transformed orientation to the definition of crystal orientations (Equation 2.19). The $C_s$ axes (direction of the scan), and the $T_1$ and $T_2$ reference frames will in general not be aligned, but do share the optical axis of the TEM as the $z$-axis. The two are therefore related by an in plane rotation $R(\theta)$ (a method for finding $\theta$ is presented in Appendix B). The new orientation $g$ after tilting to $(x, y)$ is expressed as

$$g = (R(-\theta)T(x - x_0, y - y_0; x_0, y_0)R(\theta)g_0^{-1})^{-1}. \tag{2.25}$$

This equation is read as first transforming $g$ to $C_s$ ($g_0^{-1}$), transforming the result to the tilt axes reference frame ($R(\theta)$), operating with $T(\alpha, \beta; \alpha_0, \beta_0)$ ($T(x - x_0, y - y_0; x_0, y_0)$), transforming back to the sample reference frame ($R(-\theta)$) and finally transforming the result back to $C_c$ with the final inversion.

Although somewhat complicated, the transformation in Equation 2.25 is extremely useful for automating the search for particular zone axes, as will be shown in subsection 4.2.5.

### 2.4.2 Selected Area Diffraction

Selected area diffraction (SAD) is a technique in which a selected area aperture is inserted in an image plane. This aperture is placed so that it selects out a particular area on the sample, from which a diffraction pattern is to be obtained. The beam is then spread by the second condenser lens in the illumination system, so that the beam is the most parallel to the optical axis, resulting in sharp diffraction peaks in the back focal plane. The back focal plane is projected down to the screen to record the diffraction pattern. When the sample is tilted to a low index zone axis, the diffraction pattern will be symmetric, and it is relatively easy to label the reflections ($hkl$) manually. Figure 2.6 shows two SAD patterns of $ErMnO_3$ where Figure 2.6(a) was captured close to the [010] zone axis and two non-collinear reflections are annotated. For Figure 2.6(b) the sample was not tilted to a low index zone axis and the pattern is therefore irregular so that labeling reflections is difficult.

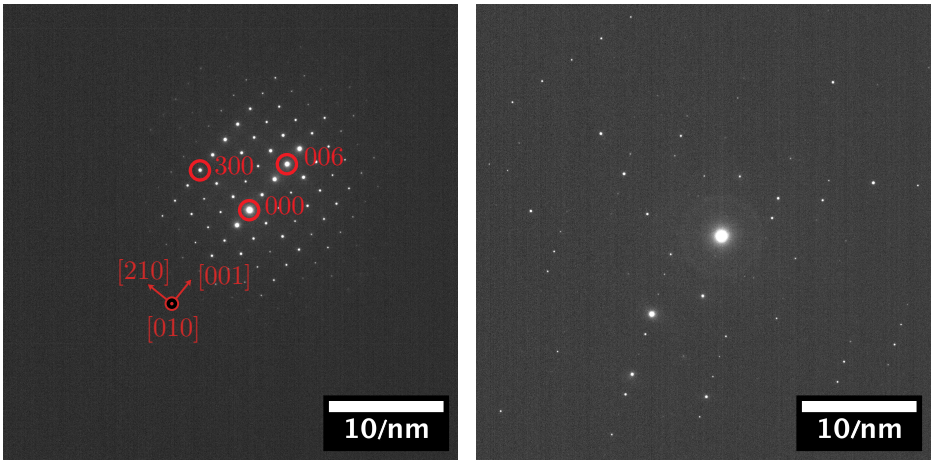


(a) (b)

Figure 2.6: Two SAD patterns of $ErMnO_3$ captured (a) close to the [010] zone axis, and (b) not on a low index zone axis. The annotation in (a) label the zero reflection, 000, and the reflections from two lattice planes, and the normal vectors $[uvw]$ to these planes.

Labeling two reflections in a SAD pattern is sufficient because the label of any other reflection can be found by a linear combination of the first two. The label for the two reflections can be found by manually searching for values of $hkl$ for which the relative interplanar distance (Equation 2.11) and the angle between the normal vectors (Equation 2.8) correspond to what is measured in the diffraction pattern. This search can be made semi-automatic with the aid of computer software such as ReciPro [26], but the results it provides should be checked manually.

In the project I did last semester, I showed that labeled SAD patterns can be combined with $T(\alpha, \beta; \alpha_0, \beta_0)$ to determine the crystallographic orientation of grains, and describe them in a common sample-tilt reference frame [15]. This was done by expressing the normal vectors of the labeled reflections in a Cartesian coordinate system and finding the rotation which aligns those vectors to their position in the reference coordinate system. Although this was somewhat useful, the process is quite tedious, and gave no real benefit compared to template matching on SPED data. For these reasons, SAD will in this thesis only be used to determine the zone axis of grains.

Instead of a parallel electron beam illumination, a convergent beam can be used for diffraction to get a convergent beam electron diffraction (CBED) pattern. The convergent electron probe results in diffraction disks (rather than the points in SAD, see Figure 2.6), and gives diffraction information from a more localized area compared to SAD. CBED has some advantages over SAD like higher sensitivity to thickness, but the theory of CBED is not addressed further in this thesis.

### 2.4.3 Bright-Field, Dark-Field and HRTEM Imaging

Dark-field (DF) imaging in TEM is a powerful technique with strong orientation dependent contrast which can be used to determine which parts of a sample scatter electrons to a particular reflection [24]. This can be useful in imaging precipitates in a sample where the intensity in a normal bright-field image might be dominated by the matrix as whole. A DF TEM image is taken by inserting an objective aperture in the back focal plane of the microscope. The aperture is positioned so that it selects out a particular reflection from the sample. To avoid the many aberrations present away from the optical axis, the objective aperture is usually kept in the center, and the beam is tilted to move a reflection of interest to

the center of the aperture. When the image plane is projected down to the screen, only parts of the sample which scattered to the chosen reflection will be bright. If the (000) reflection is selected using the objective aperture, the result is a bright-field (BF) image which is more intense than DF images and has better contrast compared to images without an objective aperture.

If a large, or no objective aperture is used, the direct and diffracted beams can interfere, and a phase contrast image related to the lattice is formed. This is called high resolution TEM (HRTEM) imaging and is used for this thesis, but the theory of lattice phase images is not addressed further here.

### 2.4.4 Scanning TEM Techniques

Scanning transmission electron microscopy (STEM) is a different way of operating a TEM, in which the electron beam is focused on the sample, rather than hitting it parallel. The electron beam thus becomes a probe with a convergence angle $\alpha$, and the area on the specimen from which the signal is obtained will be localized. The beam is scanned in a raster-like pattern to produce an image. This is done by shifting the beam by scanning coils above the specimen, and the recorded intensity at the detector corresponds to the pixel value at that position. Magnification and resolution is determined by the distance between points in the raster and the beam diameter on the specimen.

There are different types of STEM including bright-field (BF), annular dark-field (ADF), and high-angle ADF (HAADF). The difference between these are what scattering angles are collected by the detector, and for this work HAADF-STEM will be used. As the name suggests, HAADF collects the electrons that are scattered though high angles (>50 mrad, $\sim 3^\circ$). HAADF-STEM images are sometimes referred to as Z-contrast images because the contrast in images is highly dependent on the atomic number of the specimen ($I \propto Z^{1.7-2}$ [27]). With HAADF-STEM, high resolution lattice images are obtained with a small enough (sub-atomic spacing) step and probe size, but the image formation mechanism is fundamentally different from HRTEM because the image is formed incoherently by counting strongly scattered electrons at the different probe positions in the scan and not by interference between the direct and diffracted beam.

Instead of recording the intensity as a single value for each probe position in the scan (as in STEM) the diffraction pattern from that area could be projected down and captured by a pixelated detector. This way, a 4D dataset of the specimen is obtained, where associated with each probe position, there is a 2D diffraction pattern. This is known as scanning electron diffraction (SED), or sometimes referred to as 4D-STEM. An image of the specimen can be formed by integrating the intensity of (part of) the diffraction pattern associated with each pixel, collapsing the 4D dataset down to 2D. Theoretically, a diffraction pattern consists of mathematical points, but due to the convergence angle of the beam, the diffraction reflections in a scanning dataset are disks instead.

SED patterns contain large amounts of information about the sample such as crystal phase and orientation. However, the patterns are based on dynamical electron diffraction, making interpretation of the reflection intensities more complicated. For template matching, it is desired to have simpler (i.e. more kinematic like) diffraction patterns that are easier to work with. To simplify the diffraction pattern, the dynamical effects may be reduced by precessing the beam [28]. This technique is called scanning precession electron diffraction (SPED). In SPED, the probe is not only scanned across the sample, but also tilted by an angle $\phi$ away from the optical axis, and precessed around the optical axis in a full circle, at each point in the raster scan. An image of the diffraction pattern is captured as the probe undergoes $n$ full revolutions ($n = 1, 2, 3 \dots$), so that an average diffraction pattern over the

inclination angles is recorded for each probe position [29]. This type of diffraction pattern is called a precession electron diffraction (PED) pattern. In recording the PED patterns, it is important to adjust the exposure time of the detector to be a whole number of precession revolutions. Otherwise, the intensity distribution of reflections would be asymmetrically distributed. For instance, if the beam is precessing with a frequency of 100 Hz, the exposure time of the camera should be a whole number times the 10 ms the electron beam uses on a complete revolution. Although dynamical effects are very much still present in SPED, the precession tends to make PED patterns more kinematic like [29]. When SPED and SED are referred to together, the notation S(P)ED will be used in this report.

As the tilted probe rotates around the optical axis, the center of the Ewald sphere also moves around in a circle in reciprocal space. As the center of the Ewald sphere moves around, the sphere samples different parts of reciprocal space. Thus, after a full rotation around the optical axis, the average diffraction pattern will contain more diffraction reflections, compared to SED, as shown in Figure 2.7. Precession also removes any fine structures within the reflection disks, and reduces intensity variations due to sample thickness. All this makes the diffraction patterns easier to interpret, however the benefits of SPED comes at the cost of spatial resolution because as the tilted beam precesses, it samples a larger volume in the specimen than it would without precession.

The tilting of the probe away from the optical axis will also shift the entire diffraction pattern on the detector camera. For the averaging of diffraction patterns from the rotation to make sense, the beam needs to be descanned under the sample, by another set of scanning coils. Examples of SPED diffraction patterns without descan are presented in Appendix A (Figure A.1), which can be used to measure the precession angle.

Experimentally, the TEM column needs to be aligned for SPED by adjusting the scanning and descanning coils so that the sample plane, beam pivot point plane, and probe crossover plane all coincide (this is further described in section 3.3). This can be a challenge for large ($> 1°$) precession angles, but is crucial to do properly for the success of the method. As the sample plane needs to coincide with the beam pivot point plane and probe crossover plane, scanning large areas at high sample tilts can be problematic as the specimen height will be different across the scan. It is also important to perform the alignment at the desired precession angle and frequency as the alignment parameters will vary greatly with precession angle and frequency [30].

### Virtual Bright- and Dark-Field

Virtual bright-field (VBF) and virtual dark-field (VDF) images can be generated from S(P)ED data. While in conventional DF-TEM a diffraction reflection is selected using a physical objective aperture in the back focal plane, the VDF images are generated using a virtual objective aperture (in data processing). That is, instead of calculating each pixel value in the image from the integrated intensity of the entire diffraction pattern corresponding to each pixel, the pixel value is the integrated intensity of a single reflection in the corresponding diffraction pattern. If the reflection that is chosen for integration is the direct beam, the result is a VBF image, while if other reflections are chosen, the result is a VDF image. Similar to normal BF- and DF-TEM images, the brighter parts of the VBF image scatter less electrons, and for VDF images, the brighter parts scatter more electrons to the chosen reflection. For SPED VDF, bending and thickness contrast are greatly reduced compared to normal BF-and DF-TEM images, and VBF and VDF images of SED data.

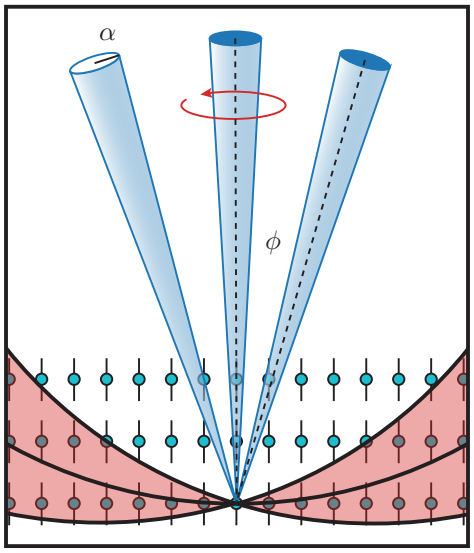


Figure 2.7: Schematic showing the effect of beam precession in SPED. The electron beam is represented by the blue cones with a convergence angle $\alpha$, and the grid of lines with blue circles are the reciprocal relrods of the crystal. In SED, only the center beam would hit the sample, and the corresponding Ewald sphere would intersect only a few relrods. By rotating the beam cone at an angle $\phi$ about the optical axis (as in SPED), the Ewald sphere is moved around in a circle in reciprocal space, and thus intersects a greater number of relrods as all the relrods in the red tinted area intersects the Ewald sphere at some point.

### 2.4.5 Electron Energy Loss Spectroscopy

Electron energy loss spectroscopy (EELS) is an experimental technique in TEM where the energy loss of electrons are recorded after they have interacted with the sample. In the electron-sample interaction, some electrons will interact inelastically with the sample, meaning they loose some of their energy. The inelastic interactions include phonon and plasmon excitations, inter- and intra-band transitions, inner shell ionizations and more [31].

An EELS spectrum typically records a range of energy loss typically up to max 2000 eV. A schematic of such an EELS spectrum is shown in Figure 2.8. The schematic loss spectrum is plotted with energy loss along the horizontal axis, and electron counts on the vertical axis. The EELS signal is often classified into the low-loss and high-loss (core-loss) regions [31]. In the low-loss region, which typically reaches up to about 50-100 eV, the first and main peak is the zero loss peak (ZLP) and represents electrons that transmitted through the sample with no measurable energy loss. This includes unscattered electrons, electrons scattering elastically or exiting phonon modes. The width of the zero loss peak relates to the energy spread of the electron gun in the TEM. The further peaks in the low-loss region represent plasmon excitations. The low-loss shoulder of the ZLP contains information about the band structure and dielectric properties of the sample, and the ratio between the ZLP and the plasmon peaks is related to the thickness of the sample [31].

In the high-loss region of the EELS spectrum (over 100 eV energy loss), the signal intensity decays rapidly, and it is often plotted on a logarithmic scale (see Figure 2.8). This region contains ionization edges superimposed on top of the decaying background due to inner shell ionizations in the sample. The energy of the ionization edges is characteristic of the elements in the sample, and can therefore be used for chemical characterization [31].

As the chemical composition of the $ErMnO_3$ sample in this work is known, the low-loss region is here of most interest. EELS is often combined with a scanning focused probe

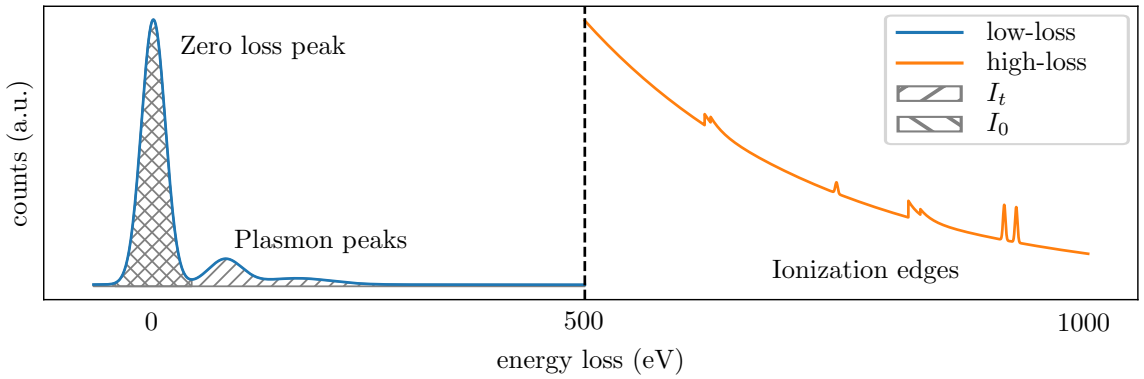


Figure 2.8: Schematic of an electron energy loss spectrum. The low-loss region extends to about 50-100 eV and contains the zero loss peak and plasmon excitations. The high-loss region is plotted on a logarithmic scale and contains ionization edges characteristic of the elements in the sample. $I_0$ and $I_t$ are the integrals of the zero loss peak and the entire spectrum, respectively.

to obtain a spectrum from each probe position. This allows for spatially resolved EELS mapping [31].

Experimentally, the energy of the electrons after interacting with the specimen are measured by sending the electrons through a static magnetic field perpendicular to the electron path. The magnetic field acts as a prism which, through the Lorentz force, disperses the different electrons by their kinetic energy. The dispersed electrons can then be counted on a CCD camera, where one axis of the camera represent the electron energy. The EELS spectrum is thus obtained by calculating the energy loss $(E_0 - E_f)$, where $E_0$ is the initial electron energy and $E_f$ is the recorded electron energy, and plotting it against the counts on the camera.

The thickness of a sample may be measured with the "Log-ratio Method" [31]. From simple Poisson statistics, it can be shown that the thickness, $t$, of a sample is related to the ratio between the number of inelastically and elastically scattered electrons. This relation is described by

$$t/\lambda = \ln I_t/I_0, \tag{2.26}$$

where $\lambda$ is the mean free path of electrons in the material, and $I_t$ and $I_0$ are the areas under the whole EELS spectrum and under the zero loss peak, respectively (see Figure 2.8).

The value of $\lambda$ needs to be determined in order to compute the absolute thickness. A crude estimate for $\lambda$ is simply $0.8E_0$, where $E_0$ is the initial electron energy in keV, and the result is in units of nm [31]. This estimation is often used when the composition of the specimen is unknown. In the present case, the composition of the specimen is known, and the value of $\lambda$ can be estimated more accurately.

It has been found empirically that the mean free path, $\lambda$ can be estimated as

$$\lambda \approx \frac{106F(E_0/E_m)}{\ln\left(2\beta E_0/E_m\right)} \tag{2.27}$$

where $\lambda$ is in units of nm, $\beta$ is the collection angle in mrad, $E_0$ is the initial electron energy in keV, $F$ is a relativistic factor given by

$$F = \frac{1 + E_0/1022 \text{ keV}}{(1 + E_0/511 \text{ keV})^2} \approx 0.618 \text{ at } E_0 = 200 \text{ keV}. \tag{2.28}$$

Finally, in Equation 2.27, $E_m$ is a factor dependent on the effective atomic number, $Z_{\text{eff}}$, in the sample. It has been proposed given as

$$E_m \approx 7.6 Z_{\text{eff}}^{0.36}, \qquad Z_{\text{eff}} = \frac{\sum_i f_i Z_i^{1.3}}{\sum_i f_i Z_i^{0.3}}, \tag{2.29}$$

where $f_i$ is the atomic fraction of each element of atomic number $Z_i$.

With Equation 2.26 and Equation 2.27, the thickness of a sample may be estimated. The method has been found to be accurate to about $\pm 20\%$ [31].

In the derivation of Equation 2.27, a few key assumptions were made, specifically that the convergence and collection angles are quite small (<10 mrad at 200 kV). This assumption will not hold true for the EELS spectra that were used to determine specimen thickness in this thesis. Iakoubovskii *et al.* [32] proposed a different approximation for $\lambda$

$$\lambda \approx \frac{200 F E_0}{11 \rho^{0.3}} \left( \ln \left( \frac{\alpha^2 + \beta^2 + 2\theta_{\text{E}}^2 + \delta^2}{\alpha^2 + \beta^2 + 2\theta_{\text{c}}^2 + \delta^2} * \frac{\theta_{\text{c}}^2}{\theta_{\text{E}}^2} \right) \right)^{-1}, \tag{2.30}$$

where $\alpha$ and $\beta$ are the incident convergence semi-angle and collection semi-angle in mrad, $\delta = |\alpha^2 - \beta^2|$, $\theta_{\text{c}} = 20$ mrad, $\rho$ is the density of the sample in g cm$^{-3}$, $E_0$ is the initial electron energy, $F$ is again defined by Equation 2.28 and $\theta_{\text{E}}$ is a characteristic angle given by

$$\theta_{\text{E}} = 5.5 \rho^{0.3} / (F E_0). \tag{2.31}$$

With the experimental parameters that will be used for EELS in this thesis, the approximation for $\lambda$ in Equation 2.30 will be most applicable. Still, the accuracy of the determined thickness is only about $\pm 20\%$.

## 2.5 TEM Micrograph and Electron Diffraction Simulations

TEM micrographs and diffraction patterns can be hard to interpret as the final result often is a complicated convolution of the electron-sample interactions, and aberrations of the microscope itself. The key challenge is to disentangle these effects so that as much information about the sample can be extracted from micrographs or diffraction patterns, while ignoring artifacts arising from the electron optics. In this process, TEM simulations can be of great aid. In this section, a brief introduction to TEM micrograph and electron diffraction simulations will be given with emphasis on the multislice solution. The theory presented here is based on *Advanced Computing in Electron Microscopy* by Kirkland [33].

TEM micrograph simulations have a long and rich history starting with Bethe who first discussed dynamical electron diffraction in 1928 [34] even before electron microscopes were invented. Over the years, two main approaches for simulating TEM results have emerged: The Bloch wave eigenvalue solution, and the multislice solution [33]. Broadly speaking, the Bloch wave eigenvalue solution involves expanding the quantum mechanical electron wave in the basis of Bloch waves, which satisfy the Schrödinger equation inside the periodic potential of the crystalline specimen, and solving the Schrödinger equation with appropriate boundary conditions to find the wave function as it exits the sample. The multislice solution, on the other hand, solves the problem by slicing the sample into a number of slices, where each slice acts kinematically, and the incoming wave to each slice is the outgoing wave from the previous slice.

There are advantages and disadvantages to both approaches for simulating TEM results. Although the Bloch wave solution can have analytical solutions for very simple crystals, both

the Bloch wave solution and the multislice solution generally need to be solved numerically. It is therefore fruitful to compare the two approaches in terms of their computational efficiency. The direct solution of a matrix equation such as the Schrödinger equation used in the Bloch wave solution scales as $N^3$, while the multislice solution, which employs the fast Fourier transform, scales as approximately $N \log_2 N$ [33]. The multislice solution is therefore much more efficient at larger and more complex problems. It is also more flexible in terms of solving complex structures such as interfaces or lattice defects. One benefit of the Bloch wave solution is that it generally produces more accurate results for higher order Laue zones (HOLZ). The multislice algorithm will be used for simulating TEM results in this thesis, specifically CBED and PED patterns, and is therefore treated in more detail below.

### 2.5.1 The Multislice Solution

In the multislice solution to TEM micrograph simulations, the specimen is divided into a number of thin slices along the direction of the electron beam, as shown schematically in Figure 2.9(a). The slices are thin enough to be treated as simple two-dimensional phase objects separated by $\Delta$z, so the propagation between slices can be treated as free space Fresnel diffraction. The multislice algorithm works by iteratively calculating the effect of the phase object on the electron beam incoming to a slice, and propagating the solution onto the next slice.

More formally, the multislice algorithm starts by solving the Schrödinger equation for the full wave function $\Psi_f(x, y, z)$ in the potential $V(x, y, z)$ of a slice of the specimen.

$$\left(-\frac{\hbar}{2m}\nabla^2 - eV(x, y, z)\right)\Psi_f(x, y, z) = E\Psi_f(x, y, z). \tag{2.32}$$

Through a series of approximations and assumptions such as the full wave equation being a product on the form $\Psi_f(x, y, z) = \Psi(x, y, z)\exp\{2\pi iz/\lambda\}$, where $\lambda$ is the wavelength of the electrons, and $\Psi(x, y, z)$ varies slowly with $z$, and assuming the slices are sufficiently thin, it can be shown that

$$\Psi_{n+1}(x, y) = p_n(x, y, \Delta z_n) \otimes (t_n(x, y)\Psi_n(x, y)) + \mathcal{O}(\Delta z^2), \tag{2.33}$$

where $p_n(x, y, \Delta z_n)$ and $t_n(x, y)$ are the propagation and transmission operators which take the wavefunction at slice $n$ to slice $n+1$, and $\Delta z_n$ is the thickness of that slice [33]. The symbol $\otimes$ represents convolution. This way, the wavefunction at slice $n+1$ is the interference pattern from the wave exiting slice $n$ (see Figure 2.9(b)).

The propagation function from one slice to the next is the free space propagator

$$p_n(x, y) = \exp\left\{\frac{i\lambda\Delta z_n}{4\pi}\nabla^2_{xy}\right\} \tag{2.34}$$

and the transmission function is given by

$$t_n(x, y) = \exp\left\{i\sigma\int_{z_n}^{z_n+\Delta z_n} V(z, y, z')\,\mathrm{d}z'\right\} \tag{2.35}$$

where $\sigma = 2\pi me\lambda/h^2$.

Depending on the type of simulation, the wavefunction $\Psi_0$ at $z = 0$ is set to either a plane wave for conventional TEM simulations, or a probe wave for STEM like simulations. With repeated application of Equation 2.33, the electron wave at any depth (in discrete steps of $\Delta z$) of the sample can be calculated.

The process of implementing the multislice solution efficiently requires some care and often utilizes the fast Fourier transform, turning the convolution in Equation 2.33 into multiplication through the convolution theorem. Equation 2.33 then becomes

$$\Psi_{n+1}(x,y) = \mathrm{FT}^{-1}\{P_n(k_x,k_y)\mathrm{FT}\{t_n(x,y)\Psi_n(x,y)\}\} + \mathcal{O}(\Delta z^2), \tag{2.36}$$

where FT{} is the two-dimensional Fourier transform and $P_n(k_x,k_y)$ denotes the Fourier transform of Equation 2.34.

Although the equations of the multislice solution are somewhat cumbersome, using premade software which implements the multislice solution is quite straightforward. The software is provided with a model of the unit cell, and simulation parameters such as the thickness are set. One thing to note is that because the fast Fourier transform is used, most software only accept an orthorhombic (rectangular) unit cell. This is of course a problem for simulating TEM results of samples with non-orthorhombic unit cells. In most cases, however, it is possible to redefine a larger unit cell that is rectangular.

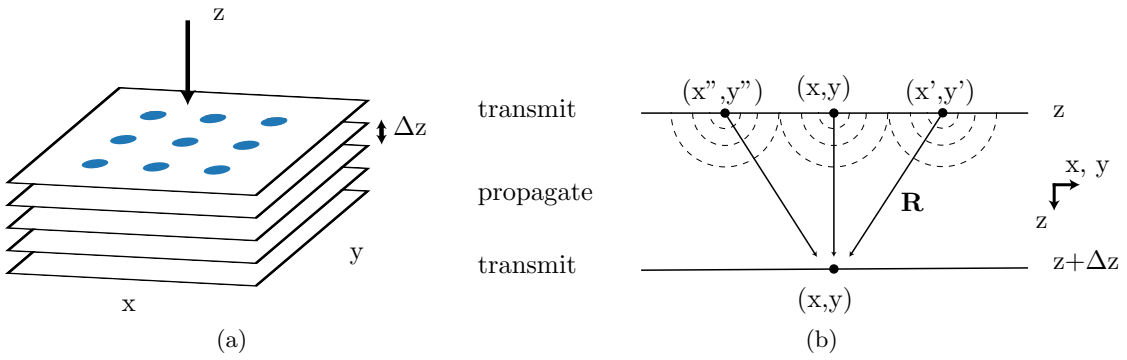


Figure 2.9: (a) In the multislice solution to TEM micrograph simulations, the sample is divided into thin slices along the direction of the electron beam separated by $\Delta z$. (b) The simulation iteratively calculated the effect of transmitting the electron wave through a slice and propagating the result to the next slice so that the wave at $z + \Delta z$ is the interference pattern from all the waves coming from the slice at $z$. This figure is inspired by figure 6.5 and 6.6 in Kirkland [33].

### 2.5.2 Images vs. Diffraction Patterns

Once the multislice solution has been used to calculate the wavefunction as it leaves the sample, the question still remains how this wavefunction relates to what is recorded by the detector. It is in this step there is a difference depending on what type of result is being simulated. The transmitted wavefunction is imaged by the objective lens of the microscope. For diffraction mode such as convergent beam electron diffraction (CBED), the back focal plane of the objective lens is projected to the camera, while in imaging mode, an image plane of the objective lens is projected to the camera.

The effect of the objective lens can be modeled through its transfer function $H_0(\mathbf{k})$

$$H_0(\mathbf{k}) = \exp\{-i\chi(\mathbf{k})\}A(\mathbf{k}) \tag{2.37}$$

$$\chi(\mathbf{k}) = \pi\lambda\mathbf{k}^2(0.5C_s\lambda^2\mathbf{k}^2 - \Delta f) \tag{2.38}$$

where $\Delta f$ is defocus, $C_s$ is the coefficient of spherical aberration, and $A(\mathbf{k})$ is the aperture function of the objective aperture (1 for $\lambda\mathbf{k} < \alpha_{\max}$ and 0 otherwise). $\chi(\mathbf{k})$ here is a simplified example of the aberration function of the objective lens, more extended aberration functions would also include other aberration such as chromatic aberrations. [33].

Given that the wavefunction as it leaves the sample is $\Psi_t(\mathbf{r})$, the image wavefunction in the back focal plane of the objective lens is

$$\Psi_i(\mathbf{k}) = \mathrm{FT}\{\Psi_t(\mathbf{r})\}H_0(\mathbf{k}). \tag{2.39}$$

A simulated diffraction pattern is the absolute square of this

$$I(\mathbf{k}) = |\Psi_i(\mathbf{k})|^2. \tag{2.40}$$

Simulating real space images involves the inverse Fourier transform back to real space

$$I(\mathbf{r}) = |\mathrm{FT}^{-1}\{\Psi_i(\mathbf{k})\}|^2. \tag{2.41}$$

### 2.5.3 Frozen Phonon Approximation

Most TEM analysis is carried out at room temperature (300 K) and atoms in a sample are vibrating. These small deviations from their equilibrium position will influence the intensity distribution in images and diffraction patterns in the TEM. In multislice simulations, however, the simulation is provided with a model of the sample where all the atoms are perfectly still in their equilibrium position. The frozen phonon approximation is a method for including the thermal vibrations of atoms in the simulation. The optical phonons in most materials vibrate at most at frequencies around $10^{12}$ to $10^{13}$ Hz. The electrons in the TEM, on the other hand, are traveling at about half the speed of light, and only spends approximately $0.7 \times 10^{-16}$ s inside the sample, which is much less than the period of oscillation for the phonons. The atoms in the sample thus appear stationary to the imaging electrons. This observation is the key to the frozen phonon approximation in multislice simulations. In this approximation, the atoms in the sample are displaced randomly a tiny amount from their equilibrium position, and left stationary there when running the simulation. The final simulated image or diffraction pattern is the average of multiple such random displacements and simulations [33].

## 2.6 Data Processing

In the following section, a few useful concepts in image processing are introduced and a method for finding crystallographic orientations through template matching on S(P)ED datasets is described. The data processing is done using the open-source Python packages HyperSpy[35], Orix[21, 22] and Pyxem[36, 37]. The goal the data processing is to acquire and quantify as much information from the collected data as possible.

### 2.6.1 Image Contrast

The contrast in an image is the difference in luminance or pixel intensity which make objects distinguishable from the background. Higher contrast is in images makes the objects more visible. Contrast can be defined in many ways. In this thesis, contrast between ferroelectric domains will be calculated in VDF images. The domains appear as bright and dark regions in the image, and for these types of images the Michelson contrast is useful [38]. It is defined as

$$C_m = \frac{I_H - I_L}{I_H + I_L}, \tag{2.42}$$

where $I_H$ is the luminance of the bright region and $I_L$ is the luminance of the darker region. The Michelson contrast is a unitless number between 0 and 1, where 0 is no contrast 1 is the highest possible contrast.

### 2.6.2 Normalized Cross Correlation

The normalized cross-correlation (NCC) is a number describing how similar two images, or regions of images are. NCC can be used in a range of different applications such as object recognition and convolutional neural networks, and is generally defined as a convolution between an image and a kernel. In this thesis, NCC will be used to measure the similarity between two images of the same size, and so the kernel will be the second image. The NCC score between two images $I_0(x, y)$ and $I_1(x, y)$ is defined as

$$\mathrm{NCC}(I_0, I_1) = \frac{\sum_{x,y}(I_0(x,y) - \bar{I_0})(I_1(x,y) - \bar{I_1})}{\sqrt{\sum_{x,y}(I_0(x,y) - \bar{I_0})^2 \sum_{x,y}(I_1(x,y) - \bar{I_1})^2}}, \tag{2.43}$$

where $\bar{I}$ is the average intensity of the image. The NCC score is sometimes referred to as zero-normalized cross-correlation and has a range between -1 and 1. The NCC of an image with itself is 1.

### 2.6.3 Template Matching on S(P)ED

Template matching is a brute force method for determining the crystallographic orientation of a crystalline material [37]. The method uses a S(P)ED dataset to compare the diffraction patterns with a library of simulated diffraction patterns. The library contains simulated diffraction patterns of the known sample material in all possible orientations. The simulated diffraction pattern most similar to the experimental diffraction pattern thus determines the crystallographic orientation. A flowchart of template matching is presented in Figure 2.10.

#### Cross Correlation

The S(P)ED datasets are often large, on the order of several to several tens of GB, and contain many thousands of diffraction patterns. In addition, the library of simulated diffraction patterns also contain thousands of entries, depending on the angular resolution chosen for the simulation. Comparing the two datasets manually is therefore not feasible, and an automatic procedure is required.

The automatic procedure needs to be some function which takes in an experimental diffraction pattern, along with a library of potential matching patterns, and determines a score for each library entry so that the highest scoring library entry is chosen. A severe restriction to the methods is computational power, thus although many image correlation functions like Equation 2.43 exist, most of them are too computationally expensive to be feasible here.

The correlation score given in the equation below turns out to be a good balance between computational lightness, and accuracy in the calculated score [37, 39]. The score is defined as

$$Q = \frac{\Sigma_i P(x_i, y_i) T(x_i, y_i)}{\sqrt{\Sigma_i P(x_i, y_i)^2} \sqrt{\Sigma_i T(x_i, y_i)^2}}, \tag{2.44}$$

where $P(x, y)$ are the pixel values of the experimental diffraction pattern, and $T(x, y)$ represent the pixels of the simulated diffraction pattern. $Q$ is similar to Equation 2.43, but

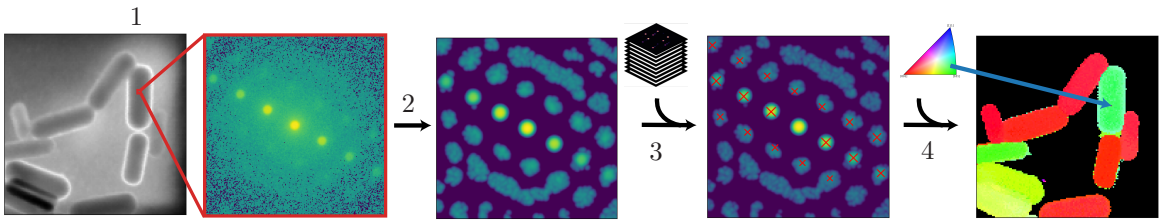


Figure 2.10: Flowchart showing the steps of template matching for finding crystallographic orientations. In order to find the orientation of a given pixel in the scan (1), the corresponding diffraction pattern is preprocessed to center it and remove noise (2), and then compared to a library of simulated diffraction patterns (3). The orientation is visualized here with a Z projected inverse pole figure (4). The data used in this figure is a SPED dataset of gold nanoparticles.

the average is not subtracted in the summations. The summations are further kept computationally inexpensive by generating the simulated diffraction patterns extremely sparse, so that the only non-zero elements are the centers of the diffraction reflections. This way, the summation in the numerator of Equation 2.44 only contains as many elements as there are reflections in the simulated diffraction pattern, and the number of multiplications and additions required for the calculation is greatly reduced.

### Preprocessing

Because the cross correlation score is an extremely sparse summation, it is also very susceptible to noise in the experimental diffraction patterns. Preprocessing of the S(P)ED dataset is therefore crucial for the success of the template matching.

To reduce the effect of noise the background in each diffraction pattern is subtracted through a Difference of Gaussians background subtraction, followed by a series of Gaussian blurring and thresholding.

Due to small misalignments of the microscope and shifts from electron-sample interactions, the diffraction pattern will shift slightly between probe positions. This is a problem because the simulated diffraction patterns are perfectly centered, and will thus never correlate well with an off center experimental diffraction pattern. The first step in the preprocessing is therefore to center the zero reflection for all experimental diffraction patterns.

### Library Generation

The library of simulated diffraction patterns is generated using the simple kinematic approximation (Equation 2.15). The inputs to the simulation include the angular resolution, diffraction calibration, an excitation error specifying how close to the exact diffraction condition a relrod needs to be before it is included, and the minimum intensity for a reflection not to be counted as extinct. The simulation also features a parameter representing precession angle, but since the simulation is kinematic, it likely is not directly related to experiments, and has much the same effect on the simulated diffraction patterns as changing the excitation error.

In general, the library of simulated diffraction patterns should sample all of orientation space (SO(3) group), however at a reasonable angular resolution, this would result in a very large library. The size of the library can be drastically reduced by only simulating diffraction patterns in the symmetry reduced orientation space. Furthermore, in the Bunge convention of Euler angles, all orientations with the same $\Phi$ and $\phi_2$ are related through an in-plane rotation. The size of the library is thus reduced further by only sampling $(\Phi, \phi_2)$, and the $\phi_1$ component of the Euler angles is found by in-plane rotations of the simulated diffraction

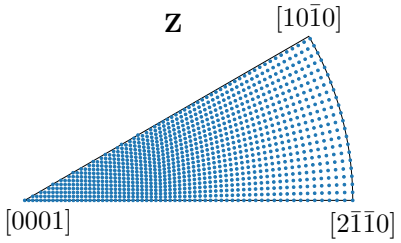


Figure 2.11: The 1050 unique orientations sampled when generating a library for template matching using the `spherified_cube_edge` method and an angular resolution 2°.

patterns in the indexation process. Pyxem, which is used for template matching, supports a range of different ways to sample orientation space for the library generation. In this thesis, the `spherified_cube_edge` method was used. An example of the sampling with this method and a resolution of 2° is shown in Figure 2.11. With this angular resolution, 1050 unique orientations are sampled. For the angular resolution that was actually used in template matching, 0.3°, 44740 unique orientations are sampled.

## 2.7 $ErMnO_3$

Erbium manganite ($ErMnO_3$) is part of a class of functional materials known as hexagonal manganites with the general formula h-$RMnO_3$ (R = Sc, Y, In, Dy, Er). Hexagonal manganites can exhibit a range of interesting properties including ferroelectricity, ferromagnetism, multiferroicity and charged domain walls [40].

### 2.7.1 Crystal Structure

The hexagonal crystal structure of $ErMnO_3$ has $\mathbf{a}_1 = \mathbf{a}_2 = 6.115\,\text{Å}$, $\mathbf{a}_4 = 11.41\,\text{Å}$, and $\alpha = \beta = 90°$ and $\gamma = 120°$. The point group of $ErMnO_3$ is 6mm and the space group is $P6_3cm$ (at room temperature) [41, 42]. This point group is non-centrosymmetric, which is a requirement for ferroelectricity. However, because kinematic diffraction patterns are centrosymmetric, the Laue group symmetry of $ErMnO_3$, 6/mmm, will be used for inverse pole figures describing orientations.

$ErMnO_3$ can exist in different phases depending on temperature. Above 1429 K it is paraelectric with space group $P6_3/mmc$, and below it is ferroelectric. Below about 80 K the material has been reported to become ferromagnetic [43]. The room temperature version of $ErMnO_3$ is a p-type semiconductor with a narrow band gap of about 1.6 eV [44]. This means that the majority charge carries in the bulk are positively charged holes, with enthalpy stabilized interstitial oxygen anions being the main source of p-type conductivity [45].

A schematic of the $ErMnO_3$ unit cell is presented in Figure 2.12. The arrangement of atoms in the unit cell is quite complicated with 6 Er atoms, 6 Mn atoms and 18 oxygen atoms for a total of 30 atoms in the unit cell. This makes the analytical expression for the structure factor found through Equation 2.18 hard to analyze and simulations of diffraction patterns are often required.

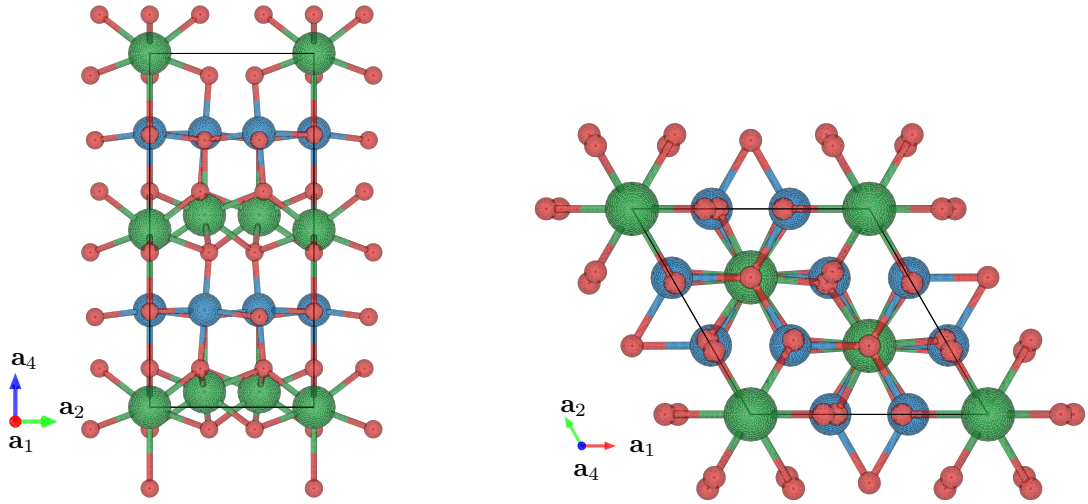


(a) (b)

Figure 2.12: Schematic of the $ErMnO_3$ unit cell at room temperature viewed along $\mathbf{a}_1$ (a) and $\mathbf{a}_4$ (b). The green atoms are erbium, the blue are manganese and the oxygen atoms are red. These figures are made in Vesta using a Crystallographic Information File (CIF) from Springer Materials based on the work of Yakel *et al.* [41, 42].

### 2.7.2 Ferroelectricity

As mentioned, $ErMnO_3$ is ferroelectric at room temperature. Ferroelectricity is a characteristic of a material that exhibits a spontaneous electric polarization that can be reversed by an applied electric field. The polarization arises by charged ions shifting along the polarization direction ($c$-direction) in the unit cell. This is similar to the more known ferromagnetism where the material exhibits a spontaneous magnetic polarization which can be reversed by a magnetic field. In traditional (also known as primary) ferroelectrics such as $BaTiO_3$, the ferroelectricity arises from softening of the polar distortion mode [40]. This essentially means that the overall energy is reduced by ions shifting along the polarization direction. Hexagonal manganites and $ErMnO_3$ is, however, not a traditional ferroelectric. In non-traditional ferroelectrics the ferroelectricity arises as a secondary effect of symmetry breaking caused by something else. In the case of $ErMnO_3$, which is an improper ferroelectric, a structural breaking of symmetry causes ferroelectric polarization along $\mathbf{a}_4$ [3, 40]. A consequence of ferroelectricity being a secondary effect is that the domain walls are flexible and charged domain walls form naturally. This would not be energetically favorable in proper ferroelectrics. Improper ferroelectrics tend to have a smaller polarization than the proper. The polarization of $ErMnO_3$ is about $6\,\mu C\,cm^{-2}$[3, 46]. The domain walls in $ErMnO_3$ can also meander and tend to be quite small on the order of a few unit cells.

#### Charged Ferroelectric Domain Walls

As ferroelectrics possess a spontaneous electric polarization, interesting interfacial effects can occur between domains of different polarization. Particularly interesting are the 180° domain walls naturally occurring in $ErMnO_3$. The configuration of such a domain wall could be head-to-head or tail-to-tail. A head-to-head configuration results in a positive charge at the domain wall, and tail-to-tail a negative charge. A schematic of this is shown in Figure 2.13(b) and (c). If the polarization is parallel to the wall as in Figure 2.13(a),

the domain wall will be neutral. In $ErMnO_3$, all these types of domain walls, and those in between (slanted domain walls) occur in the as-grown state.

To screen the electrostatic potential at charged domain walls, charged point defects and other mobile charge carriers tend to redistribute and are attracted or repelled by the domain wall depending on their charge. This can increase or reduce the conductivity along the domain walls substantially in comparison to the surrounding domains [3]. In $ErMnO_3$, which is a p-type semiconductor, enhanced conductivity at tail-to-tail domain walls has been reported, and is explained by the accumulation of mobile holes at the domain wall to screen the local diverging electrical field. Similarly, head-to-head domain walls exhibit a suppressed conductance due to depletion of the majority charge carries [47].

At the boundaries between crystallographic grains, a generalized version of bound charge at domain walls can occur. Instead of polarization pointing head-to-head or tail-to-tail, the polarization of the two grains can point in an arbitrary direction (assuming randomly oriented grains) as defined by the $c$-axis of the two grains. The bound surface charge density at a grain boundary is

$$\rho = (\mathbf{P}_2 - \mathbf{P}_1) \cdot \mathbf{n}, \tag{2.45}$$

where $\mathbf{P}_i$ are the polarizations of the two grains and $\mathbf{n}$ is the grain boundary normal vector pointing inside grain 1. [4, 14].

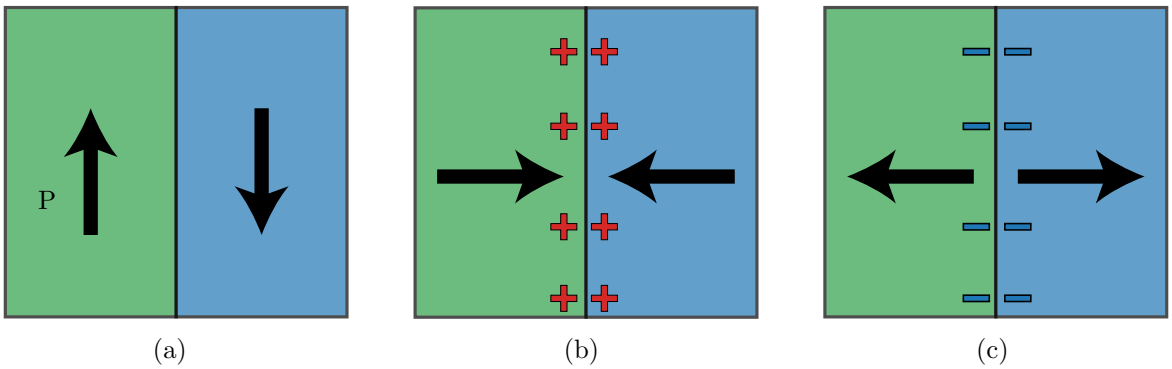


Figure 2.13: Schematic showing (a) a neutral, (b) a positively charged (head-to-head) and (c) a negatively charged (tail-to-tail) domain wall.

# Chapter 3

# Methods

This chapter introduces the experimental aspects of this project including a few notes on how the sample was synthesized and prepared for TEM investigations, a presentation of the three TEMs that were used and some details on the data processing and simulations used to obtain results. As the same specimen was studied with the same TEMs in this thesis as in the project report for TFY4520 [15], parts of this chapter are reused.

## 3.1 Sample Synthesis and Specimen Preparation

The bulk polycrystalline material, from which the investigated lamella was extracted, was made by a conventional solid-oxide synthesis routine. The powder synthesis, pressing and sintering procedure is described by Schultheiß *et al.* [13].

The sample synthesis was done by Dr. Jan Schultheiß. $Er_2O_3$ and $Mn_2O_3$ powders were dried for 12 hours at 900°C and 700°C, respectively, after which they were mixed stoichiometrically and ball milled for 12 hours. The mixed powder was then annealed stepwise at 1000°C, 1050°C and 1100°C for a total of 12 hours. Further, the powder was pressed isostatically into 10 mm pellets at 200 MPa. The pellets were sintered at a temperature of 1350°C for 10 minutes. This produced a sample with grain size on the order of around 1.5 µm. In this procedure, microcracking is unavoidable, but should not affect the as-grown ferroelectric domains as the microcracks form at a much lower temperature than the Curie temperature of $ErMnO_3$ [48]. Further details on the synthesis and material properties can be found in [13].

A thin lamella was extracted from the bulk $ErMnO_3$ polycrystal by Kasper Aas Hunnestad using a FEI Phoenix G4 focused ion beam (FIB) at NTNU NanoLab. First a protection layer was deposited by electron beam assisted Pt deposition (ca. 30 nm) followed by Ga ion assisted deposition of Pt for a few microns. The protection layer protects the original sample surface and gives more even milling rates resulting in a more even lamella thickness. The ion beam was then used at an acceleration voltage of 30 kV to mill out trenches around the desired part of the sample as well as underneath it, creating a lamella attached at one point to the bulk. A micromanipulator lift-out needle was attached to the lamella before complete separation. After extracting the lamella from the bulk using the micromanipulator, it was placed on a Cu half grid and welded in position by Pt deposition. The lamella was then thinned down to roughly 200 nm, before the acceleration voltage was reduced to 5 kV for the last thinning down to sub-100 nm. The low acceleration voltage and nearly parallel ion beam to the lamella during the thinning step reduces the risk of milling damage such as amorphization.

## 3.2 The Transmission Electron Microscopes

The three TEMs that were used for this thesis were a JEOL JEM-2100, a JEOL JEM-2100F, and a JEOL JEM-ARM200F. These will be referred to as the 2100, the 2100F and the ARM, respectively. All three TEMs are located at the TEM Gemini Centre/NORTEM-Trondheim node at NTNU, and operate at an acceleration voltage of 200 kV. The TEMs are differently configured and have different accessories (detectors, controls, support programs) optimized for different tasks. Before capturing any data on either of the TEMs, the microscopes were aligned following the standard principles of TEM alignment at the TEM Gemini Center Trondheim. With exception to the data from the ARM (which was recorded by Dr. Emil Frang Christiansen), all TEM data for this work was captured by the author.

#### JEOL JEM-2100

The 2100 was mainly used during the project report preceding this thesis [15] for conventional TEM (BF/DF, HRTEM and SAD). It is equipped with a $LaB_6$ filament electron gun and an Orius SC 200D CCD camera. Out of the three microscopes used in this thesis, the 2100 has the poorest spatial resolution and is mainly used for lower magnification TEM (up to around 200 000×).

#### JEOL JEM-2100F

The 2100F was used by far the most throughout this thesis, and all data when not explicitly stated otherwise was captured on it. It is equipped with a field emission gun (FEG) with an energy spread of 0.7 eV. The 2100F is equipped with two bottom mounted cameras: (i) a Gatan 2k UltraScan CCD camera which was mostly used for the conventional TEM techniques, and (ii) a 256×256 Medipix Direct Electron Detector from the QuantumDetectors Merlin system. This camera supports 1, 2, 6, 12, and 24 bits of dynamical range.

SPED is made possible on the 2100F through the NanoMegas Scanner and Digistar Control software hardwired to the scan board.

#### JEOL JEM-ARM200F

The ARM is a double aberration corrected TEM meaning it has a probe corrector above the specimen and an image corrector below it. The ARM uses a ColdFEG electron gun with an energy spread below 0.3 eV. For this thesis, the used detectors are the HAADF-STEM detector for imaging, and a Quantum GIF with DualEELS and a 2k CCD camera for EELS. HAADF-STEM and low loss EELS are used to verify results from simulations and data from the 2100F.

The operation of the ARM was done by Dr. Emil Frang Christiansen. All data from the ARM used in this thesis was captured in a single session, and before this session, the sample was cleaned in $O_2$ plasma for 3×10 s (Fishioni plasma cleaner model 1020).

### 3.2.1 Specimen Holder

The sample was placed in a Gatan double tilt sample holder. For the whole duration of this work, the sample was kept in this holder in the same position. This was done to ease correlating data from different sessions, operation modes and instruments. The Gatan double tilt holder can tilt the sample ±30° about two perpendicular tilt axes. In the 2100F, however, at $y$-tilts above about 17.5°, the sample could not be moved far enough in $z$ direction to

reach the standard focal plane of the objective lens. In this microscope, the effective range of sample tilt was therefore ±30° in $x$-tilt and only −30° to 17.5° in $y$-tilt.

## 3.3 S(P)ED Data Collection and Processing

### 3.3.1 Data Collection and SPED settings

The S(P)ED data was collected on the 2100F TEM. The microscope was aligned for SPED as described in detail by Barnard *et al.* [30], the key steps are given below. The alignment for SED is similar to SPED, but the steps 3.-7. are not required.

1. Align the TEM according to standard alignment procedure.
2. Switch to Nano Beam Diffraction (NBD) and redo the standard alignment procedure.
3. In diffraction mode, insert and center the 40 µm condenser aperture and over-focus the electron beam using the condenser lens (adjusting brightness).
4. Move to a region with large easily visible features and activate precession at the desired precession angle and frequency.
5. Make the BF-CBED disk static (have sharp edges) by descanning adjustments.
6. Minimize the motion in the shadow image within the BF disk by adjusting the pivot point.
7. Repeat step 5. and 6. iteratively and increase magnification (using the condenser lens / brightness) in each step until no further improvement can be made.
8. Turn off precession and adjust brightness until a Ronchigram is observed (preferably on amorphous region). Insert and center the 10 µm condenser aperture on the Ronchigram.
9. Blank the beam to avoid beam damage, move to region of interest, turn on precession and start scanning.

In the last step, moving to the region of interest can be challenging as SPED scans are slow, thus giving little feedback concerning region being scanned. SED with 1 bit dynamical range and 1 ms dwell time was therefore used to navigate to the region of interest. This fast SED scan was also used to adjust the camera length and center the diffraction pattern on the detector, after which the SPED data can be captured. The S(P)ED data in this thesis were collected in 12 bit mode with 10 ms exposure time if not stated explicitly different.

Many S(P)ED datasets with varying precession angles, step sizes and covering different regions of the sample were captured throughout this work. The alignment procedure described above was repeated before capturing all the datasets. This is especially important when the sample has been tilted, because this usually changes the sample height. The precession frequency for all collected SPED data was set to 100 Hz, the nominal probe size was set to 1 nm, and the nominal camera length was set to 12 cm. A smaller probe size can achieve better spatial resolution, but for the scans used in this thesis, the step size was the limiting factor for spatial resolution. The camera length was chosen so that the PED patterns covered a reasonable region on the detector.

#### Calibrations

The step size for the S(P)ED datasets were calibrated using recognizable features in the scans (for instance holes or grain boundaries) and conventional BF-TEM images. The BF-TEM images are calibrated from the microscope, and this calibration was assumed to be accurate. The scale bars in images from S(P)ED data are added manually using the calibrated step size. The reciprocal PED patterns were calibrated with tabulated values from the Wiki page of the TEM Gemini Centre (not publically available).

### 3.3.2 Data Processing

The data processing of S(P)ED data was done using the open-source Python libraries HyperSpy and Pyxem [35, 36]. HyperSpy has a range of useful functionality for plotting and analyzing multidimensional scientific data, and Pyxem builds on top of HyperSpy with emphasis on data from pixelated electron detectors. The HyperSpy `roi` module is especially useful when analyzing S(P)ED data, where a region of interest (roi) aperture of different shapes can be placed in either the navigation (real space) or the signal (reciprocal) space, and the dataset can be sliced inside this roi. Slicing the dataset with an roi in real space (summing the diffraction patterns within the roi) forms the basis for virtual selected area diffraction (VSAD). And the inverse, slicing the dataset with an roi in reciprocal space forms the basis for virtual bright- and dark-field (VBF, VDF) imaging. An roi in real space is referred to as a virtual selected area (VSA) aperture, and an roi in reciprocal space is referred to as a virtual objective aperture.

#### Template Matching

In the project report written by the author in the fall of 2022 [15], the parameters for template matching on S(P)ED data were optimized, both on the experimental data acquisition side and software data processing side. It was found that SPED with a 1° precession angle gave the best template matching results, and so this precession angle was used for all template matching in this thesis.

Template matching on the SPED datasets was performed using the methods described in subsection 2.6.3. For the preprocessing of the datasets, the diffraction patterns were centered using the `Blur` method in HyperSpy [35] with half square width of 10 and a sigma of 3. The background was subtracted using the `Difference of Gaussians` algorithm with $\sigma_{\min} = 3$ and $\sigma_{\max} = 6$. Noise was further reduced by a Gaussian blur with $\sigma = 0.5$, followed by thresholding at 1 and two more Gaussian blurs with $\sigma = 0.5$ and $\sigma = 1.3$, and finally another threshold at 0.3.

For the simulated diffraction patterns library generation used in template matching, an angular resolution of 0.3°, a minimum intensity of 0.0015, a max excitation error of 0.0125 and a precession angle of 0.3° was used[1]. The diffraction calibration for the simulation was set to 0.00952354965. The crystal structure information for the simulations was provided by a Crystallographic Information File (CIF) from Springer Materials based on the work of Yakel *et al.* [41, 42]. A logarithmic transformation was applied to the experimental SPED diffraction patterns before calculating the correlation score.

The output of the template matching in Pyxem is a phase and result python dictionary, which together encode the result of template matching including the crystal orientation in

[1] Although a precession angle of 0.3° does not match any of the experimental datasets, this parameter was chosen because it resulted in a simulated diffraction pattern appearing similar to the experimental diffraction patterns.

each probe position of the SPED scan (as Euler angles) and the correlation score. The further analysis of this output was done in the python based Orix library [21] and the Matlab based MTEX software package [23]. Pyxem has functionality for converting the phase and result dictionaries to Orix `CrystalMap` objects. The `CrystalMap` object can from Orix be saved as the standard .ang file format which can be loaded in MTEX. Between converting from the result and phase dictionaries to Orix `CrystalMaps` and loading the results to MTEX, careful consideration of the different definitions of orientations is required. The orientation result of template matching with Pyxem uses a different definition of the Cartesian coordinate system compared to Equation 2.9, namely the $\mathbf{e}_1 \| \frac{\mathbf{a}_1^*}{|\mathbf{a}_1^*|}$ definition is used. For the hexagonal unit cell of $ErMnO_3$, this difference results in the `CrystalMap` orientations being rotated 30° about $\mathbf{a}_4$, and so to compensate the orientations are rotated back 30°. When the .ang file is loaded in MTEX, this definition can be specified in the `crystalSymmetry` object.

In MTEX, detailed crystallographic analysis using the template matching result can be done, and the software has support for reconstructing the grains in the sample based on the similarity of orientations of neighboring pixels (i.e. image segmentation). This way, a mean crystallographic orientation for each grain can be calculated, and this mean orientation can be visualized as a unit cell plotted on top of each grain. MTEX was mostly used for these types of plots, and for calculating the mean orientation of grains. Further analysis of the mean orientations of grains was done in Python with Orix. When transforming the mean orientations from MTEX to Orix, the orientations were represented as quaternions. However, in loading the quaternions in Orix, the orientations need to be inverted because MTEX used the inverse definition of orientations compared to Equation 2.19, which is the one Orix uses.

## 3.4 PED Multislice Simulations

The simulations of PED patterns were made using the Pyms (py_multislice), which is an open-source python based simulation software [49]. Pyms has a range of different functions for simulating TEM results, including CBED patterns. To simulate PED patterns using Pyms, the `CBED` function in the `Premixed_routines` module was used. CBED is of course different from PED, however, the CBED simulation in Pyms allows for specifying a small beam tilt (<50 mrad) in any direction. The strategy for using the CBED simulation function for simulating PED is thus to simulate many CBED patterns, each with a beam tilt sampled discretely from a cone of beam tilts with a semi-angle of the desired precession angle (here, the experimental precession angle was used, not the 0.3° as for template matching), and then combining all the simulations to a single diffraction pattern. For the same reason the exposure time in experimental SPED needs to be a whole number times the precession period, the sampled beam tilts need to be symmetrically distributed around the beam tilt cone. That is, each of the total $N$ CBED simulations which combines to a PED simulation with a precession angle of $\phi$ uses a beam tilt $(\phi_x, \phi_y)$, where

$$\phi_x = \phi \cos(j\frac{2\pi}{N}), \qquad \phi_y = \phi \sin(j\frac{2\pi}{N}), \qquad j \in \{1, N\}. \tag{3.1}$$

CBED simulations with a beam tilt $(\phi_x, \phi_y)$ will result in a shift of the entire diffraction pattern. Thus, in order to meaningfully combine all the CBED simulations with different beam tilts, the diffraction patterns need to be centered, so that the direct beam remains in the center. That is, we need to also simulate the descan which is used when obtaining experimental SPED datasets. In order to simulate descan, the beam tilt $(\phi_x, \phi_y)$ needs to

be related to the number of pixels the corresponding simulation needs to be shifted. As Pyms is open source, it is easy to examine the code and reverse engineer the transformation required to center the diffraction patterns. In applying the transformation, all pixels that are shifted outside the simulated region are set to 0. This process is illustrated in Figure 3.1, and I have posted example code implementing it for Pyms to its GitHub page (https://github.com/HamishGBrown/py_multislice/issues/7).

In addition to beam tilt, the Pyms CBED multislice simulation supports a range of different simulation parameters. The parameters used in the PED simulations here are presented in Table 3.1. In this table, the slices describe how the unit cell is sliced for the multislice simulation. The gridshape influences the field of view in reciprocal space. Because of the recentering of the diffraction pattern, the field of view needs to be set higher for larger precession angles. Tiling refers to how many unit cells are tiled together in the simulation. The aperture describes the size of the image forming lens aperture in mrad, and controls the radius of the reflection discs in the simulation. This parameter was set to have diffraction discs of comparable size to the ones in the experimental SPED datasets. The number of iterations of the frozen phonon approximation is described by nfph, and $N$ is the number of samples of beam tilt according to Equation 3.1. The thickness of all the simulations was set to a range between 25 nm and 150 nm with a step size of about 0.42 nm (300 steps). In Pyms, the specimen thickness in the simulation is rounded of to a whole number times the length of the unit cell in the slicing direction.

The simulation also needs to be provided a model of the crystal structure. Like many other simulation software packages, Pyms only accept orthorhombic unit cells ($\alpha = \beta = \gamma = 90°$, $|\mathbf{a}_1| \neq |\mathbf{a}_2| \neq |\mathbf{a}_3|$). This is of course a problem as $ErMnO_3$ has a hexagonal unit cell. In addition, Pyms only allows for simulations along the $\mathbf{a}_3$ direction. Thus, the $ErMnO_3$ unit cell needs to be recasted to an orthorhombic unit cell with the desired zone axis along $\mathbf{a}_3$ of the new unit cell. This recasting was done using the JEMS software [50]. In JEMS, after loading the CIF file, "Crystal → Transform unit cell" was used, followed by pressing "matrix" and entering the desired rotation into the transformation matrix. Then "done" was pressed, and the transformed unit cell was exported. The resulting unit cell had a length in the slicing direction of 0.60 nm, which is the thickness resolution of the multislice simulations. Because this is longer than the 0.42 nm step size of the input thickness, some redundant simulations with the same thickness twice after rounding were made.

Table 3.1: Parameters of PED simulation using Pyms. The parameters are explained in the text, further details of the parameters are provided in the documentation of Pyms [49].

| Precession angle: | 0° (CBED) | 0.5° | 1° |
|---|---|---|---|
| Slices | [0.5, 1] | [0.5, 1] | [0.5, 1] |
| Gridshape | [1024, 1024] | [1024, 1024] | [2048, 2048] |
| Tiling | [32, 32] | [32, 32] | [32, 32] |
| Aperture | 1.23121 | 1.23121 | 1.23121 |
| nfph | 25 | 25 | 25 |
| $N$ | N/A | 100 | 100 |
| eV | 200 kV | 200 kV | 200 kV |

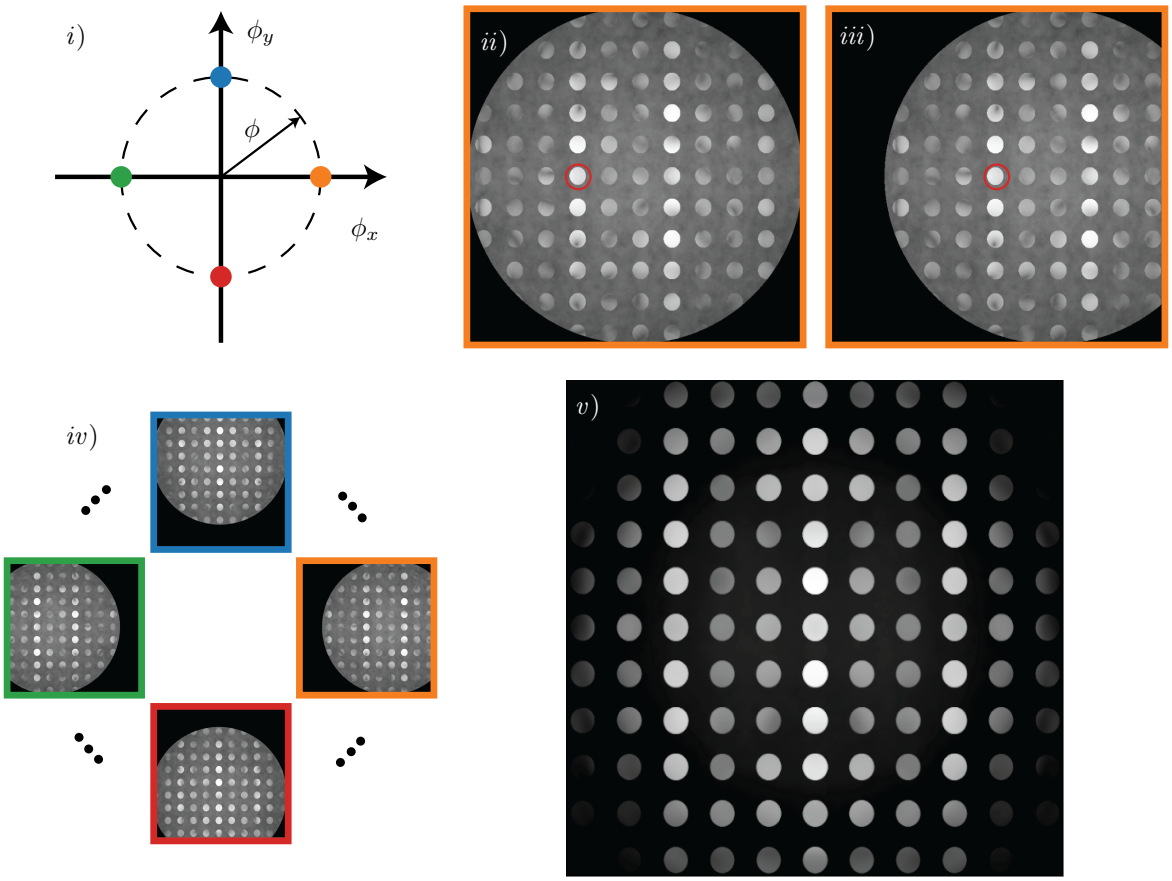


Figure 3.1: Illustration of how CBED simulations with beam tilt is used to simulate PED patterns. *i*) $N$ (here $N = 4$) points from a circle with radius $\phi$ are sampled and used as beam tilt for the CBED simulation resulting in *ii*) ($\phi = 0.5°$ was chosen for this illustration). *iii*) the simulated diffraction pattern is descanned (centered so that the zero reflection is in the center of the image). The red circle in *ii*) and *iii*) marks the zero reflection. *iv*) process in *ii*) and *iii*) is repeated for all $N$ samples of the circle in *i*), and the results are summed to get the PED simulation in *v*). For *v*), $N = 100$ was used.

## 3.5 Code

Code implementing the methods used for S(P)ED data processing and plotting, and multi-slice simulations in this thesis is made available on GitHub (https://github.com/anderscmathisen/Master_Code/tree/main).

# Chapter 4

# Results

In this chapter, the results will be presented followed by a discussion of the findings in the next chapter. This chapter is divided into five sections. The first section introduces the investigated specimen, and the second presents the crystallographic orientations of grains in the specimen found through template matching. Ferroelectric domains and domain walls are studied in the third section, and the experimental results are complemented with multislice simulations presented in the fourth section. The final section presents independent measurements to verify the results obtained with the multislice simulations.

## 4.1 Sample Overview

The polycrystalline $ErMnO_3$ FIB lamella studied in this thesis is approximately 8.5 µm by 4 µm in size, and contains around 30 grains. Figure 4.1(a) shows a bright-field TEM overview image of the entire sample. Figure 4.1(b) shows the same image as in (a), but rotated and cropped around the sample, to clearly define the coordinate system which will be used to present and discuss crystal orientations throughout this thesis. After the rotation (Figure 4.1(b)), the amorphous/nanocrystalline Pt protection layer is seen at the top of the specimen, while the attachment to the FIB half grid support is seen on the right. The $x$-axis of the coordinate system is defined as running parallel to the Pt protection layer towards the attachment to the FIB half grid.

There are a few holes in the sample, which appear as homogenous bright spots in the BF-TEM image with streaks of lighter areas beneath them. During the thinning step of specimen preparation, the ion beam mills more effectively at imperfections and holes, making holes bigger and creates streaks of thinner regions beneath them. The streaked region towards the bottom left (marked with red arrow in Figure 4.1(b)) is another FIB artifact called curtaining.

The grains in the sample can be vaguely identified from the BF-TEM image, but contrast due to other effects, such as bending and strain, is also present. Qualitatively, the lamella appears to have even thickness, which decreases slightly from top to bottom, disregarding the specimen preparation artifacts.

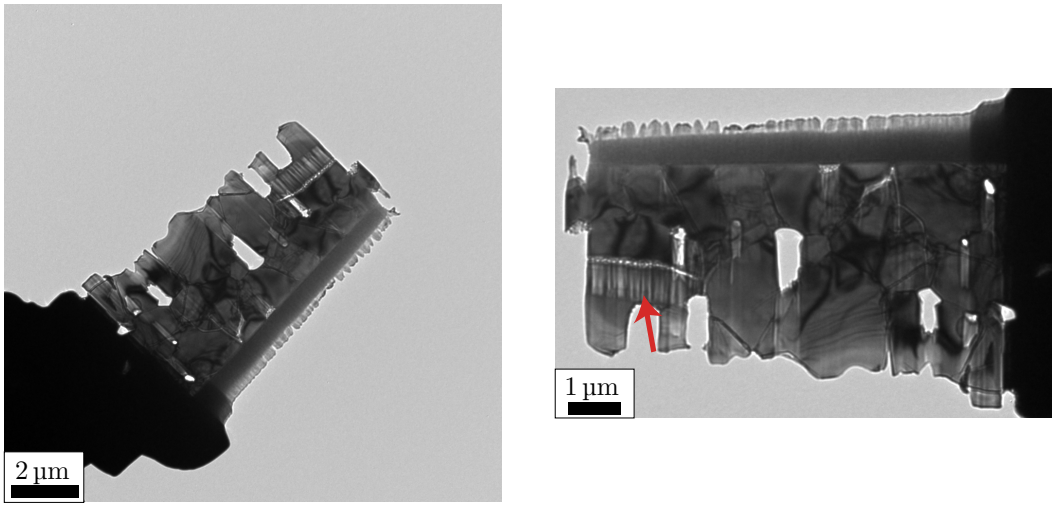


(a) (b)

Figure 4.1: BF-TEM image of the entire lamella. (a) Image as recorded on the TEM. (b) The same image as in (a), but rotated and cropped around the area of interest. The red arrow in (b) points at curtaining artifacts from the FIB sample preparation. The image was captured with the 2100 TEM.

The sample consists of a number of grains, labeled from *a*-*z* in Figure 4.2. The identification and labeling of grains are based on the BF-TEM image in Figure 4.1(b) and the result of template matching, which will be presented in section 4.2. The gray area on the top and right of the schematic sample in Figure 4.2 represent the amorphous/nanocrystalline Pt protection layer and the attachment to the sample holder. The gray grains on the left and bottom left of the sample have not been given labels as they are thinner and/or damaged from the specimen preparation and will not be considered in the rest of this thesis. Figure 4.2 also shows the coordinate system which will be used to present and discuss orientations.

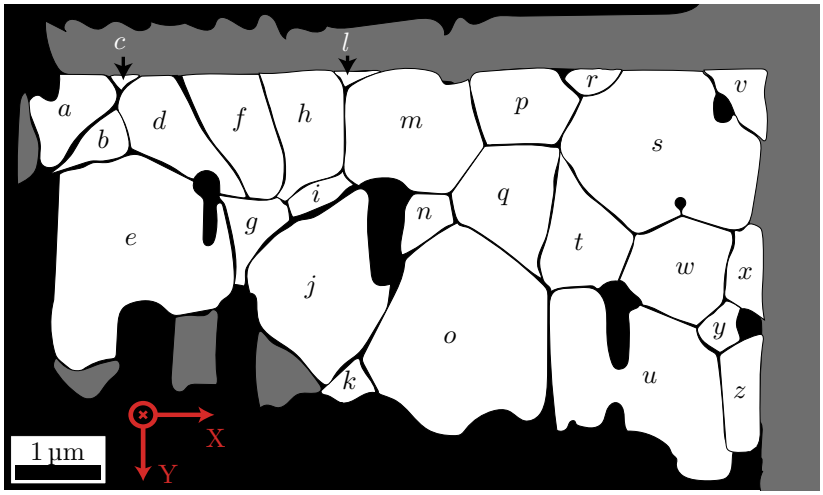


Figure 4.2: Schematic of the sample labeling 26 of the largest grains *a*-*z*. The gray areas on the top and right represent the amorphous/nanocrystalline Pt protection layer and attachment to the sample holder. The unlabeled gray grains on the left and bottom left will not be considered in this thesis because they are very thin and/or damaged from the specimen preparation. The coordinate system will be used to present and discuss orientations.

## 4.2 Crystal Orientations

To explore how the grains are orientated in space and with respect to each other, template matching of a SPED dataset of the specimen was done. Before the results of template matching are presented, the general appearance of PED patterns from different crystallographic orientations and the structure of a 4D SPED dataset will be presented.

### 4.2.1 PED Patterns and Schematic Unit Cells

Figure 4.3 shows experimental PED patterns and how these relate to crystallographic orientations. Figure 4.3(a) shows the IPF Z-projection of the three major zone axes of $ErMnO_3$: [0001] (red), $[2\bar{1}\bar{1}0]$ (green) and $[10\bar{1}0]$ (blue), as well as an orientation not close to a low index zone axis (pink). The model hexagons in Figure 4.3(a) show the unit cell corresponding to each projection in the IPF. As only the Z-projection IPF is included in Figure 4.3(a) (and neither the X- nor Y-projection), the in-plane rotations about the zone axis of the unit cells are set to correspond with the experimental PED patterns presented in Figure 4.3(b)-(e). The diffraction patterns in Figure 4.3(b)-(e) were made by summing individual PED patterns of different SPED datasets of the sample. Figure 4.3(c) and (e) are generated from the same SPED scan where (c) is the sum of PED patterns in grain $m$ and (e) from grain $f$. Figure 4.3(b) and (d) are from different SPED datasets of grain $h$ and $a$, respectively, where the grains were tilted to the desired zone axis before capturing the depicted PED patterns.

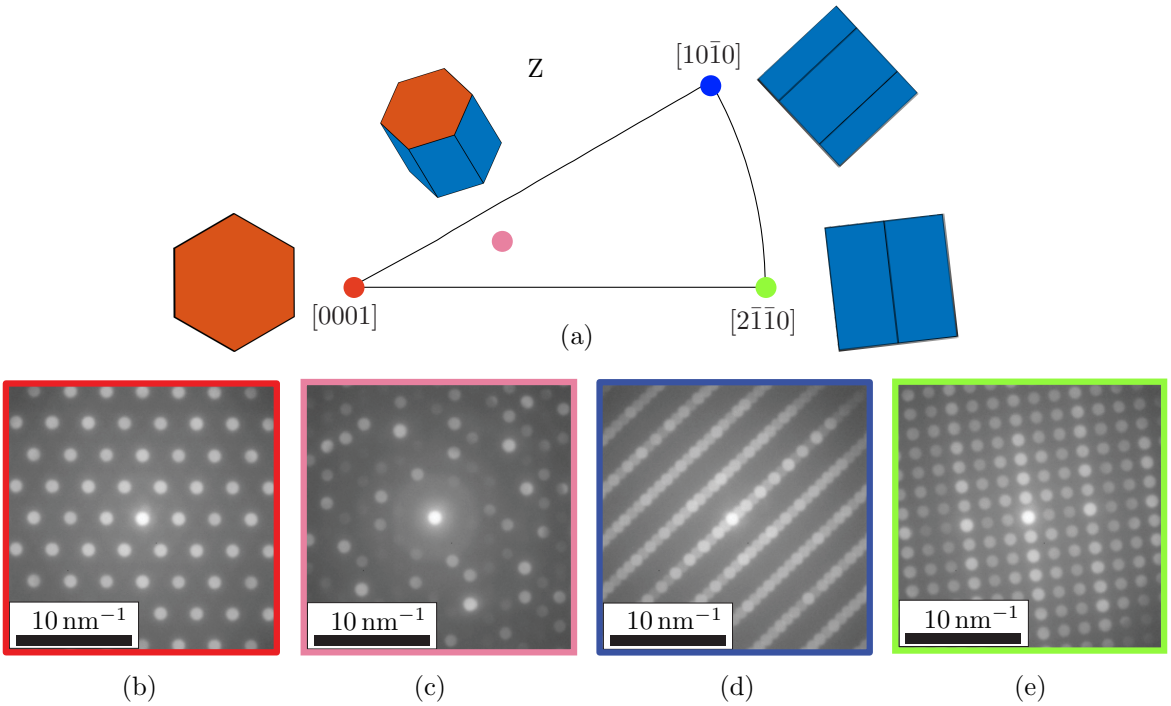


Figure 4.3: (a) The Z-projection IPF (zone axis) of the three major zone axes (red, blue and green), and an orientation not close to a low index zone axis (pink) with corresponding model unit cells. (b)-(e) Summed experimental PED patterns from the orientations plotted in (a). The colored borders in (b)-(e) correspond with the orientations in (a).

The PED patterns in Figure 4.3(b), (d) and (e) are regular and easy to recognize by characteristic ratios and symmetry. For instance, the hexagonal symmetry in Figure 4.3(b) is characteristic of the [0001] zone axis, and comparing this PED pattern to the corresponding unit cell plotted in Figure 4.3(a), the 30° rotation between real and reciprocal space for

hexagonal systems is easily recognized. Figure 4.3(d) features diffraction reflections which are very closely spaced along the $\mathbf{a}_4$ direction and are overlapping because of the convergence angle of the electron beam. Figure 4.3(e) is characteristic of $ErMnO_3$ in the $[2\bar{1}\bar{1}0]$ zone axis and will be studied in detail later. Unlike Figure 4.3(b), (d) and (e), the PED pattern in Figure 4.3(c) is not easily recognized and more representative of the PED patterns in a SPED dataset where the grain orientations are random. To determine crystal orientation from this type of PED pattern, template matching is required.

Figure 4.4(a) is a VBF image that has been generated from a SPED dataset covering the entire specimen. The 4D SPED dataset consists of individual PED patterns, such as the ones presented in Figure 4.4(b) and (c), one for each probe position in the scan. The VBF image in Figure 4.4(a) was generated from the SPED dataset by setting the pixel value of a certain probe position to the integrated intensity of the direct beam in the corresponding PED pattern. The blue and orange circles in Figure 4.4(a) show the position from which the individual (single) PED patterns in (b) and (c) were captured. Within a single grain, all PED patterns are similar, and by moving to a different grain the PED pattern changes abruptly, indicating a different crystal orientation. Compared to the PED patterns in Figure 4.3, which were summed over multiple pixels within a grain, the individual PED patterns in Figure 4.4(b) and (c) appear noisy.

In capturing the SPED dataset presented in Figure 4.4 (and all subsequent S(P)ED datasets in this thesis), a scan rotation of 19° (counterclockwise) was used to have the same specimen orientation as in Figure 4.1(b). As the pixelated detector is stationary in the TEM, the individual captured PED patterns are not affected by the scan rotation. Thus, the PED patterns in Figure 4.4(b) and (c) also need to be rotated 19° counterclockwise to align with the VBF image.

In the VBF image, the contrast arises by different orientations scattering more or less electrons away from the direct beam. Vacuum appears white (high pixel value) because in those positions, the electron beam is not scattered at all, while for example grain $d$ and $f$ appear darker because they scatter a lot of electrons, leaving less intensity in the direct beam.

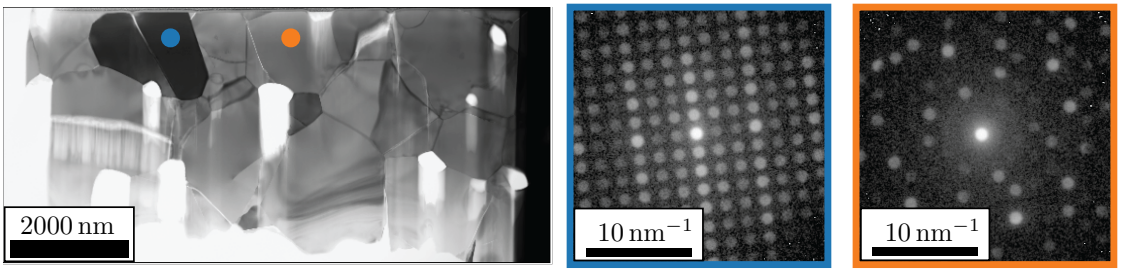


(a) (b) (c)

Figure 4.4: (a) VBF image of the entire lamella, with grain $f$ and $m$ labeled with blue and orange dots, respectively. The colored borders of (b) and (c) correspond with the dots in (a), and show the position from which these individual experimental PED patterns were captured.

### 4.2.2 Template Matching on Individual PED Patterns

Figure 4.5 shows how the crystallographic orientation of the PED patterns in Figure 4.4(b) and (c) is found though template matching. In the first step of template matching, the diffraction pattern is preprocessed, where the background is removed, intensity is rescaled, and the PED pattern is centered and blurred. The first column in Figure 4.5 shows the effect of this step. The correlation score (Equation 2.44) between the preprocessed diffraction

pattern and the simulated diffraction patterns is then calculated. The correlation scores, in the second column of Figure 4.5, have been normalized as only the relative values are of interest. The highest correlation score determines the crystal orientation. In specific applications, such as solving multiple phases, the absolute value could be of interest, but it is not relevant for this thesis.

For the diffraction pattern from grain $f$ (first row of Figure 4.5, corresponding to Figure 4.4(b)), the simulated diffraction patterns around the $[2\bar{1}\bar{1}0]$ zone axis have the highest correlation score. The correlation score of the PED pattern in Figure 4.4(c) (second row of Figure 4.5) is more even throughout the orientation space (higher after normalization), indicating that the template matching was less confident in this orientation. There is still a clear peak in the correlation score at the zone axis, as marked with the black arrow. The last column in Figure 4.5 plots the simulated best-fit diffraction pattern as red crosses on top of the experimental diffraction pattern.

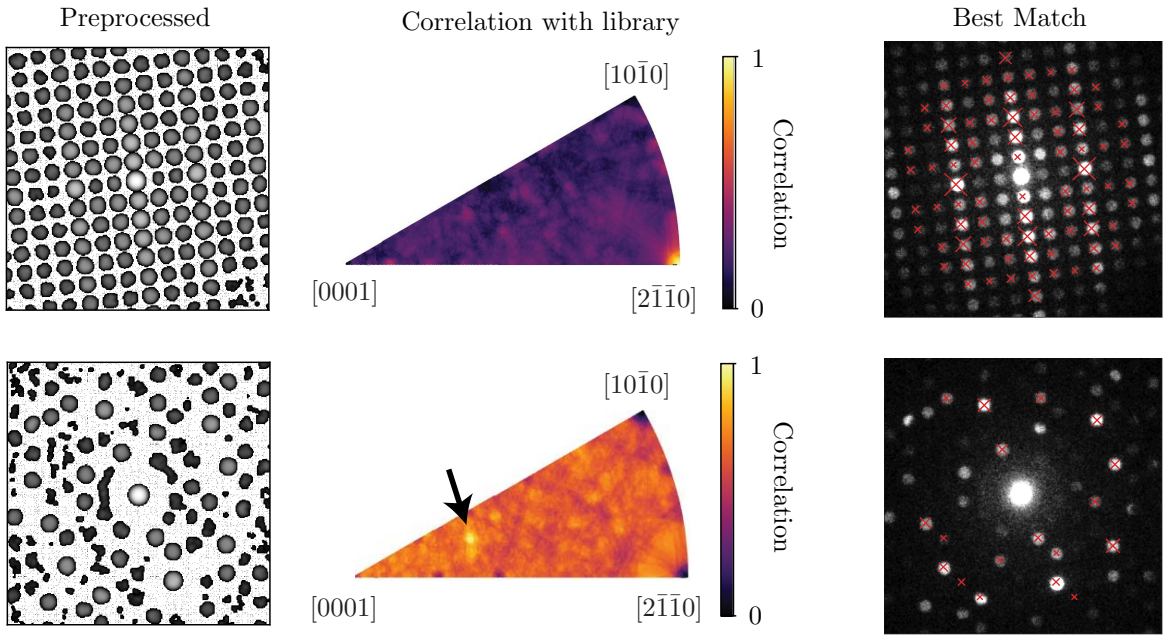


Figure 4.5: Preprocessing and template matching for the two PED patterns in Figure 4.4. The first row shows the process for Figure 4.4(b) and the second for Figure 4.4(c). The first column shows the effect of the preprocessing on the PED patterns, the second column shows the correlation score between the preprocessed PED pattern and the simulated diffraction patterns (score normalized between 0 and 1), and the last column shows the simulated diffraction pattern (the red crosses) which had the highest correlation score plotted on top of the experimental PED pattern.

### 4.2.3 Orientation of Grains in The Sample

By repeating the process shown in Figure 4.5 for all the PED patterns in the SPED dataset in Figure 4.4, comprising around 170 000 individual PED patterns, the crystallographic orientation of all the grains in the sample was found. The result is shown in Figure 4.6, with the X-, Y- and Z-projection of the orientations. The orientations found through template matching have been rotated 19° counterclockwise to correct for the scan rotation.

Although the orientation of grains in Figure 4.6 is completely specified, with the Z-projection corresponding to the zone axis and the X- and Y-projections showing the in-plane rotation, the result can be challenging to interpret. Figure 4.7 shows a different way of representing the orientations of the grains. Here, the colors are the IPF Z-projection, and

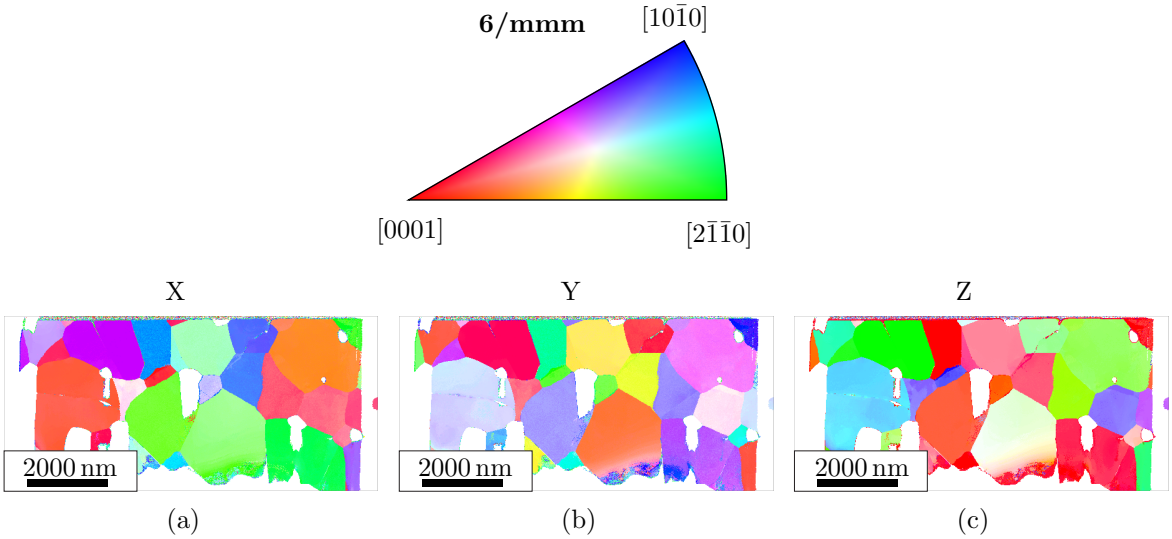


Figure 4.6: The orientation of the grains in the sample found by template matching on SPED data. (a), (b) and (c) show the X-, Y- and Z-projection of the orientation. The IPF color space is provided on top.

in addition unit cells are plotted on top of each grain. In this figure, one can easily examine the crystallographic orientation of all the grains.

Based on the uniformity of colors within grains, template matching appears to have been successful. There are, however, a few artifacts towards the bottom of the sample, where it is thin and damaged. This is especially prominent at the bottom of grain $o$ where the color becomes red while the rest of the grain is beige. The same red color is also seen around the edges of the holes in the specimen. Some red lines are also seen in and between certain grains, such as through grain $p$ and between grain $d$ and $f$.


Figure 4.7: Crystallographic orientation of grains in the sample with unit cells plotted on top of each grain.

Two unit cells have been placed on grain $n$ in Figure 4.7, which is likely caused by a pseudosymmetry. A pseudosymmetry is not an actual symmetry of the crystal structure, but rather two different (non-equivalent) crystallographic orientations that give similar diffraction patterns. Thus, in the template matching, there are two different orientations which both correlate reasonably well with the experimental diffraction patterns. In the pixels of grain $n$, the found orientation will therefore randomly be either of the two. This is why the

MTEX software, which reconstructs grains and plots the unit cells, wrongly reconstructs two grains inside of grain $n$, explaining the placement of the two unit cells.

To figure out which of the two unit cells plotted on top of grain $n$ in Figure 4.7 is the correct, one could try to optimize the parameters of preprocessing and template matching. However, the easiest solution is to slightly reorient the sample using the double tilt sample holder, and scan the sample again. This will move the orientation of grain $n$ away from the difficult orientation with a pseudosymmetry, and hopefully only a single solution will be found in template matching on the new SPED dataset.

This is the case even for a slight holder tilt adjustment, as shown in Figure 4.8. Figure 4.8(a) was captured at around the same sample tilt as Figure 4.7 (3.2°, 2.4°), while Figure 4.8(b) was captured with an $x$-tilt of 0.8° and a $y$-tilt of −2.0°. Grain $n$ in Figure 4.8(a) again features two unit cells. In Figure 4.8(b), however, grain $n$ only has a single unit cell, showing that it was the lower unit cell of grain $n$ in Figure 4.7 which was correct. Grain $q$ in Figure 4.8(b) now has the same problem which grain $n$ has in Figure 4.8(a) and Figure 4.7, however the orientation of this grain was unambiguously determined in Figure 4.7.

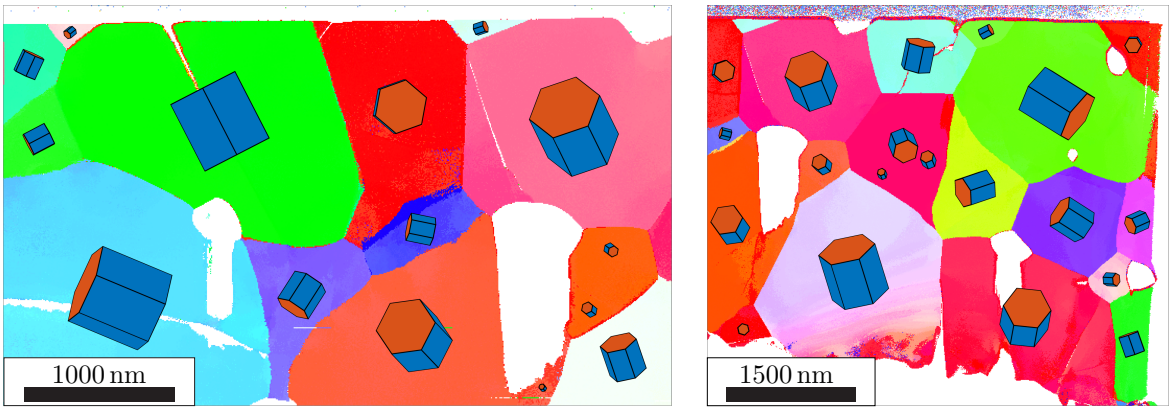


(a) (b)

Figure 4.8: The result of template matching on two SPED datasets captured at slightly different sample tilt. (a) was captured with an $x$- and $y$-tilt of 3.2° and 2.4°, while (b) was captured with an $x$- and $y$-tilt of 0.8° and −2.0°. Grain $n$ in (a) features two unit cells indicating that this orientation has a pseudosymmetry. After tilting the specimen in (b), the pseudosymmetry is broken and the orientation of grain $n$ is readily solved.

Knowing the 3D crystallographic orientation of all the grains in the sample, several aspects can be deduced. For example, the misoreintation angle between orientations at the grain boundaries can be calculated from Equation 2.22. This is plotted in Figure 4.9(a), where the misorientation angles are drawn manually on top of a VBF image. A further example of a deduction one can do after template matching is calculating the angle between the $c$-axis at the grain boundaries. This can be done by expressing the $c$-axes as Cartesian vectors in the sample coordinate system, and calculating the angle between two vectors at grain boundaries. The result is shown in Figure 4.9(b), where the angles have been drawn manually on top of a VBF image of the sample. Although the angles in Figure 4.9(a) and (b) are similar, they are not the same. For instance, two orientations that are related to each other by a rotation, $\theta$ about the $c$-axis will have a $c$-axis angle of 0°, but the misorientation angle will be $\theta$.

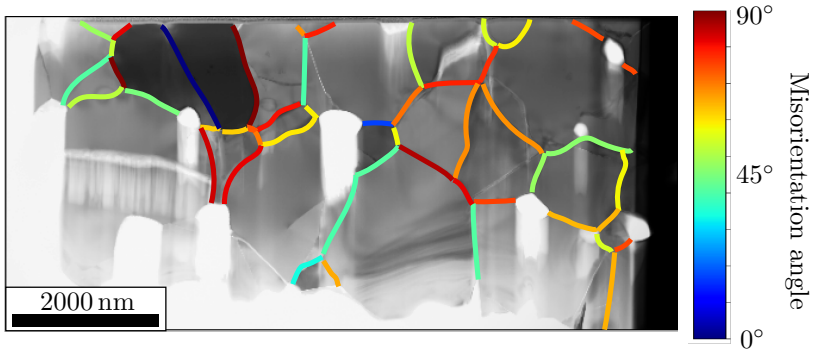


(a)

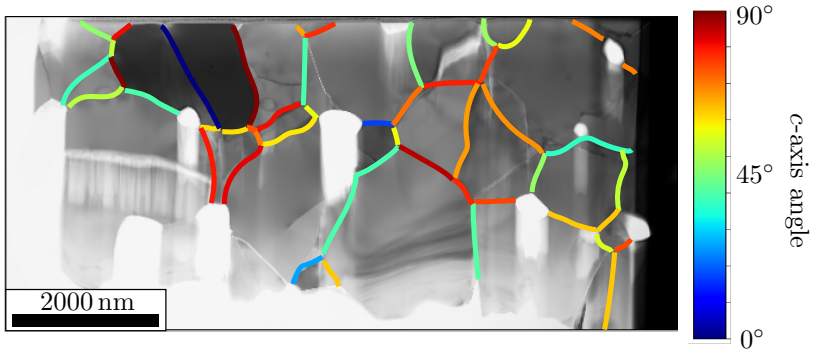


(b)

Figure 4.9: (a) The misorientation angle between the orientations at the grain boundaries. (b) The angle between the $c$-axes at the grain boundaries. In both plots, the angles were calculated using Orix from mean grain orientations found with MTEX, and drawn manually on top of the VBF image in Figure 4.4.

The angle of the crystallographic $c$-axis to the imaging plane (the plane perpendicular to the electron beam) is also calculated from the template matching orientations maps, and is plotted in Figure 4.10. This angle describes how much the $c$-axis points in the imaging plane, so that the [0001] zone axis has an angle of 90°, and the $[2\bar{1}\bar{1}0]$ and $[10\bar{1}0]$ zone axes both have an angle of 0°.

The $c$-axis angles at grain boundaries and angle between $c$-axis and imaging plane calculated from orientation maps are related to the ferroelectric aspects of this study. The angle between the $c$-axes at grain boundaries is related to the charging at grain boundaries though Equation 2.45. The angle between the $c$-axis and the imaging plane is related to measuring polarization and visualizing ferroelectric domains within a grain for a given orientation (more on this in subsection 4.3.2).

### 4.2.4 Template Matching Orientation Accuracy

The crystal orientations found through template matching on SPED have a certain error range. The aim now is to quantify this error range though a tilt series. In Appendix B, 14 SPED datasets with $x$-tilt ranging from -30.7° to 30.2°, and 5 SPED datasets with $y$-tilt ranging from -18.2° to 17.5° were used to determine the position of the gonio system tilt axes as a function of scan rotation. These 18 datasets (the two tilt series shared one common

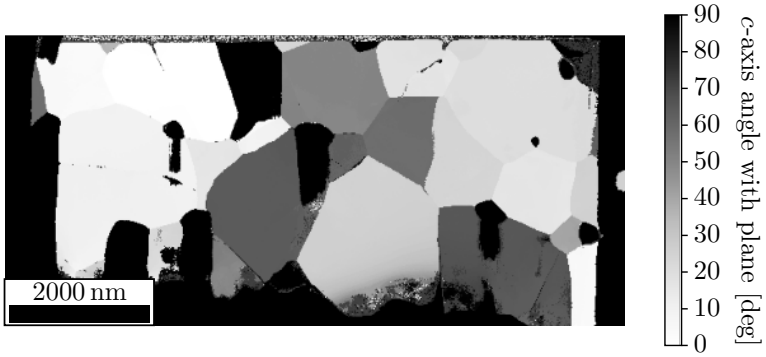


Figure 4.10: The angle between the $c$-axis and the imaging plane (the plane perpendicular to the electron beam).

sample tilt) as a combined set can be used to estimate the accuracy of template matching.

The 18 SPED datasets in the tilt series covered the five grains $f$, $g$, $h$, $i$ and $j$. In Figure 4.11, the results of template matching on three of the datasets in the $x$-tilt series are presented to qualitatively illustrate an error in template matching. Grain $h$ appears to be in the [0001] zone axis in both Figure 4.11(b) and (c). This suggests that the template matching for this grain has failed as (b) and (c) were captured at completely different sample tilts, and the difference in sample tilt should be reflected in the determined orientations.

A quantitative measure for the accuracy of template matching is found by calculating the mean orientation of the five grains in all the datasets, and converting those orientations back to a reference sample tilt through Equation 2.25 based on the $x$- and $y$-tilts at which the datasets were captured. If the template matching was errorless (and the goniometer of the double tilt holder was flawless), the orientation of each grain from each step in the tilt series after the transformation would be identical. In reality, however, there will be a spread in the transformed orientations, and this orientation spread will give an indication of the template matching orientation accuracy. Equation 2.25 requires the angle of rotation between the scan directions and the tilt axes ($\theta$) as a parameter. In Appendix B this angle was determined to be 9.6° for the 19° scan rotation that was used for the tilt series.

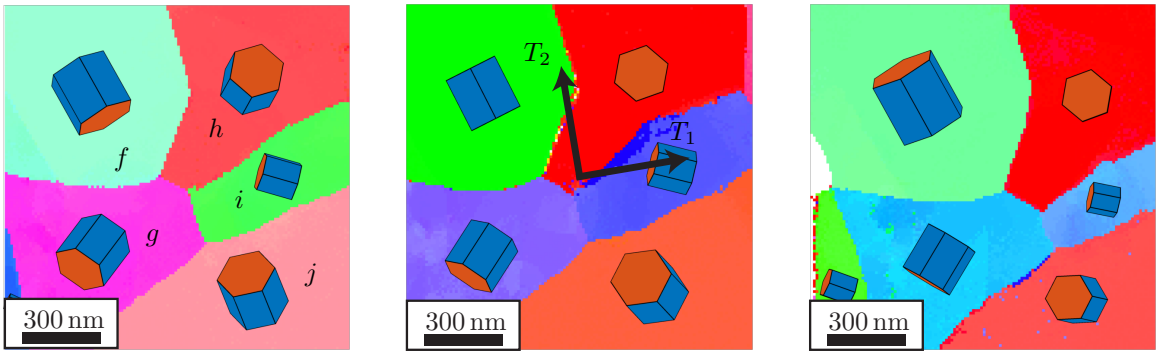


(a) (b) (c)

Figure 4.11: The result of template matching on three of the datasets in the SPED tilt series covering grain $f$, $g$, $h$, $i$ and $j$. The $x$- and $y$-tilts were (a): (-17.5°, 1.8°), (b): (2.5°, 1.8°), and (c): (18.0°, 1.8°). In (b) the tilt axes found through the analysis in Appendix B are plotted on top of the image.

The resulting orientations after the transformation back to the reference $x$- and $y$-tilt (0°, 0°) are presented in Figure 4.12 as an IPF with X-, Y- and Z-projections. In order

to quantify the spread in orientation space for each of the grains, a mean orientation is calculated. Subsequently, the misorientation between each of the transformed orientations to the mean orientation is calculated. The average misorientation angle describes the spread in orientation space. From Figure 4.12 it is clear that template matching has worked well for grain $f$, $g$, $j$ and $i$, where the average misorientation angle is around 0.5-0.6°. For grain $h$, however, the average misorientation angle is 5.26°. This quantifies what is seen in Figure 4.11, namely that template matching on grain $h$ did not work well. It appears that the zone axis [0001] is preferred by the template matching algorithm, and that it is sometimes chosen even when it is not the actual zone axis.

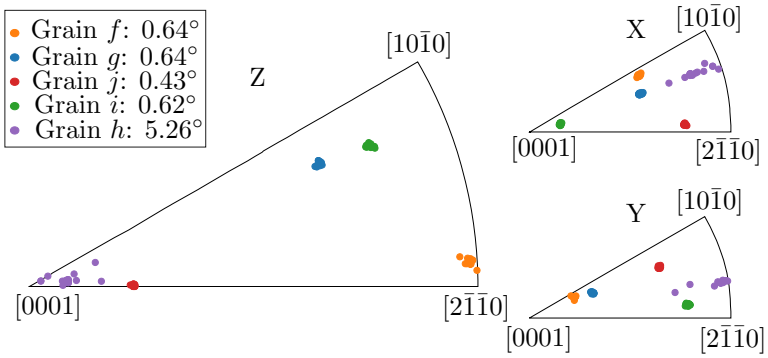


Figure 4.12: IPF showing the orientation of the 5 grains in the tilt series of 18 tilts after transforming the orientation found through template matching back to the reference sample tilt (0°, 0°) through Equation 2.25. The numbers in the legend are the average misorientation angle to the mean orientation for each grain.

### 4.2.5 Finding Sample Tilts for Target Zone Axes

The procedure for tilting the sample to specific zone axes in a polycrystalline material can be time-consuming. This process usually involves examining kikuchi lines and SAD patterns while searching for the desired zone axis by tilting the sample and applying a high electron dose to a small volume. The process can be especially tedious for polycrystals with small grains as $x$-tilt and $y$-tilt can (for most TEM sample holders) not simultaneously be at eutectic height, so the act of tilting the sample also moves the area that is probed with the electron beam. In addition, for crystals with large symmetry reduced orientation regions such as $ErMnO_3$, the desired zone axis will often lie outside the maximum tilt range, leaving the search futile. Knowing the 3D crystallographic orientation of all the grains in the sample through template matching, the position of both gonio tilt axes relative to the specimen reference frame, and being able to describe the transformation to other sample tilts through Equation 2.25, the procedure of orienting to specific zone axes can be made semi-automatic.

Finding zone axes is made semi-automatic by searching for values of $x$ and $y$ in Equation 2.25 (the $x$- and $y$-tilt of the double tilt holder) so that the desired zone axis in the transformed orientation is parallel to the optical axis of the TEM. In the search for $x$ and $y$, all symmetrically equivalent zone axes to the desired one need to be considered, as well as the maximum tilt range of the double tilt holder. This problem may have an analytical solution, however, when implementing this in code, it is much easier to search for the values of $x$ and $y$ that minimize the angle between the desired zone axis (or a symmetrically equivalent one) and the TEM optical axis through SciPy's `minimize` function [51] under the restriction that the $x$- and $y$-tilt are within the bounds ±30°.

To evaluate how well this approach finds the $x$- and $y$-tilts for different zone axes, 9 zone axes for different grains were chosen arbitrarily, and the $x$- and $y$-tilt of the actual zone

axis were found experimentally. The SAD patterns from these 9 zone axes are shown in Appendix A (Figure A.2), and the results are compared with the predicted $x$- and $y$-tilts in Table 4.1. The deviation (Euclidean distance, $\sqrt{(x-x')^2+(y-y')^2}$) between the software predicted $x$- and $y$-tilt and the actual $x$- and $y$-tilt for all 9 zone axes is given in Table 4.1. The average deviation is $0.73 \pm 0.38°$.

Table 4.1: Software prediction and actual values for the sample tilt for zone axes of different grains. The SAD patterns from these zone axes are presented in Appendix A (Figure A.2). The deviation between the software prediction and the actual value is calculated as the Euclidean distance.

| Grain | Wanted Zone axis | Software Prediction | Actual Sample tilt | Deviation |
|---|---|---|---|---|
| $w$ | $[10\bar{1}0]$ | (-9.1, 15.4) | (-9.6, 16.4) | 1.12 |
| $s$ | $[2\bar{1}\bar{1}0]$ | (6.0, -18.6) | (6.5, -17.9) | 0.86 |
| $s$ | $[4\bar{2}\bar{2}1]$ | (-0.2, -2.5) | (-0.2, -2.0) | 0.5 |
| $s$ | $[2\bar{1}\bar{1}1]$ | (-5.5, 11.2) | (-5.7, 11.7) | 0.54 |
| $t$ | $[8\bar{4}\bar{4}9]$ | (-11.6, -24.1) | (-11.9, -24.4) | 0.42 |
| $p$ | $[2\bar{1}\bar{1}0]$ | (-14.5, 11.7) | (-14.2, 10.3) | 1.43 |
| $n$ | $[0001]$ | (16.1, -24.8) | (17.0, -24.6) | 0.92 |
| $f$ | $[4\bar{2}\bar{2}1]$ | (-10.5, 13.1) | (-11.1, 12.7) | 0.72 |
| $m$ | $[10\bar{1}1]$ | (-3.7, -2.4) | (-3.7, -2.3) | 0.1 |
| Average | N/A | N/A | N/A | $0.73 \pm 0.38$ |

## 4.3 Visualization of Ferroelectric Domains

So far, it has been shown that the crystallographic orientation of grains can be found through template matching on SPED data, and that this can be used to deduce for instance misorientation angles, or tilting grains to a desired zone axis. However, the orientation found so far have been in the 6/mmm Laue group symmetry, while the actual point group of $ErMnO_3$ is 6mm. In template matching, this reduction of orientation space is by design as the kinematic approximation used for template matching is unable to resolve the non-centrosymmetric 6mm point group.

The extra mirror plane perpendicular to the $c$-axis in 6/mmm (compared to 6mm) essentially describes that the ferroelectric polarization direction has not been found with template matching. That is, the 6/mmm point group is centrosymmetric and there is no difference to whether the $c$-axis points up or down in the hexagonal unit cell. The aim now is to resolve the non-centrosymmetric nature of $ErMnO_3$ and find the polarization direction, thereby extending the orientation mapping of grain orientations to domain orientation mapping.

### 4.3.1 Bright-Field Domain Structure Imaging

In Figure 4.13, three BF-TEM images of grain $f$ on the $[2\bar{1}\bar{1}0]$ zone axis are shown. In each of the BF-TEM images, the domain wall between two ferroelectric domains is visible as a faint dark line (highlighted by the red arrows). In capturing these images, conventional (non-scanning) TEM was used to control the size and position of the electron beam manually. Between capturing each of the images in Figure 4.13, the electron beam was focused close to the domain wall, moving the domain wall towards the electron beam in the $c$-direction. Between Figure 4.13(a) and Figure 4.13(b), the electron beam was focused below and along the domain wall, which moved it down, and between Figure 4.13(b) and Figure 4.13(c), the

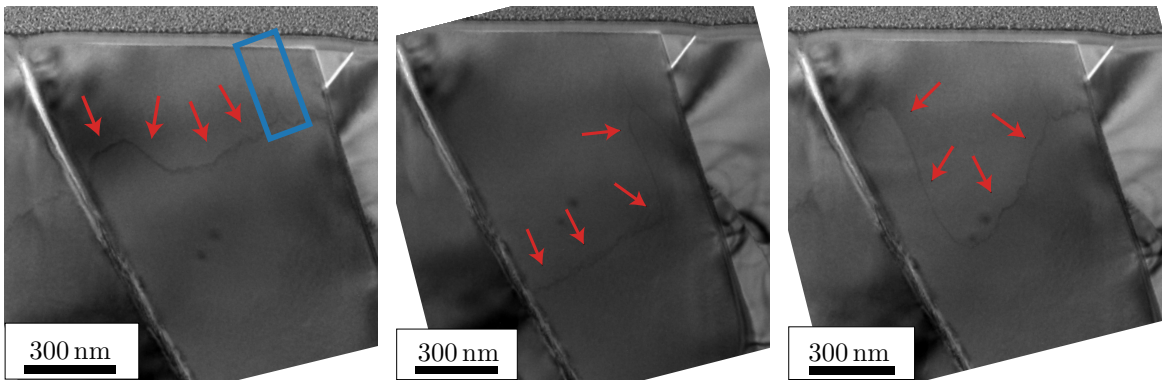


(a) (b) (c)

Figure 4.13: BF-TEM images of domain walls under the influence of the electron beam. The domain wall appears in these images as a faint dark line (indicated by the red arrows). Between capturing (a) and (b), the electron beam was focused below the domain wall, moving it down. Between capturing (b) and (c), the electron beam was focused above the domain wall on the left part of the grain, moving the domain wall here back up. The blue rectangle in (a) highlights a pinned domain wall that resisted movement by the electron beam. The white region in the corner of the images is caused by the rotation and crop performed to orient the sample similar to the other images used in this thesis.

electron beam was focused above the domain wall on the left part of the grain, moving only the left part of the domain wall back up again.

Although the domain walls in general are mobile and influenced by the electron beam, some domain walls appear more stable. In the upper right part of grain $f$ in Figure 4.13 (marked with blue rectangle in Figure 4.13(a)), two domain walls merge together into a thin line, running all the way up to the amorphous Pt layer. This thin line appears to be a pinned domain wall, and resisted movement by the electron beam. A HRTEM image of this region is shown in Figure 4.14. Unlike the other images of the specimen in this report, Figure 4.14 has not been rotated, and so the position of the amorphous Pt protection layer is to the right (outside the depicted area). This stable pinned domain wall will serve as a reference point for the further studies of the domains in grain $f$.

### 4.3.2 Virtual Dark-Field Imaging

Although BF-TEM images can show the position of domain walls, they do not convey any information about the polarization direction on either side of the domain wall. In the project report preceding this thesis [15], it was shown that VDF images generated from SPED datasets could be used to visualize ferroelectric domains. It was found that for many crystal orientations, not just the $[2\bar{1}\bar{1}0]$ zone axis, which is commonly used to image domain walls with high resolution HAADF-STEM, there is a difference in the intensity of certain diffraction reflections, depending on the polarization direction. In VDF images generated from those particular reflections there will therefore be a contrast difference between domains.

VDF images of grain $f$, with ferroelectric domain contrast, are shown in Figure 4.15, where (a) is a VDF image from a SED dataset, and (b) is a VDF image from a $\phi = 1°$ SPED dataset. In both (a) and (b), the insert is a summed (P)ED pattern from a region within grain $f$. The summed (P)ED patterns are plotted on a logarithmic scale. By comparing the two, it is clear that precession increases the intensity further out in reciprocal space. The red circle in the insert marks the diffraction reflection used to generate the VDF image. The $(00\bar{2})$ reflection was used for the SED VDF image in Figure 4.15(a), and the $(0\bar{1}12)$ reflection for the SPED VDF image in Figure 4.15(b). Although the SED VDF image features ferroelectric

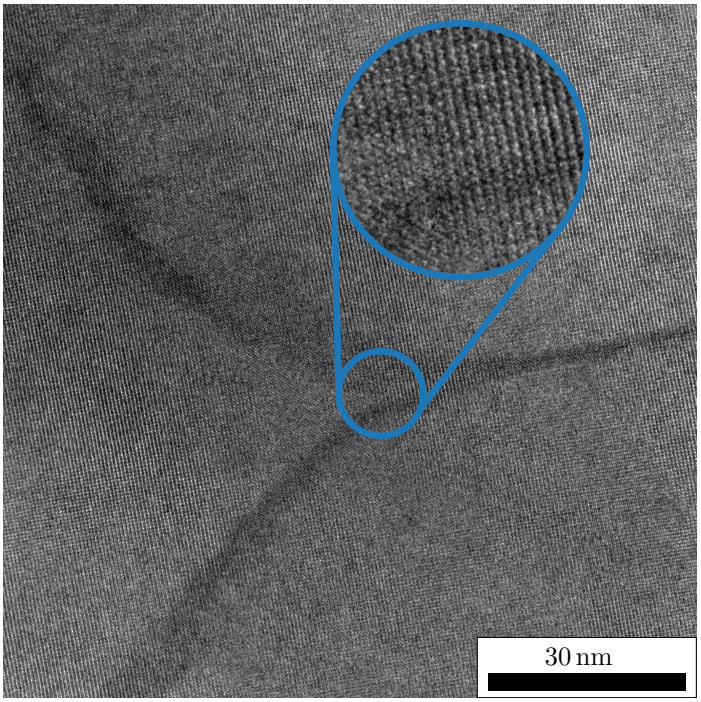


Figure 4.14: HRTEM image of the region in grain $f$ where two domain walls merge to a thin line. The insert is a digital zoom of the same image. Note that this image is presented as captured in the TEM, and so the amorphous Pt protection layer is located to the right.

domain contrast, the intensity within the domains varies, which is likely due to thickness variations and local strain fields. The same uneven intensities within domains are also observed in conventional DF-TEM images, which is presented in Appendix A (Figure A.3). Precessing the beam tends to average out thickness and strain effects, resulting in more even intensity within domains, as seen in Figure 4.15(b).

Note that the ferroelectric domain contrast is inverted between Friedel pairs. That is, if the VDF image in Figure 4.15(b) had been generated from $(01\bar{1}2)$ (inverted through the direct beam) instead of $(0\bar{1}12)$, the bright domain would become dark, and the dark domain would become bright. This is illustrated in Appendix A (Figure A.4), and was also extensively explored in the project report preceding this thesis [15].

As mentioned, ferroelectric domain contrast is observed for a range of different orientations, even when the $c$-axis is not pointing in the imaging plane or the grain is in a low index zone axis. Figure 4.16 shows a composite VDF image generated from the SPED dataset in Figure 4.4. As the PED for each grain is different, a VDF image has been generated by manual trial-and-error selection of reflections for each grain separately, and stitched together to form the composite VDF image. Because the VDF images are generated for each grain separately, contrast between different grains can not be compared, only within a grain is the contrast comparable.

In some grains, no domain contrast could be found. These grains are marked with the red stars in Figure 4.16, and have been artificially darkened to avoid distracting from the grains with domain contrast. For the grains with no ferroelectric domain contrast, there are three possibilities: i) the grain only has a single ferroelectric domain. ii) The polarization direction ($c$-axis, see Figure 4.10) is too parallel to the electron beam thus not influencing the intensities in the diffraction pattern. iii) The ferroelectric domain contrast is too weak to be observed.

In the grains with notable domain contrast, the domain walls are marked with red lines in Figure 4.16. The domain contrast in some grains, like $a$, $f$, $j$ and $m$, is very prominent, while for others, like $o$ and $u$, other types of contrast also contribute considerably. The other types of contrast appear as more slowly varying intensity differences (compared to the ferroelectric domain contrast), and is believed to be caused mainly by grain bending.

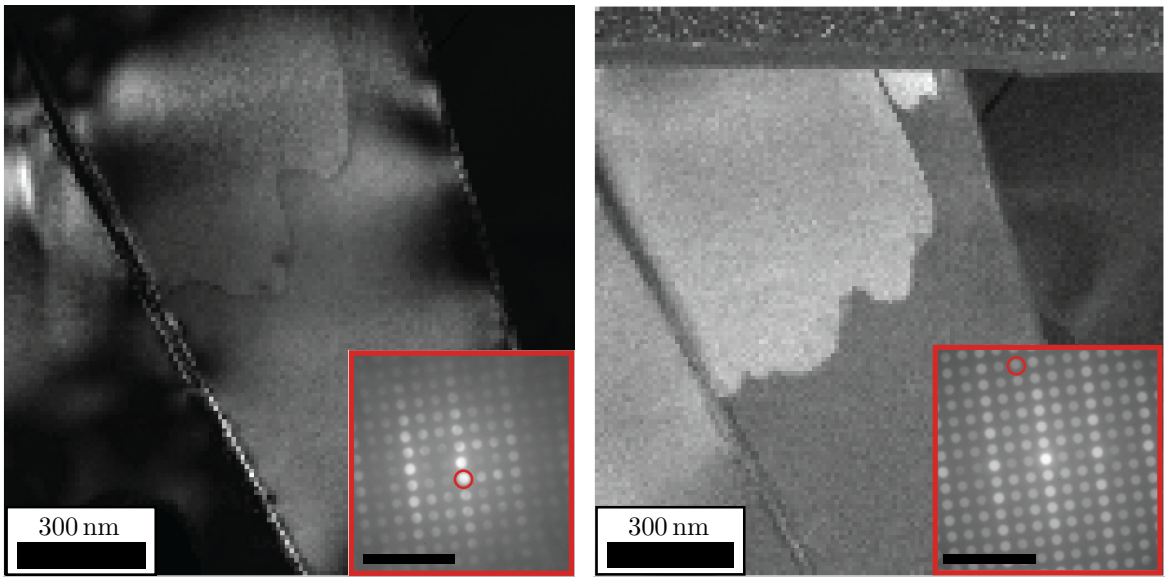


(a) (b)

Figure 4.15: (a) VDF image generated from a SED dataset of grain $f$. (b) VDF image generated from a SPED dataset of the same grain with a 1° precession angle. Both datasets were captured with grain $f$ on the $[2\bar{1}\bar{1}0]$ zone axis. The insert in (a) and (b) shows a summed (P)ED pattern from grain $f$, and the red circle marks which reflection was used to generate the VDF image. The scale bar in the insert is $10\,\mathrm{nm}^{-1}$ in both (a) and (b).

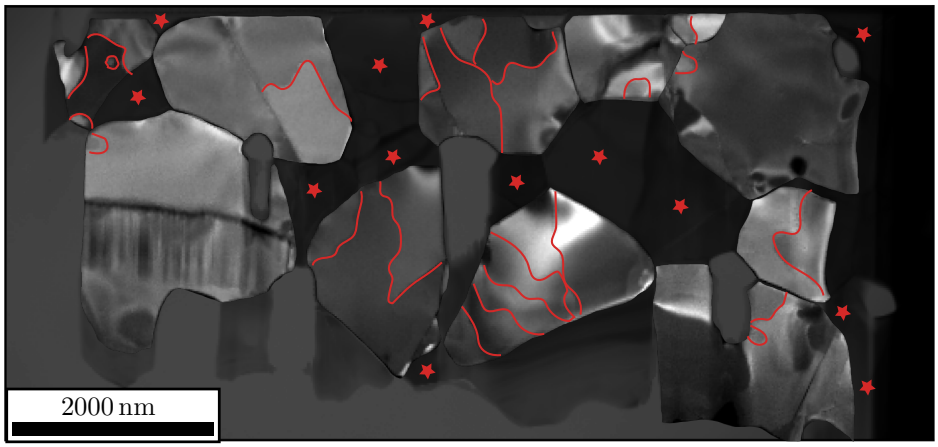


Figure 4.16: Composite VDF image generated from a SPED dataset of the sample showing domain contrast in many grains. VDF images were generated separately for each grain, and stitched together to form an image where the ferroelectric domains are visible in many grains. Domain walls are marked with red lines. No domain contrast was found in the artificially darkened grains marked with red stars.

To get an impression of which crystallographic orientations give ferroelectric domain contrast, a series of SPED scans with increasing angle between the $c$-axis and the imaging plane were captured, starting at the $[2\bar{1}\bar{1}0]$ zone axis ($c$-axis fully in-plane) and ending at the [0001] zone axis ($c$-axis fully out-of-plane) by tiling around the $[01\bar{1}0]$ crystal direction. This was done using Equation 2.25 and the procedure described in subsection 4.2.5, and would be extremely tedious without this aid. From this series, VDF images were generated and the ferroelectric domain contrast was investigated.

The chosen orientations were all zone axes on the form $[2j, \bar{j}, \bar{j}, i]$, e.g. zone axes along the line between $[2\bar{1}\bar{1}0]$ and [0001] in the stereographic projection. Because there is a 90° angle between these two zone axes, and the double tilt holder has a maximum tilt range of ±30°, no single grain could be used for the entire series. Instead, multiple grains were used so that the entire range could be covered. The sampled zone axes and the grains that were used for those zone axes are summarized in Table 4.2.

For each of the total 9 SPED datasets, the diffraction pattern will contain a multitude of diffraction reflections, depending on which crystallographic planes meet the diffraction condition. VDF images can be generated from any of the diffraction reflections, but generally only some reflections results in a VDF image with ferroelectric domain contrast. And some reflections will give better contrast than others.

VDF images were generated from all diffraction reflections in the 9 SPED datasets, and the further analysis was performed on the VDF images where ferroelectric domain contrast was observed manually. This initial manual selection was done to exclude VDF images with strong bending contrast, which was not of interest. The contrast between the ferroelectric domains was calculated from Equation 2.42, using the average intensity of a region in the bright domain $I_H$, as well as the average intensity of the darker domain $I_L$.

Figure 4.17 shows the ferroelectric domain contrast values (Equation 2.42) from all the VDF images generated from the SPED datasets with increasing angle between the $c$-axis and the imaging plane. The contrast generally decreases as the angle increases, and for angles above the 72.2° (the $[2\bar{1}\bar{1}5]$ zone axis), no domain contrast was found for any of the diffraction reflections. $N$ in Table 4.2 is the number of data points for each angle in Figure 4.17, and also generally decreases for increasing angles.

The diffraction reflections that resulted in VDF images with ferroelectric domain contrast, and the VDF images with the highest contrast are all shown for the different zone axes in Appendix A (section A.5, Figure A.5-A.13).

Table 4.2: The zone axes used to investigate how ferroelectric domain contrast in VDF images from SPED datasets varies as the angle between the $c$-axis and the imaging plane changes. $N$ is the number of diffraction reflections which resulted in ferroelectric domain contrast in the VDF image.

| Grain | Zone axis | $c$-axis angle with imaging plane | $N$ |
|---|---|---|---|
| $f$ | $[2\bar{1}\bar{1}0]$ | 0° | 82 |
| | $[4\bar{2}\bar{2}1]$ | 17.3° | 26 |
| $m$ | $[4\bar{2}\bar{2}3]$ | 43.0° | 55 |
| | $[4\bar{2}\bar{2}5]$ | 57.3° | 5 |
| | $[2\bar{1}\bar{1}3]$ | 61.8° | 16 |
| | $[2\bar{1}\bar{1}5]$ | 72.2° | 10 |
| | $[2\bar{1}\bar{1}6]$ | 75.0° | 0 |
| $j$ | $[2\bar{1}\bar{1}10]$ | 80.9° | 0 |
| $d$ | [0001] | 90° | 0 |

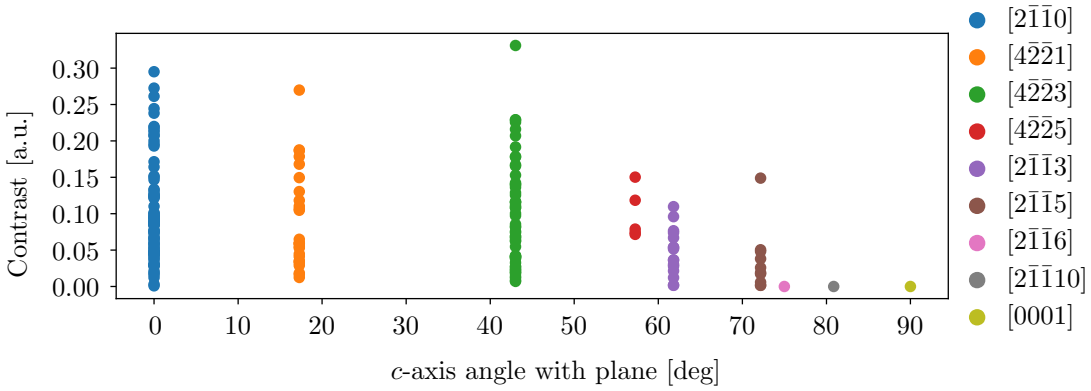


Figure 4.17: Ferroelectric domain contrast (Equation 2.42) in VDF images generated from SPED dataset of different zone axes. Each color represents a different zone axis, and each point of that color represents the ferroelectric domain contrast in a VDF image generated from different diffraction reflections.

## 4.4 CBED and PED Simulations

By using VDF images based on SPED data, the grain orientation map may be expanded to a domain map. However, the VDF images only show that the domains are oppositely polarized. To determine which domain has what polarization direction, the intensity of Friedel pairs can be compared with dynamically simulated intensities.

Figure 4.18 shows the result of the CBED and PED multislice simulations of $ErMnO_3$ in the [2$\bar{1}\bar{1}$0] zone axis with the $c$-axis (the polarization direction) pointing vertically up for (a) $\phi = 0°$ (CBED), (b) $\phi = 0.5°$ (PED), and (c) $\phi = 1°$ (PED). The parameters for these simulations are listed in Table 3.1. The diffraction patterns shown in Figure 4.18 were all simulated with a thickness of around 71 nm, but the full simulations consist of 300 diffraction patterns with equidistant thicknesses between 25 nm and 150 nm. The diffraction patterns in Figure 4.18 are all plotted on a logarithmic scale with a small constant offset to avoid issues with the logarithm of 0. Figure 4.18(a) and Figure 4.18(b) show the full field of view of the simulation, while Figure 4.18(c) has been cropped to have the same field of view as (a) and (b). The uncropped version of Figure 4.18(c) is given in Appendix A (Figure A.14).

The CBED simulation in Figure 4.18(a) took about 30 min on a standard laptop (Apple MacBook Pro 16" 2019, 6 cores, 16 Gb RAM), while the $\phi = 0.5°$ and $\phi = 1°$ PED simulations were done on a workstation computer (Custom built, 256 Gb RAM, AMD Ryzen Threadripper 64 core processor) and took 4 h, and 26 h, respectively. For these simulations, the $N = 100$ different beam tilts were computed sequentially on all available cores of the CPU.

Comparing Figure 4.18(a) to (b) and (c), it is clear that in the simulation, the precession (sampling different beam tilts) has a similar effect to precession in experimental SPED. In the CBED simulation (Figure 4.18(a)) there are larger intensity variations within the diffraction discs compared to the PED simulations (Figure 4.18(b) and (c)). Additionally, the simulated PED patterns have more intensity further out in reciprocal space compared to the CBED simulation. Comparing the $\phi = 0.5°$ and $\phi = 1°$ simulations, the $\phi = 0.5°$ simulation appears to have greater intensity between the diffraction discs, however, when plotting the full field of view of the 1° PED simulation (in Appendix A, Figure A.14) it is clear that this is not really the case, and just an artifact from normalization. Although the intensity between diffraction disks are similar, the relative intensities of the diffraction discs are different between the two PED simulations.

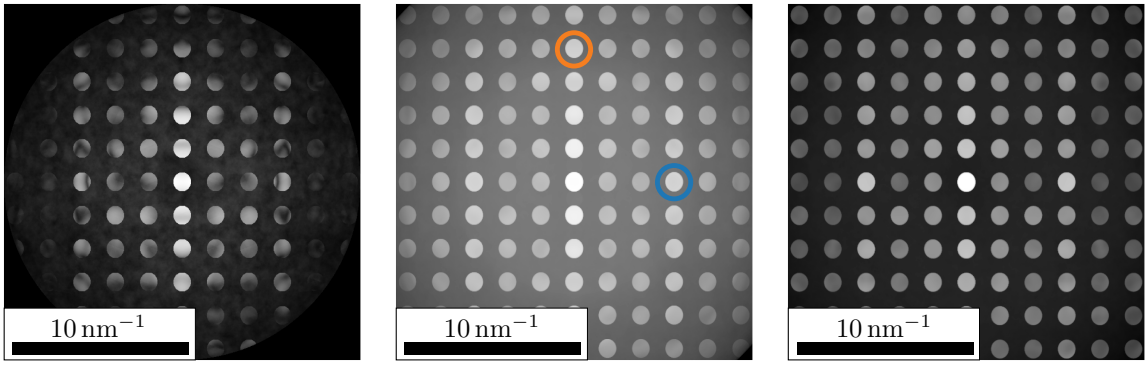


(a) (b) (c)

Figure 4.18: (a) CBED ($\phi = 0°$), (b) PED ($\phi = 0.5°$), and (c) PED ($\phi = 1°$) simulations of $ErMnO_3$ in the $[2\bar{1}\bar{1}0]$ zone axis. In these simulations, the $c$-axis points vertically up, so in (b) the orange circle marks the (008) diffraction reflection, and the blue circle marks the (030) diffraction reflection (indexing is the same in (a) and (c)). These images are plotted on a logarithmic scale with a small constant offset. The $\phi = 1°$ simulation (c) has been cropped to the same field of view as (a) and (b). The uncropped version of (c) is given in Appendix A (Figure A.14). The thickness for all three simulations was set to 71 nm.

### 4.4.1 Finding Polarization Direction from PED Simulations

The CBED and PED simulations can be used to find the polarization direction of the domains in grain $f$. Although it is not immediately obvious for the human eye from Figure 4.18, the simulated diffraction patterns are non-centrosymmetric, and there is a difference in the intensity of the diffraction disks depending on whether the $c$-axis is pointing up (as in Figure 4.18) or down. To highlight these differences, one can simulate two diffraction patterns, one with $c$-axis up and the other down, then subtract them from each other. To save computation cost, the diffraction pattern is only simulated for one $c$-axis direction (up), and simply rotated 180° for the other $c$-axis direction (down), as this is equivalent.

The difference of the simulated diffraction patterns for the $\phi = 0°$ (CBED) and $\phi = 1°$ PED simulations at 71 nm are shown in Figure 4.19. As the difference plots in Figure 4.19 (right column) are the result of the diffraction pattern with $c$-axis up subtracted $c$-axis down, they are referred to as Up-Down. The result of reversing the subtraction order is referred to as Down-Up.

In the Up-Down PED simulation with $\phi = 1°$ in Figure 4.19 (bottom right), the $(0\bar{1}4)$ and $(01\bar{4})$ Friedel pair is marked with red circles. Comparing these two reflections in the difference PED pattern, there is a black-white inversion (i.e. one reflection is black (negative value), the other white (positive value)), and this inversion explains the ferroelectric domain contrast in VDF imaging. Imagine a SPED dataset of a grain with two domains, one with polarization up and one down. If a VDF image is generated from this SPED dataset using the upper left of the two red circles in Figure 4.19 (the one marking the black reflection), then the pixel intensities in the domain with polarization up would be the integrated intensity of the $(0\bar{1}4)$ diffraction reflection, while for the domain with polarization down, pixel intensities would be the integrated intensity of the $(01\bar{4})$ diffraction reflection. The fact that the reflection is black (negative value) in the Up-Down difference pattern means that the intensity of the $(01\bar{4})$ reflection is grater than the $(0\bar{1}4)$ reflection. Thus, in the VDF image, the polarization up domain would be darker than the polarization down domain. A VDF image generated using the other red circle (lower right) would result in the polarization up domain being brighter than the polarization down domain. The $(0\bar{1}4)$ and $(01\bar{4})$ Friedel pair is not special

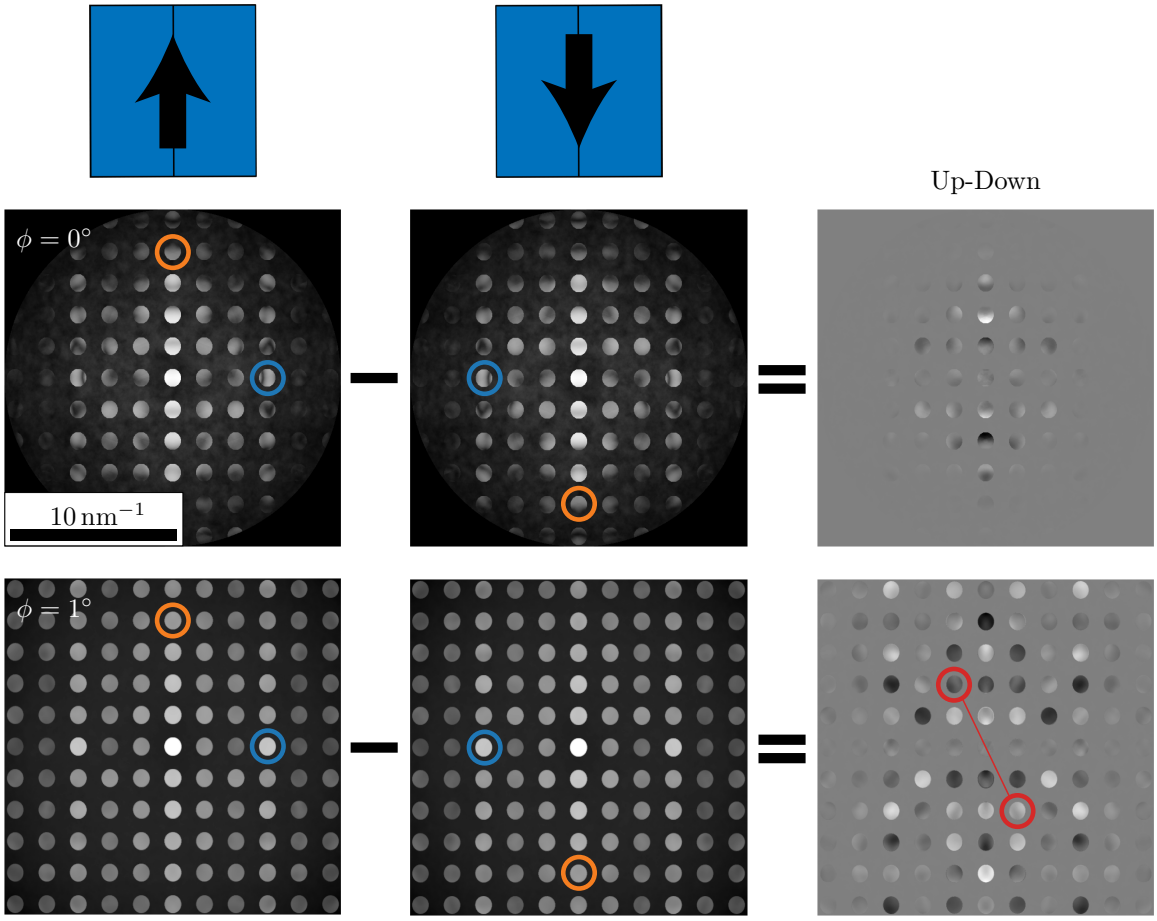


Figure 4.19: CBED ($\phi = 0°$) and PED ($\phi = 1°$) simulations of $ErMnO_3$ on the $[2\bar{1}\bar{1}0]$ zone axis with opposite $c$-axis direction (indicated by model unit cell at the top) and their (Up-Down) difference diffraction pattern. The subtraction highlights the difference in the diffraction patterns of opposite $c$-axis direction. The orange and blue circles mark the (008) and (030) reflections, respectively. The simulated diffraction patterns (left and middle column) are plotted on a logarithmic scale with a small constant offset, and the difference diffraction pattern (right column) is plotted on a linear scale where white pixels are positive and black negative. The red circles in the difference diffraction pattern with $\phi = 1°$ mark the $(0\bar{1}4)$ and $(01\bar{4})$ Friedel pair. The thickness for these simulations was set to 71 nm. The scale bar is the same for all diffraction patterns in this figure.

in this regard, as any pair exhibiting black-white inversion would have some domain contrast. In fact, most diffraction reflections in Figure 4.19 for $\phi = 1°$ could be used to generate VDF images with domain contrast.

Three (experimental) S(P)ED datasets of grain $f$ on the $[2\bar{1}\bar{1}0]$ zone axis were captured with no precession (SED), 0.5° and 1° precession, all with exposure time set to 10 ms (1 precession round). Using a 1° precession angle, a fourth dataset was captured with a 100 ms exposure time (10 precession rounds) to explore the effect of increased counts.

The experimental equivalent of the difference of simulated diffraction patterns with opposite $c$-axis direction (as shown in Figure 4.19) is calculated by subtracting the experimental PED patterns from two different ferroelectric domains in the same grain. Subtracting the PED patterns from two single probe positions in the scan is significantly influenced by noise, while summing the PED patterns from the entire ferroelectric domains picks up unwanted effects such as grain bending and/or variations in thickness. Thus, summed PED patterns from small virtual selected area (VSA) apertures were used, reducing the noise while avoid-

ing unwanted effects. The sum of PED patterns inside the VSA aperture is referred to as a virtual selected area diffraction (VSAD) pattern. In order to obtain VSAD patterns from separate ferroelectric domains, the domains were visualized using VDF imaging from the $(0\bar{1}4)$ reflection, after which two same-size VSA apertures were placed in separate ferroelectric domains, close to the domain wall separating them. Since the ferroelectric domains only need to be roughly visualized in order to place the VSA apertures, maximizing contrast is not important in this step. Thus, the $(0\bar{1}4)$ reflection was chosen arbitrarily to generate the initial VDF image.

Having both simulations of PED difference patterns with $c$-axis up and down, and the experimental equivalent (difference of VSAD patterns from separate domains in grain $f$), one can compare the two to find the polarization direction of ferroelectric domains in grain $f$. There are, however, a few challenges. Firstly, although for the simulation it is known that the result shows either Up-Down or Down-Up depending on the chosen subtraction order, the subtraction order is not known for the experimental difference of VSAD patterns because the domain polarization direction is unknown. That is, the experimental version could be $c$-axis up minus $c$-axis down or $c$-axis down minus $c$-axis up. Thus, on the simulation side, both subtraction orders need to be considered. Secondly, the simulated and the experimental diffraction patterns have a different number of pixels, and the experimental diffraction patterns are not aligned with the $c$-axis vertical. To resolve this, the experimental diffraction patterns were rotated 7.5° clockwise to have the $c$-axis vertical like in the simulations (considering the scan rotation, this means the diffraction patterns are rotated 26.5° clockwise with respect to the VDF images). The simulation and the experimental patterns were then cropped to the same field of view, and the number of pixels in the simulated diffraction patterns was changed using SciPy's `resize_local_mean` function [51] to match the experimental diffraction pattern. Lastly, the thickness of the sample is unknown, and so all the 300 simulated diffraction patterns ranging from a thickness of 25 nm to 150 nm were compared to the experimental diffraction pattern. The thickness which has the highest NCC score (Equation 2.43) for either Up-Down or Down-Up was then used to determine both the thickness and polarization direction.

The simulated and experimental difference diffraction patterns in Figure 4.20-4.23 are plotted with a red-blue color scheme, chosen to better highlight the difference between negative (red) values and positive (blue) values. The color bar has been omitted because the NCC score used to compare the simulations to the experimental data rescales the data to have a mean of zero and a standard deviation of unity, making the normalization arbitrary.

Figure 4.20(a) shows a VDF image generated from the $\phi = 1°$ SPED dataset with 10 ms exposure time. Subtracting the VSAD patterns from the two highlighted VSA apertures (blue−orange) results in the experimental difference diffraction pattern shown in Figure 4.20(b). The difference VSAD pattern has been rotated and cropped to include reflections from $(0\bar{4}\bar{8})$ (lower left) to (048) (upper right). Figure 4.20(c) shows the NCC score between the difference VSAD pattern (Figure 4.20(b)) and the simulated $\phi = 1°$ difference diffraction pattern for different thicknesses and both subtraction orders (Up-Down and Down-Up). The highest NCC score for Up-Down is 0.78 and correspond to a thickness of 71 nm. Using the Down-Up simulation, the NCC score is negative for all thicknesses. The highest (least negative) Down-Up NCC score is -0.23, corresponding to a thickness of 29 nm. Thus, the 71 nm Up-Down simulation is the best fit to the experimental difference VSAD pattern, indicating that the blue VSA aperture is placed in a domain with polarization up, and the domain in which the orange VSA aperture is placed has polarization down. Figure 4.20(d) shows the simulated difference PED pattern (Up-Down) with the highest NCC score.

For the $\phi = 1°$ SPED dataset with 100 ms exposure time, the VDF image and the two VSA apertures are shown in Figure 4.21(a), and the result of subtracting the VSAD in the orange VSA aperture from the VSAD in the blue VSA aperture is shown in Figure 4.21(b). The difference diffraction pattern has been rotated and cropped similarly to Figure 4.20(b). The NCC score (shown in Figure 4.21(c)) for the difference diffraction pattern in Figure 4.21(b) and the Down-Up $\phi = 1°$ simulation is, similarly to Figure 4.20(c), negative for all simulated thicknesses. The Up-Down simulation has the highest NCC score of 0.56 for a thickness of 66 nm, which is slightly lower than was found with the $\phi = 1°$ SPED dataset with 10 ms exposure time. The Up-Down simulation with the highest NCC score is shown in Figure 4.21(d).

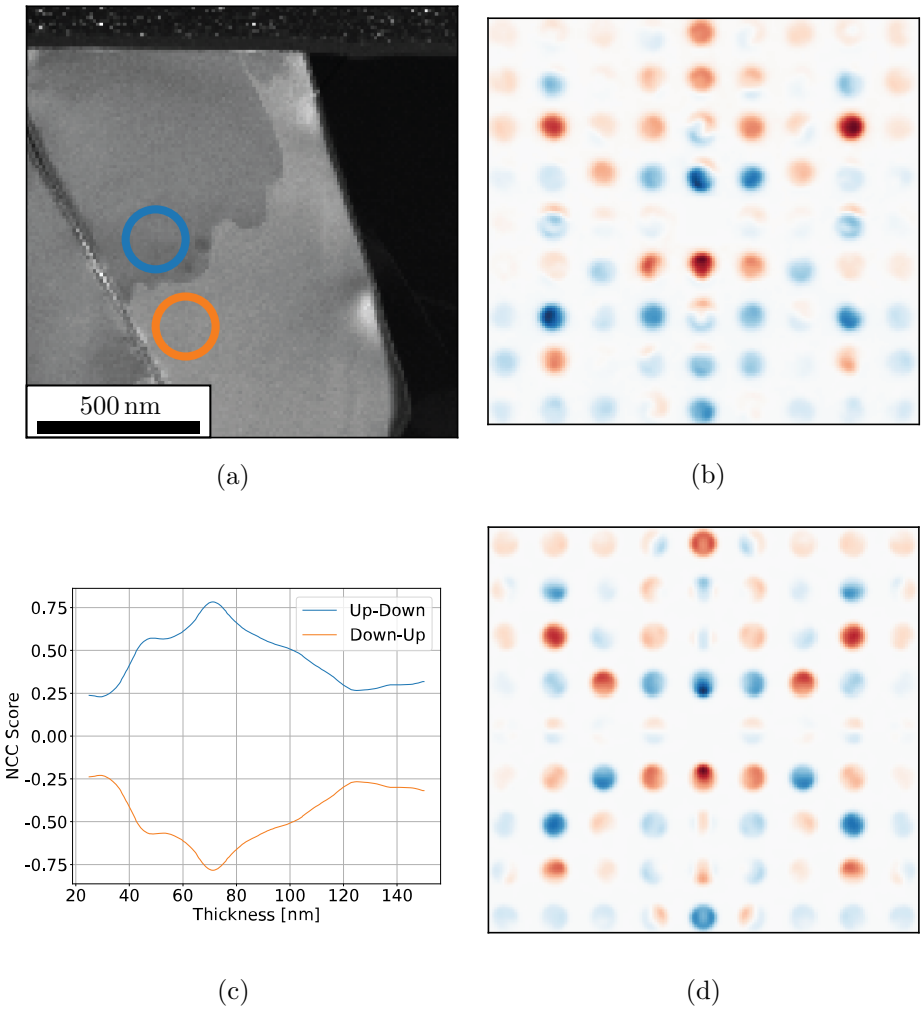


Figure 4.20: (a) VDF image from the $\phi = 1°$ SPED dataset of grain $f$ on the $[2\bar{1}\bar{1}0]$ zone axis with 10 ms exposure time. The VDF image was generated from the $(0\bar{1}4)$ reflection, and the blue and orange circles mark the VSA apertures used. (b) The difference diffraction pattern calculated from the two VSAD patterns of the blue and orange VSA aperture (blue−orange). The difference VSAD pattern in (b) has been rotated and cropped. (c) The NCC score between (b) and the simulated Up-Down and Down-Up PED patterns ($\phi = 1°$) for varying thickness. (d) The Up-Down PED simulation at a thickness of 71 nm, which is the best-fit to (b).

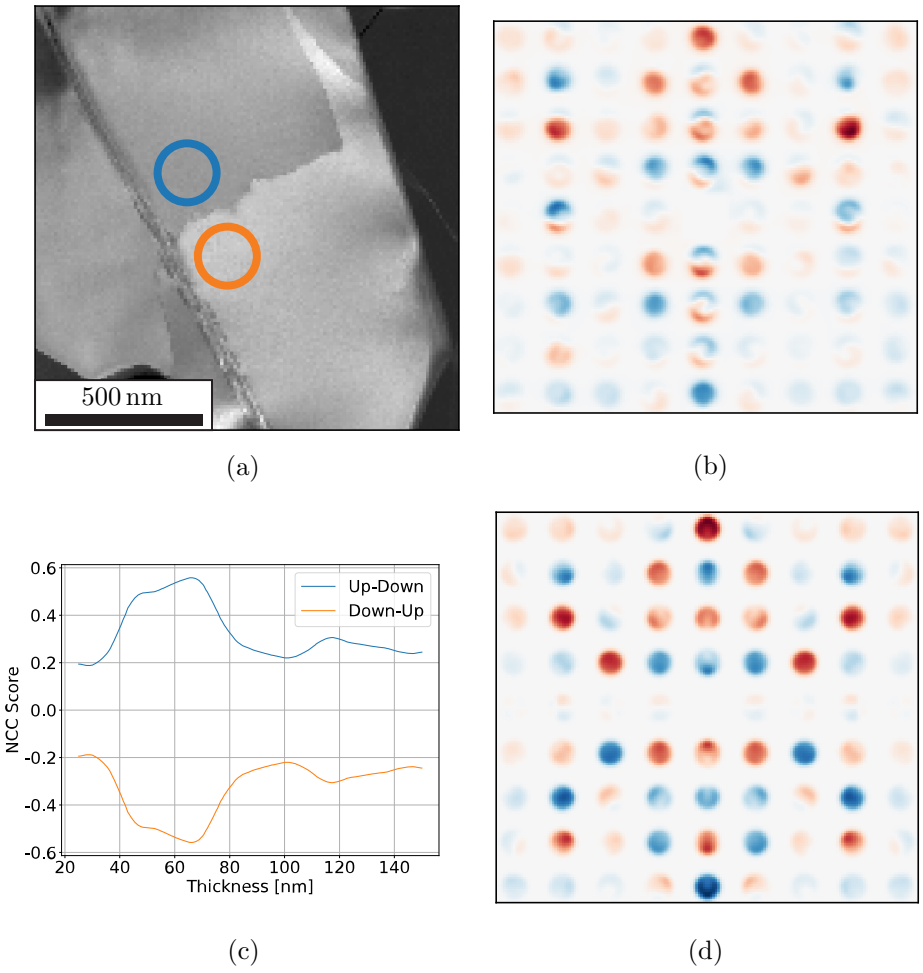


Figure 4.21: (a) VDF image from the $\phi = 1°$ SPED dataset of grain $f$ on the $[2\bar{1}\bar{1}0]$ zone axis with 100 ms exposure time. Because of the increased counts associated with the long exposure time, this dataset was captured in 24-bit mode. The VDF image was generated from the $(0\bar{1}4)$ reflection, and the blue and orange circles mark the VSA apertures used. (b) The difference diffraction pattern calculated from the two VSAD patterns of the blue and orange VSA aperture (blue−orange). The difference VSAD pattern in (b) has been rotated and cropped. (c) The NCC score between (b) and the simulated Up-Down and Down-Up PED patterns ($\phi = 1°$) for varying thickness. (d) The Up-Down PED simulation at a thickness of 66 nm, which is the best-fit to (b).

The $\phi = 0.5°$ SPED and the SED datasets had considerably less intensity for the reflections further out in reciprocal space. The difference diffraction patterns were therefore cropped to only include reflections from $(0\bar{3}\bar{6})$ (lower left) to (036) (upper right). The same analysis as for the $\phi = 1°$ datasets was performed, as shown in Figure 4.22 and Figure 4.23. Unfortunately, the experimental $\phi = 0.5°$ SPED and the SED datasets were captured slightly off zone, so there is generally more intensity in the left part of the diffraction pattern. The simulations do not account for this.

As seen in Figure 4.22(c), the highest NCC score for the $\phi = 0.5°$ was found with the Down-Up simulation at a thickness of 96 nm, resulting in an NCC score of 0.64. Compared to the two $\phi = 1°$ datasets, this thickness is substantially larger, and the polarization direction is found to be opposite. Considering only the Up-Down simulation in Figure 4.22(c), the highest NCC score is 0.38 at a thickness of 56 nm.

For the SED dataset (Figure 4.23(c)), which was compared to the CBED difference simulation, the NCC score oscillates substantially throughout the entire thickness range.

Although the highest NCC score in Figure 4.23(c) was 0.43 for the Up-Down CBED simulation at a thickness of 59 nm, which agrees better with the $\phi = 1°$ analyses than the $\phi = 0.5°$ analysis did, this appears to be mostly accidental.

In summary, the analysis of the $\phi = 1°$ datasets clearly indicate that the domain with the blue VSA aperture has polarization up, and the domain with the orange VSA aperture has polarization down. The analysis on the $\phi = 0.5°$ dataset contradicts the polarization direction results from the two $\phi = 1°$ datasets and finds a much larger thickness. Inside the thickness range 40-80nm, the $\phi = 0.5°$ analysis agrees with the polarization direction found in the $\phi = 1°$ analysis. The unprecessed data suggests the same polarization direction as the $\phi = 1°$ data did, but the NCC score oscillates substantially throughout the thickness range.

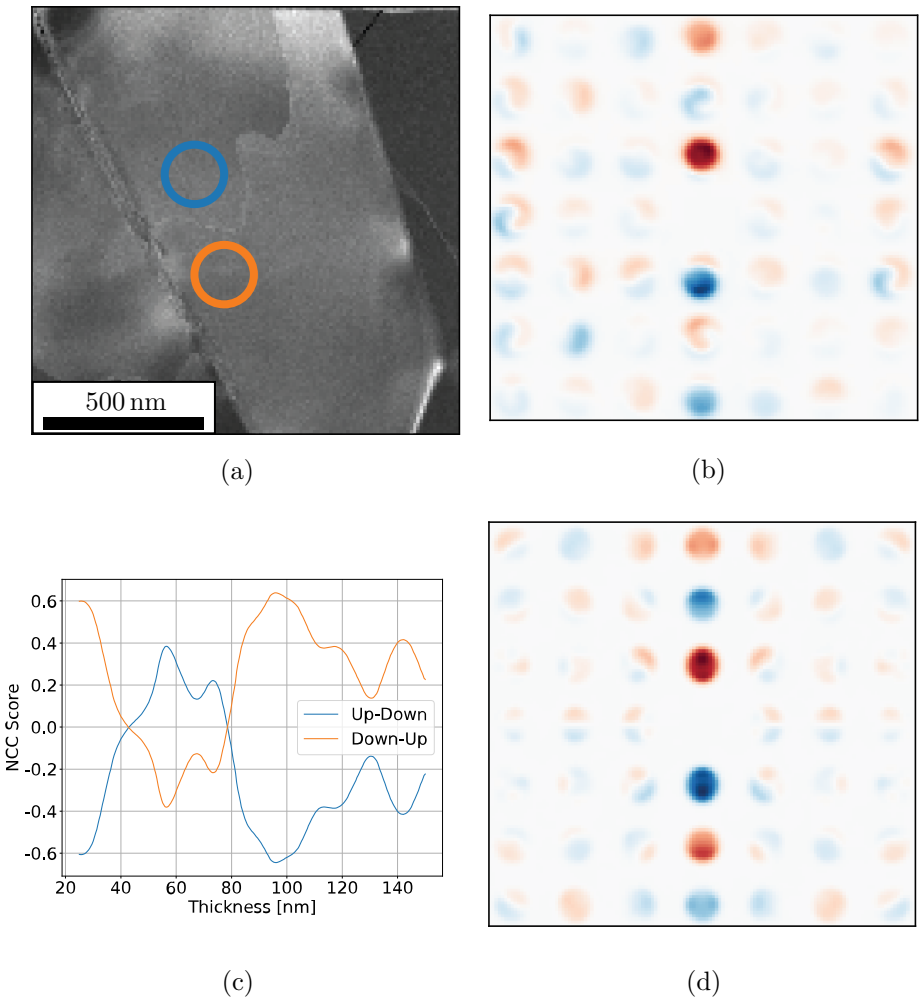


Figure 4.22: (a) VDF image from the $\phi = 0.5°$ SPED dataset of grain $f$ on the $[2\bar{1}\bar{1}0]$ zone axis with 10 ms exposure time. The VDF image was generated from the $(0\bar{1}4)$ reflection, and the blue and orange circles mark the VSA apertures used. (b) The difference diffraction pattern calculated from the two VSAD patterns of the blue and orange VSA aperture (blue−orange). The difference VSAD pattern in (b) has been rotated and cropped. (c) The NCC score between (b) and the simulated Up-Down and Down-Up PED patterns ($\phi = 0.5°$) for varying thickness. The Down-Up PED simulation at a thickness of 96 nm, which is the best-fit to (b).

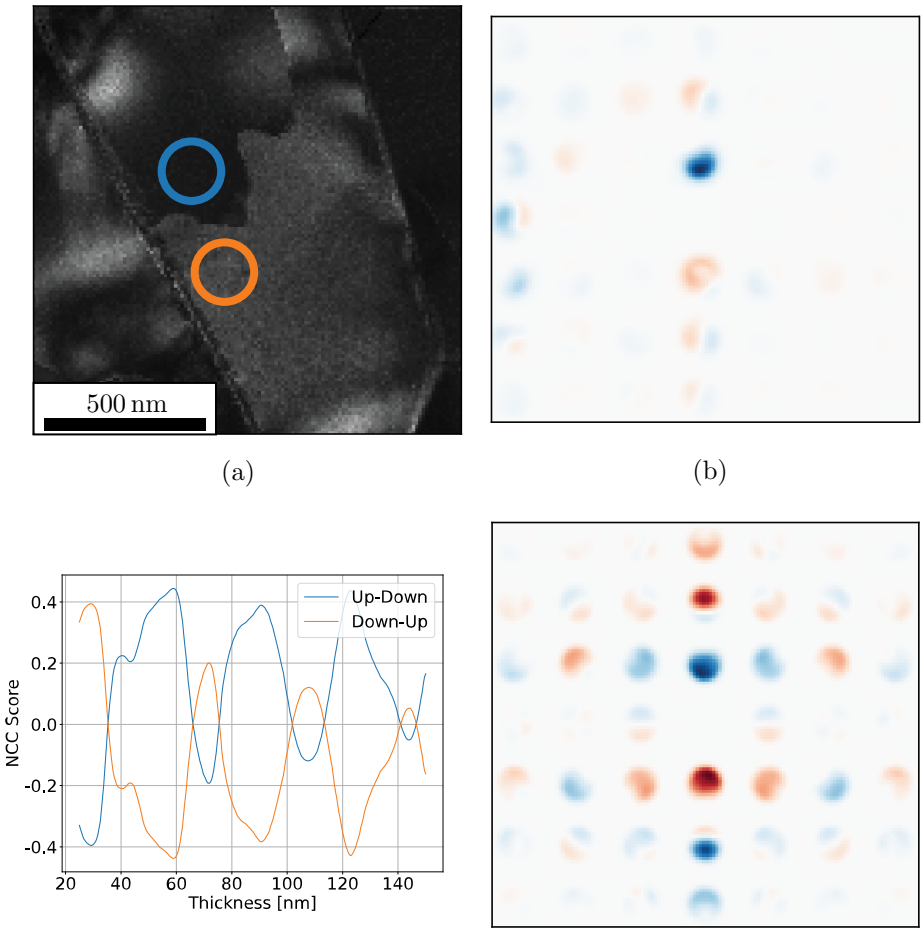


Figure 4.23: (a) VDF image from the SED dataset of grain $f$ on the $[2\bar{1}\bar{1}0]$ zone axis with 10 ms exposure time. The VDF image was generated from the $(0\bar{1}4)$ reflection, and the blue and orange circles mark the VSA apertures used. (b) The difference diffraction pattern calculated from the two VSAD patterns of the blue and orange VSA aperture (blue−orange). The difference VSAD pattern in (b) has been rotated and cropped. (c) The NCC score between (b) and the simulated Up-Down and Down-Up CBED patterns ($\phi = 0°$) for varying thickness. The Up-Down CBED simulation at a thickness of 59 nm, which is the best-fit to (b).

## 4.5 Verification of Simulation Results

Sections 4.2-4.4 show that SPED datasets (in combination with simulations) can be used to find both grain orientations and polarization directions. Additionally, they may give an indication of the specimen thickness. The polarization direction and specimen thickness results are here verified by independent measurements. To do this, the polarization direction of domains in grain $f$ is first found by high resolution HAADF-STEM in subsection 4.5.1. Secondly, in subsection 4.5.2, the thickness of the sample is measured using EELS and the log ration method described in subsection 2.4.5.

### 4.5.1 Polarization Direction

Using the aberration corrected ARM microscope, images with high spatial resolution can be used to examine the displacement of erbium atoms in the unit cell which is responsible for the ferroelectric polarization. Figure 4.24 shows two HAADF-STEM images of grain $f$ on the $[2\bar{1}\bar{1}0]$ zone axis. Figure 4.24(a) is a HAADF-STEM overview image of grain $f$ with the small blue rectangle indicating the approximate position from where the high resolution HAADF-STEM image in Figure 4.24(b) was captured. The red lines in Figure 4.24 indicate the domain wall present in grain $f$. Above this red line, in Figure 4.24(b), one can observe that the erbium atoms (the brightest dots) have an up-up-down pattern, and below the red line the pattern is down-down-up. Thus, the polarization is up above the domain wall, and down below the domain wall, as indicated by the red arrows in Figure 4.24(a). This is the same result as was found with the $\phi = 1°$ PED simulations and experimental SPED datasets in the previous section.

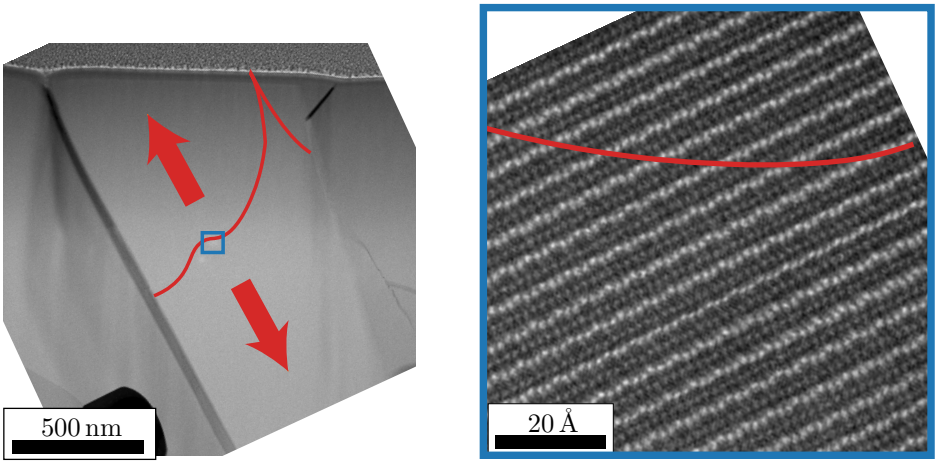


(a) (b)

Figure 4.24: (a) HAADF-STEM overview image of grain $f$ on the $[2\bar{1}\bar{1}0]$ zone axis. (b) High resolution HAADF-STEM image captured around the position of the blue rectangle in (a). The red line indicates the position of a domain wall in the grain, and the red arrows show the ferroelectric polarization of the two domains determined from lattice imaging. The displacement of erbium atoms (the brightest dots) in the unit cell is seen in (b). Above the domain wall (red line), the erbium atoms follow an up-up-down pattern (polarization up) and below they follow a down-down-up pattern (polarization down). The dimmer rows of atoms between the erbium up-up-down/down-down-up lines are manganese. The images in this figure were captured by Dr. Emil Frang Christiansen on the ARM TEM.

### 4.5.2 Sample Thickness

The thickness of the sample was mapped out using EELS and the approach described in subsection 2.4.5. With the experimental parameters of an acceleration voltage of 200 kV, a convergence angle ($\alpha$) of 27.42 mrad, a collection angle ($\beta$) of 66 mrad, and $ErMnO_3$ having a density of 7.29 g cm$^{-3}$ [41], $\lambda$ is calculated from Equation 2.30 to be about 112 nm. The EELS scan was captured with 0.1 eV per channel. The resulting thickness map from the EELS scan is shown in Figure 4.25.

The red rectangle in Figure 4.25 approximately marks the region in grain $f$ where the simulation analysis in section 4.4 was done. From the EELS data, the thickness in this region was determined to be 66.5± 4.8 nm, which is similar to the findings in the $\phi = 1°$ analysis in section 4.4.

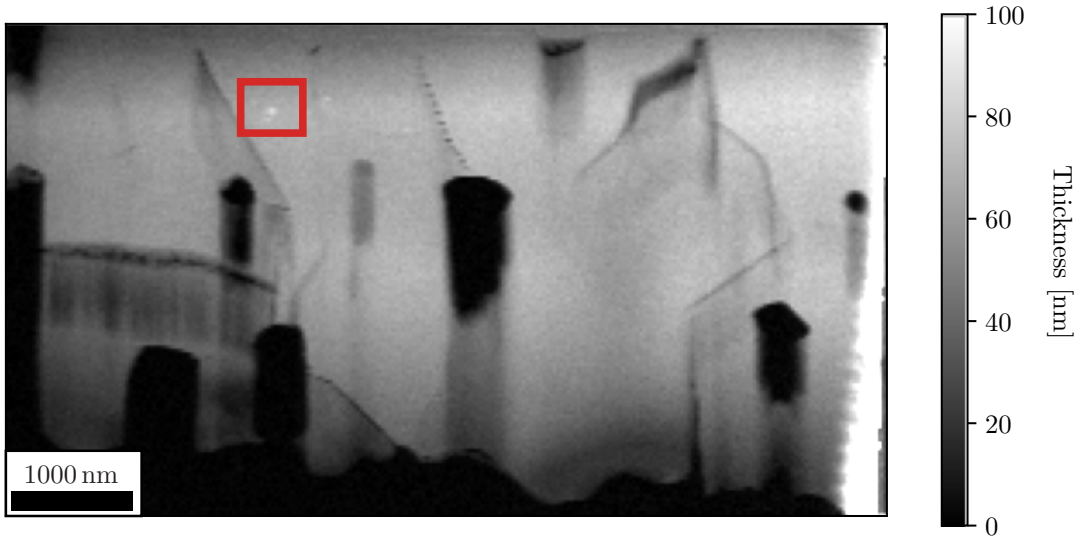


Figure 4.25: The thickness map calculated from the EELS scan of the sample. The red rectangle marks the region in grain $f$ where the PED simulation analysis presented in section 4.4 was done. The thickness found from EELS in this region is $66.5 \pm 4.8$ nm. The EELS data used to generate this figure was collected by Dr. Emil Frang Christiansen on the ARM TEM.

# Chapter 5

# Discussion

In this chapter, the results and used methods presented in the previous will be discussed. From this discussion, a conclusion and suggestions for further work are presented in the next two chapters.

## 5.1 The Specimen

The polycrystalline $ErMnO_3$ FIB lamella studied in this work is generally a well-prepared specimen. The thickness is mostly the same across the entire specimen, and the crystalline integrity of the grains is intact. FIB specimen preparation is routinely used for single crystalline $ErMnO_3$ studies [11, 46], and sample preparation artifacts are not reported. Polycrystalline $ErMnO_3$ is less studied, and no FIB preparation is reported. In the sample synthesis, small pores and microcracks are unavoidable [48]. The observed holes in the specimen are probably pores that have been enlarged during the FIB thinning step of the specimen preparation. And the streaks of thinner regions and curtaining artifacts below holes and cracks are probably caused by somewhat uneven milling below the defects. Although the Pt protection layer reduces such artifacts, some beam damage from the FIB is unavoidable.

The specimen contains grains of different sizes. The sample synthesis route followed to make the specimen studied here is reported to give a mean grain size of about 1.5 µm [13]. This is in line with observations in the TEM. By measuring the area of the 26 largest grains in the specimen, and assuming a circular grain morphology (as was done in [13]), the mean grain diameter is found to be 1.0±0.6 µm. It is, however, important to note that the specimen studied here is a ∼66 nm slice of a bulk sample and may not show the full diameter of grains.

Recent experimental studies on polycrystalline $ErMnO_3$ have shown that strain in the material has as considerable effect on the structure of ferroelectric domains [6, 13]. A general problem with TEM studies is the inevitable strain relaxation associated with creating extremely thin specimens [52]. Thus, the findings in this work may not be fully representative of the properties of a bulk polycrystalline $ErMnO_3$ sample. It is believed that grain size and orientation is not affected, but the size and shape of domains may depend on specimen thickness.

## 5.2 Orientation Mapping

The template matching routine presented in subsection 2.6.3, subsection 3.3.2 and section 4.2 proves to be a fast and reliable method for mapping out crystallographic orientations of grains in the polycrystalline specimen. The SPED dataset can easily be made to cover a relatively large area such at the 8.5 × 4 µm sample used here, allowing detailed data collection to be

carried out in a relatively short timeframe. The SPED dataset covering the entire sample (presented in Figure 4.8) was captured with $600 \times 280$ probe positions, and with a dwell time of 10 ms, this took just below 30 minutes to capture. Smaller scans like the ones in Figure 4.11 with $128 \times 128$ probe positions and 10 ms dwell time takes about 3 minutes. The data analysis is slower, and template matching on these two datasets took about 80 and 8 minutes, respectively.

Scans covering even larger areas than the one in Figure 4.8 (field of view is $9.3 \times 4.4$ µm) would to a larger extent be influenced by scan errors (i.e. tilt/shift impurity) which degrades the final result. Tilt-impurity (shifts of the entire diffraction pattern between probe positions) can often be corrected by "beam centering" (see subsection 3.3.2), however shift-impurities cause geometric distortions in VDF/VDF images which are harder to correct. The maximum scan range for the 2100F is unknown, but the range for Figure 4.8 is larger than what is commonly used. The largest SPED field of view reported previously using the 2100F at the TEM Gemini Centre-Trondheim node is $8 \times 8$ µm [53]. Still, by comparing with conventional BF-TEM images of the specimen (Figure 4.1), no significant geometric distortions are observed.

Orientation mapping with template matching on SPED is only reliable when parameters of the procedure have been optimized. The parameter space is quite large, with experimental parameters such as precession angle and exposure time, and data processing parameters such as preprocessing and library generation parameters all having an impact on the final result. The template matching in this thesis all used the same experimental parameters of 1° precession angle and 10 ms exposure time, and the same data processing parameters given in subsection 3.3.2. In the project report preceding this thesis [15], the parameter space of template matching was explored extensively, and it was verified that the parameters used in this thesis are the ones that gave the best results there. Still, the parameters could probably be improved further to increase the reliability of template matching. In the project report, it was found that precession angles of 0.5° and 2° could give correct template matching results as well, but SED (no precession) did not work well and resulted in nearly random orientations for each pixel.

### 5.2.1 Benefits of Template Matching on SPED Data

Template matching on SPED data is not the only way to determine the crystallographic orientation of grains in a polycrystalline sample. A commonly used technique is electron backscatter diffraction (EBSD), which is a scanning electron microscopy (SEM) based technique that can be used to do orientation mapping. In EBSD, a kikuchi pattern is obtained from each probe position in a scan, which can be compared to simulations to determine crystallographic orientation [54]. This approach has previously been used to determine the crystallographic orientation of grains in polycrystalline $ErMnO_3$ [13]. Sample preparation for EBSD is much simpler as a polished bulk sample may be investigated directly (carbon coating for enhanced conductivity may be required), and the angular precision of the found orientation is generally better than with SPED (ca. 1° vs 0.01° [37, 55]). A further benefit of EBSD is that larger areas may be investigated, allowing more statistically significant conclusions to be made. The main benefit of SPED compared to EBSD is superior spatial resolution. In a review of orientation mapping in SEM and TEM by Zaefferer [55], the lateral resolution in EBSD was determined to be limited to about 20-200 nm (depending on material and experimental parameters). This limitation is mainly caused by the increased interaction volume in SEM. In SPED, it has been reported that precession angles less than 1° tends to have the same effect on resolution as a Gaussian blur with a width of about 2 nm when compared to SED, resulting in a spatial resolution of a few nm (above 1° precession angles,

spatial resolution quickly degrades) [30, 55]. Nordahl *et al.* showed that spatial resolution in SPED can be improved by correcting for probe wandering by precession path segmentation [56]. Their approach was to capture $N$ images (they used $N = 8$, normal SPED is $N = 1$) of the diffraction pattern as the beam precesses in each probe position of the scan. In post-processing, the different images of the precession path can be correlated, reducing the effect of probe wandering and improving spatial resolution. Even without precession path segmentation, the spatial resolution in default SPED is much better than EBSD.

For the overview SPED dataset covering the whole specimen (Figure 4.7), with a nominal step size of 20.8 nm (calibrated step size 15.4 nm), the focus was on scanning the whole lamella with sufficient spatial resolution to analyze grain orientations rather than optimizing for the best possible spatial resolution. However, the spatial resolution could be improved simply by reducing the step size and increasing the number of pixels. This would of course come at the cost of increased acquisition time, data processing time and dataset size. If the studied area can be limited, for example studies of single grains or grain boundaries (e.g. Figure 4.11), a smaller step size can still give acceptable acquisition times. This report will not go into further details about the optimal experimental set-up (step size, probe size, convergence angle, precession angle) for spatial resolution in SPED. For the present study and goals, the spatial resolution is adequate for getting an overview of the grains in the sample, and higher resolution scans can be made covering smaller regions.

### 5.2.2 6/mmm and 6mm Symmetry

As mentioned, the orientations found through template matching are, by design, in the centrosymmetric Laue group of the crystal point group symmetry, even when the actual point group symmetry is non-centrosymmetric (orientations here are determined in 6/mmm while $ErMnO_3$ has 6mm point group symmetry). The reason for this was the inability of the kinematic approximation in the generation of the library of simulated diffraction patterns to resolve the non-centrosymmetric point groups. If a dynamical simulation had been used to generate the diffraction library, template matching could theoretically have been used to find orientations in the 6mm point group, thus finding the polarization direction directly. In the paper introducing template matching with Pyxem [37], they hint at a future version which may support dynamical simulations, though they do not state how this could be achieved. As of writing this thesis, dynamical simulations have not been implemented for template matching in Pyxem, and it seems unlikely that brute force template matching with dynamical simulations is achievable with the state of computers today.

An order of magnitude estimation on computation time highlights the challenge of using dynamical simulations for template matching. As shown in section 4.4, the intensity of diffraction reflections fluctuate as a function of thickness, and so the library of dynamical simulated diffraction patterns would need to include thickness in addition to crystallographic orientation. Generating this library would take a long time (keep in mind that the $\phi = 1°$ simulation in section 4.4 for a single orientation took 26 hours on a fairly powerful workstation computer), but only needs to be done once (library can be reused for same material) and can probably be done much more efficiently than in section 4.4. Ignoring the library generation part and focusing on the correlation score calculation (Equation 2.44) for comparing the experimental PED patterns to the simulated library, the computation time is still way too large. Moving from 6/mmm to 6mm symmetry, the size of the symmetry reduced orientation space doubles, let's also assume we include 100 thicknesses for each orientation in the library. For template matching with a dynamical simulated library, the sparse summation in Equation 2.44 does not really make sense as it utilizes very little information from the simulated diffraction pattern, and so let's assume that the summation in that equation goes

from summing over the max 100 diffraction reflections in the kinematically sparse simulated diffraction patterns, to summing over the full 256×256 pixels of the experimental PED patterns. This would increase computation time five orders of magnitude, which means that the 80 minutes computation time for the template matching that resulted in Figure 4.7 would become about 20 years. Thus, the brute force template matching algorithm with dynamical simulations is likely not possible, but refinements on normal template matching determined crystallographic orientations using dynamical simulations could be achievable.

The additional symmetry of 6/mmm compared to 6mm has impact on the deductions made from the orientation mapping. For instance, the misorientation and *c*-axis angles at grain boundaries presented in Figure 4.9 both have a range of 0-90°. In the 6mm point group, however, the range of possible misorientation angles and *c*-axis angles is 0-180°. Generally, the ray through the *c*-axis is found through template matching, but not the direction of the *c*-axis. The limitation to the Laue groups in template matching is not ideal, but a workaround using VDF images from SPED was used to resolve the non-centrosymmetric $ErMnO_3$ crystal.

### 5.2.3 Reliability of Template Matching

Orientation maps from template matching are often presented as color maps like Figure 4.6, or with plotted unit cells like Figure 4.7, but how close the found orientations are to the true orientations (the angular resolution/accuracy), and what the typical artifacts of template matching are, are not commonly debated or addressed in sufficient detail in publications that apply the method for material characterization [57]. The reliability of template matching can be measured in many ways, and should be considered both in terms of precision and accuracy. Accuracy describes how close the measured orientations are to their true value i.e. the actual crystallographic orientation, while precision describes the spread of the measured orientations [57].

The easiest method for estimating precision of template matching is to compare the determined orientations for each pixel within grains by their color. The orientations within a grain should, by the definition of a grain, be the same (if one ignores bending across the grain). Based on the uniformity of the colors in Figure 4.6, template matching appears to be fairly precise for most of the grains. Uniformity of color is a very qualitative measure for precision, and a better method is to calculate the misorientation angle of each pixel to the mean orientation of the grain. This is plotted in Figure 5.1, and shows that the misorientation angle is below 1-2° for most grains. For grain *o*, there is considerable grain bending towards the bottom, and the misorientation angle to the mean orientation is therefore much higher. The left part of grain *m* also features a region with increased misorientation angles of about 4°. This region is separated from the rest of grain *m* by a microcrack, and is slightly misoriented with respect to the rest of the grain, explaining the increased misorientation angle. As these regions with increased misorientation angles to the mean grain orientation are explained by actual changes in orientation throughout the grains, the estimation for angular precision remains at around 1-2°.

Having precise measurements of orientations should not be confused with having accurate measurements as making the same mistake in template matching consistently throughout a grain would result in a precise (uniform color), but inaccurate (wrong color) orientation determination. As the tilt series in Appendix B and Figure 4.11 showed, the [0001] zone axis is often chosen (with uniform color) by the template matching routine, even when it is not the actual zone axis of the grain. Figure 5.2(a) illustrates this problem, where a zoom in on grain *h* in Figure 4.7 is shown. As indicated by the model unit cell, template matching determined that grain *h* is in the [0001] zone axis, but the PED pattern in the insert shows

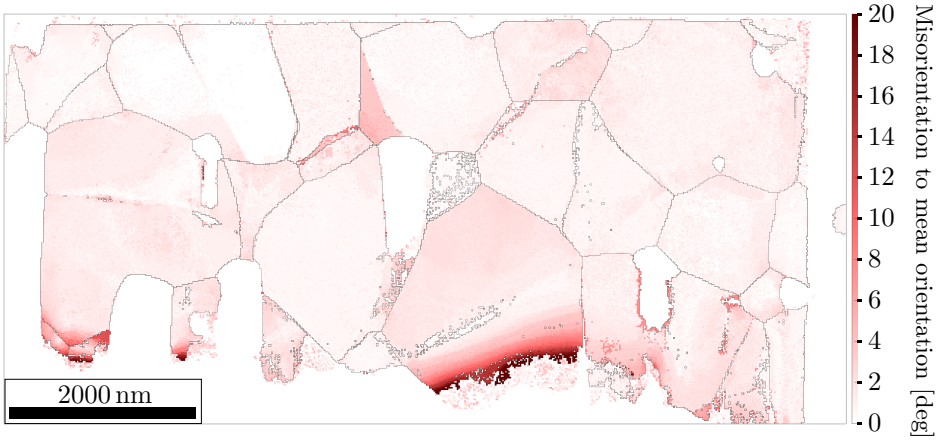


Figure 5.1: Misorientation angle to the mean orientation for each grain in the specimen.

that this is not correct. Comparing the PED pattern in the insert of Figure 5.2(a) to the PED pattern from the actual [0001] zone axis in Figure 4.3(b), it is clear that they are not the same. Still, the PED pattern in Figure 5.2(a) is close to the [0001] zone axis, and so there are multiple diffraction reflections that match well with the simulated diffraction pattern from the [0001] zone axis, as indicated by the red crosses plotted on top of the PED pattern (same type of plot as "Best Match" in Figure 4.5). This causes the [0001] zone axis diffraction simulation to have the highest correlation score from the simulated library. Thus, although grain $h$ is shown in Figure 4.7 to be in this zone axis, this result is not accurate. In the tilt series with increasing angle between the $c$-axis and the imaging plane (subsection 4.3.2), grain $h$ was determined to be on the [0001] zone axis for an $x$-tilt of 4° and a $y$-tilt of 9.7° (Figure A.13), while the SPED dataset in Figure 4.7 was captured at an $x$- and $y$-tilt of 3.2° and 2.4°.

A further example of precise but inaccurate template matching results is the amorphous electron beam deposited Pt protection layer at the top of the lamella, which is fairly consistently being determined to be close to the [0001] zone axis, as shown in Figure 5.2(b). This means that the prediction is fairly precise, but not at all accurate as the layer is amorphous and not even $ErMnO_3$. The reason for this is that the simulated library of diffraction patterns only includes simulations of crystalline $ErMnO_3$, and so the template matching will not consider an amorphous region as a possibility. The rings from the amorphous diffraction happen to line up with some diffraction reflections close to the [0001] zone axis, which explains why this zone axis is chosen (inplane rotation is random). Figure 5.2(b) is a zoom in on Figure 4.7 around grain $p$, which has a large crack through it. In this crack, there are also amorphous regions (likely caused by FIB beam damage in specimen preparation), which again are determined to be in the [0001] zone axis as indicated by the red color.

Template matching will predict orientations even for holes in the specimen (vacuum), but this can easily be filtered out by thresholding on the correlation score (Equation 2.44) as the highest possible correlation score for vacuum is very low. This is to a certain extent also true for the nanocrystalline ion beam deposited Pt protection layer above the amorphous electron beam deposited Pt protection layer. Because the diffraction rings from the amorphous Pt protection layer line up with diffraction reflections from simulated [0001] zone axis, the correlation score is fairly high and thus harder to remove by a threshold without also removing parts of the orientations determined in the actual specimen. A possible solution to this

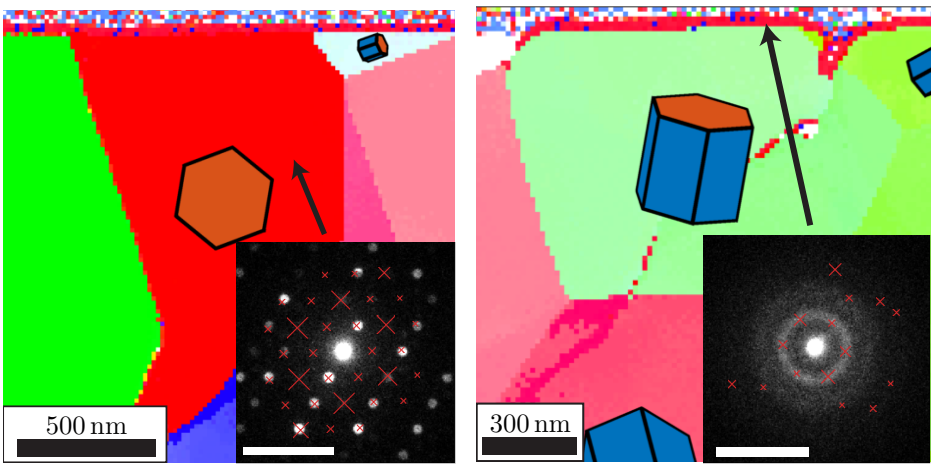


(a) (b)

Figure 5.2: Examples of precise, but inaccurate template matching results in the Figure 4.7 orientation map. (a) Zoom in on grain $h$ with a PED pattern from this grain in the insert. (b) Zoom in on grain $p$ with a PED pattern from the amorphous Pt protection layer in the insert. The red crosses plotted on top of the PED patterns are the best fitting simulated diffraction pattern showing that template matching wrongly determined these to be on (a) or close to (b) the [0001] zone axis. The scale bars in the inserts are $10\,\mathrm{nm}^{-1}$.

problem is to include a simulated amorphous diffraction pattern in the library, however by being aware of the specimen preparation and examining the data, one can safely ignore these artifacts.

The [0001] zone axis artifacts presented above illustrate that precision alone is not a good measure for the reliability of template matching, and that accuracy is just as, if not more important. In this work, the mean misorientation angle to the average orientation of the transformed orientations in a tilt series (presented in Figure 4.12) was used as a measure for accuracy. Here, it was found that the angular error range for orientation determination by template matching on SPED data is approximately 0.5-0.6°. This is slightly lower than the 1° error range that has been reported for template matching using Pyxem previously [37]. For grain $h$, the error was 5.26°. This larger error is mainly caused by the [0001] zone axis problems. Hence, this approach for measuring template matching accuracy shows that the accuracy of template matching is not uniform across the orientation space, and appears to increase close to low index zone axes.

A drawback of this measure for template matching accuracy is that a range of different factors have an impact on the measured accuracy range. Firstly, the tilt mechanism of the double tilt holder is mechanical and has some slack, which can cause the reported tilt angle of the goniometer to be a slightly incorrect (Wang estimated in his PhD an average error of 1.75% on a JEOL JEM-2100 [58]). Additionally, the position of the gonio tilt axes (found in Appendix B) also has an error range, impacting the final result. A better method for determining the accuracy of template matching would be to study a sample with a known crystallographic orientation or orientation relationship. Morawiec *et al.* [57] suggests using a twin $\Sigma 3$ misorientation in FCC materials (which has a known misorientation) to measure accuracy. This way, the results of template matching can be compared to a ground truth. For the specimen studied here, the grain orientations appear to be random, and so there is no ground truth to compare with. The average orientation after transforming back from multiple different sample tilts therefore served as the ground truth to compare with.

A different problem with template matching are the pseudosymmetries. These are exper-

imental artifacts where the diffraction pattern from one crystallographic orientation appear similar to another non-equivalent orientation. This is likely what caused two unit cells to be plotted inside grain $n$ in Figure 4.7. Pseudosymmetries were also observed in the tilt series in Appendix B for grain $j$ in Figure B.1(l), and are problematic because the result of template matching is not correct. Although problematic when only a single scan is captured, the pseudosymmetries are readily solved by reorienting the sample slightly, as shown in Figure 4.8. Ideally, three or more SPED datasets with different sample tilt should therefore be captured to allow for internal consistency checks (i.e. transforming to a reference gonio tilt) in the template matching. This may for various reasons not always be possible (for instance limited time on the TEM or beam sensitive material). In this case, all hope to resolve pseudosymmetries may not be lost. In template matching with Pyxem, it is possible to return the $n$ orientations that have the highest correlation score, and not just the single highest. For a high enough $n$ (probably below 20), the correct orientation will be among the $n$ returned orientations, along with the pseudosymmetric orientations. Starting from all the $n$ returned orientations, one could refine the template matching result. The refinement would iteratively maximize the correlation score by simulating diffraction patterns from new orientations close to the initially determined orientation and calculate the correlation score in a loop. It is expected that pseudosymmetric orientations would end up at a lower maximum correlation score compared to the actual crystal orientation after refinement, thus resolving the pseudosymmetry. Pseudosymmetries have been addressed in the literature for orientation mapping by pattern matching on EBSD data, where similar refinement approaches as described above have yielded good results [59, 54], but such refinements are currently not implemented for template matching on SPED with Pyxem.

To summarize, with the SPED data used in this work, and the optimized template matching parameters, the accuracy of the determined orientations is generally below 0.7°, with exception to certain specific orientations around low index zone axes with worse accuracy, and that the angular precision is generally below 1-2°.

### 5.2.4 Deductions from Orientations

Using the results from template matching to make deductions about aspects of the specimen is the main reason for doing template matching. The different aspects of the grains in the specimen that can be deduced from orientation maps such as misorientation angles, angles between $c$-axes and angles between the $c$-axis and the imaging plane reveal important properties about the specimen. These aspects will however only ever be as correct as the orientation mapping is correct. Thus, the misorientation angles and $c$-axis angles for the grain boundaries around grain $h$ presented in Figure 4.9 are not correct because the orientation mapping of grain $h$ was not correct. As with pseudosymmetries, the solution here is to capture multiple SPED datasets from different gonio tilts to allow internal checks to identify grains where orientation mapping fails.

Given the limited number of grains in the specimen, the grains in $ErMnO_3$ appear to be randomly oriented. There does not seem to be any specific misorientations between grains or special grain boundary shapes appearing more frequent than others. For crystalline materials where the crystal orientations are not random, such as twinning $\Sigma 3$ in FCC materials, it makes sense to visualize the misorientations in the misorientation space (similar to orientation space, can be visualized in IPF) to highlight the misorientation relations [22, 60]. In Figure 4.9(a), only the misorientation angles at grain boundaries are plotted (and not also the misorientations in an IPF) because the orientations are random, and so plotting the misorientations in an IPF would give no further significant insight.

Although orientations appear random, the angle between $c$-axes at grain boundaries (Figure 4.9(b)) are interesting to study in $ErMnO_3$. This is because this angle is related to the bound charge at the grain boundaries though Equation 2.45. To actually compute the bound charge at the grain boundary, the normal vector of the grain boundary needs to be determined. If one assumes that the grain boundaries in the specimen are edge on, meaning that the normal vector is in the specimen plane, the $\approx 90°$ $c$-axis angle between grain $b$ and $d$ results in an expected bound surface charge of $|\rho| \approx 6\,\mu C\,cm^{-2}$, where the sign of the charge is dependent on the polarization direction of grain $b$. For the grain boundary between grain $f$ and $h$ (ignoring for sake of argument that template matching on grain $h$ failed), which also has a $\approx 90°$ $c$-axis angle, the bound charge is roughly zero. This is because the normal vector of the grain boundary is roughly perpendicular to $(\mathbf{P}_1 - \mathbf{P}_2)$ for grain $f$ and $h$, which is not the case for grain $b$ and $d$. In reality, the grain boundaries of the sample may not be edge on, meaning that the normal vector of the grain boundaries have a non-zero $z$ component. This complicates the bound charge analysis significantly, and is not done for this thesis.

## 5.3 Orienting to a Zone Axes

In subsection 4.2.4, a tilt series was introduced and the found orientations from template matching were transformed back to a reference gonio tilt in order to estimate template matching accuracy. This transformation essentially answers what the crystallographic orientation of grains would be given that the gonio tilt is $(x, y)$ instead of the $(x_0, y_0)$ at which the SPED data was captured. The method for finding the $(x, y)$ gonio tilt that orients grains in the sample to a chosen zone axes (presented in subsection 4.2.5) essentially used the same approach in reverse. Namely, asking what the gonio tilt would have to be in order to have a certain grain orientation.

This approach presented in subsection 4.2.5 is a powerful tool that can accelerate the productivity on the TEM significantly. Without this tool, many of the analyses performed in this thesis, like the ferroelectric domain contrast for varying angles between the $c$-axis and the imaging plane (Figure 4.17), would simply not be possible in a reasonable timeframe.

The transformation (Equation 2.25) naturally requires that the orientation in the reference specimen tilt was determined correctly, and as discussed in subsection 5.2.3 there can be misindexations. For instance, the software predicted sample tilt for grain $h$ in the [0001] zone axis is an $x$-tilt of 3.4° and $y$-tilt of 2.5°, while the experimentally found sample tilt for this zone axis is an $x$-tilt of 4.0° and a $y$-tilt of 9.7°, which is an Euclidean distance deviation of 7.2°.

The deviation between the software predicted sample tilt and actual (experimentally found) sample tilt for different zone axes (presented in Table 4.1) of 0.73° is quite small and comparable to the accuracy of template matching and the inaccuracy of the sample holder tilt readings. Considering the mechanical slack in the double tilt holder, beam alignment deviations between TEM sessions, and template matching accuracy, this is really as small as one can hope for. When actually using this method during a TEM session, after setting the predicted sample tilt, one is so close (within <1°) to the target zone axis that it is easily identified. Manually fine-tuning holder tilts to the target zone axes from this start position is therefore trivial.

Note that the method for finding holder tilts for target zone axes relies on knowing the crystal orientation of grains and relating this to the gonio tilt axes. It therefore works best when the sample is left in the sample holder between TEM sessions. The workflow of this method starts with a TEM session where a SPED dataset covering the grains of interest is acquired, and before the next session, template matching is performed to find the

crystallographic orientation of the grains. However, if the sample is inserted in a different orientation in the sample holder the next session, it becomes harder to relate crystallographic orientation of grains to the gonio tilt axes. If leaving the sample in the holder is not an option, one could try to compensate for the inevitable in-plane rotation associated with taking the sample in and out of a sample holder. This works best if a characteristic feature (like the top of the lamella) is aligned with the scan X (or Y) direction in the initial scan of the specimen, which is achieved by adjusting the scan rotation. In the next TEM session, after template matching on the initial SPED dataset, the difference in the in-plane rotation of the specimen can be found by once again adjusting the scan rotation so that the characteristic feature is aligned with the scan X direction. The difference in the scan rotation describes the change of in-plane rotation of the specimen, and by rotating the initial template matching results through this angle, the resulting orientations describe the grains in the new sample holder position. If the specimen is flipped upside down, the situation becomes more complicated, but this can usually be avoided by paying attention when inserting the specimen in the holder. Because the specimen was left in the same holder for the duration of this work, the reliability of this approach has not been tested.

### Other Applications of The Gonio Transformation

Finding the required sample tilt for a chosen zone axis of grains in the sample is one useful application of the transformation in Equation 2.25. However, the transformation could be used for a range of other problems as well. For instance, when studying slanted grain boundaries in TEM, it is often desired to tilt the sample so that the grain boundary is viewed edge on. This way, there is no overlap of the grains and one can for instance use HRTEM to determine if there are any intermediate phases in the grain boundary. If one somehow is able to describe the normal vector of the grain boundary, $\mathbf{n}$, in the sample reference frame, the transformation in Equation 2.25 could be used to find a sample tilt which makes $\mathbf{n}$ perpendicular to the electron beam so that the grain boundary is viewed edge on. Going a step further, the transformation could be used to find the set of all $x$- and $y$-tilts that keep $\mathbf{n}$ perpendicular to the electron beam, thus rotating the sample about the $\mathbf{n}$ axis, allowing the grain boundary to be studied edge on from multiple angles. Furthermore, if the crystallographic orientation is known on both sides of the grain boundary (by template matching), one could solve an optimization problem[1] to have the grain boundary edge on, and also the two grains close to low index zone axes, which would be highly beneficial for HRTEM.

## 5.4 Visualizing Ferroelectric Domains

Visualizing ferroelectric domains with VDF images from SPED data takes the orientation mapping with template matching a step further by showing domains within grains with opposite $c$-axis direction. The results of these two techniques complement each other, where template matching reveals the crystal orientation of grains in the sample in the 6/mmm point group, leaving the determination of polarization ($c$-axis) direction of domains within grains to the VDF images. On their own, VDF images can not fully solve this last part of the puzzle, only visualize domains with opposite $c$-axis direction, however with the aid of PED simulations the polarization direction can be completely determined (using PED simulations for this will be discussed in section 5.5).

[1] Optimization in the sense that this problem does in general not have a solution that fulfills all requirements completely.

Ferroelectric domains and domain walls in $ErMnO_3$ have been studied in TEM previously for single crystals using high resolution HAADF-STEM where the displacement of erbium atoms in the unit cell is observable [5, 46] (see Figure 4.24). A drawback of HAADF-STEM is that for $ErMnO_3$, it can only be used to study domains from the $[2\bar{1}\bar{1}0]$ zone axis, and requires a probe aberration corrected TEM. Furthermore, the studied region with high resolution HAADF-STEM is very limited ($\lessapprox$100×100 nm), and so the structure and shape of domains throughout grains can not be studied with this technique. HAADF-STEM generally also applies a higher electron dose than SPED due to a larger condenser aperture and a smaller probe size, which can cause beam damage.

A different method for studying ferroelectric domains in $ErMnO_3$ is piezoresponse force microscopy (PFM) [13]. Images covering several tens of microns can be captured with PFM, allowing the structure and shape of domains to be studied on the mesoscale. PFM can qualitatively measure both the in-plane and out-of-plane polarization, and can achieve spatial resolution down to a few nanometers (although scan times at this resolution are very slow). However, this technique can not be used to find crystallographic orientations of grains, and so although the polarization of domains can be found, it can not be correlated with crystallographic orientations without additional techniques like EBSD [13].

A third method for studying ferroelectric domains in $ErMnO_3$ is SEM, where domain contrast is achieved for polarization out-of-plane (the [0001] zone axis). Here, domain contrast is achieved at low acceleration voltages (<3 kV), which is explained by the proposed contrast forming mechanism [10]. It is proposed that different polarization direction will result in either a positive or negative surface charge, which attracts or repels secondary electrons, thus resulting in different electron yields between the ferroelectric domains. In SEM, domains with in-plane polarization can not be distinguished, but the domain walls are still visible [10].

SPED falls in between HAADF-STEM, and PFM and SEM in terms of the size of the studied region, and what polarization directions can be studied. The ability to visualize ferroelectric domains, not just in the $[2\bar{1}\bar{1}0]$ zone axis (as for HAADF-STEM), or close to the [0001] zone axis (as for SEM), but for a wide range of crystal orientations is a benefit of SPED. A further benefit is that the crystallographic orientation of grains can be found not only with the same instrument, but using the same dataset (though template matching). For the other techniques, it is either required to work in a specific, known crystallographic orientation (SEM and HAADF-STEM), or a different instrument (EBSD) is required for determining crystallographic orientations (PFM). Although SPED has some key benefits, the studied region is still limited, and so making statistically significant conclusions about the bulk sample as a whole is not possible. Furthermore, SPED requires simulations to understand the observed contrast and determine polarization direction, which is both computationally expensive and difficult for off-zone orientations. The different techniques for studying $ErMnO_3$ all have benefits and disadvantages, and so utilizing all of them for their advantage in combined studies is the best approach.

### 5.4.1 Ferroelectric Domain Contrast in VDF

Implicitly so far, it has been assumed that the sharp intensity transition within grains in VDF images are caused by ferroelectric domains. This assumption will here be justified.

The ferroelectric domains in polycrystalline $ErMnO_3$ with grain sizes similar to the specimen used for this work have been studied previously using PFM [13]. Qualitatively, the shape of the ferroelectric domains found with PFM appears similar to what is found with VDF images from SPED. Furthermore, the fact that the observed contrast in VDF images (Figure 4.16) is not present in VBF images (Figure 4.4), and that the contrast is inverted

between VDF images generated from Friedel pairs (Figure A.4), can only be explained by ferroelectric domains. Dark-field imaging in conventional TEM has previously been used to visualize ferroelectric domains in $ErMnO_3$ in the $[2\bar{1}\bar{1}0]$ zone axis [5], but off-axis ferroelectric domain contrast in DF-TEM or VDF imaging has, to the best of the author's knowledge, not been reported before and substantially increases the orientation space where domains can be studied (this is discussed further in subsection 5.4.3). A conventional DF image of grain $f$ featuring ferroelectric domain contrast is presented in Appendix A (Figure A.3). Comparing Figure A.3 to the VDF image from SPED (Figure 4.15(b)), it is clear that VDF from SPED has removed much of the assumed thickness and strain field contrast observed in the conventional DF image.

Note that the ferroelectric domain contrast observed in VDF images from SPED is likely not caused by the electric polarization of the domains, but rather by the difference in crystal structure between domains. The effect of the electric polarization in ferroelectric domains on the diffraction pattern would be a shift of the entire diffraction pattern in the direction of the polarization. The polarization in $ErMnO_3$ is very weak at $6\,\mu C\,cm^{-2}$, and so this shift is not observable. As the PED multislice simulation showed, it is the difference in crystal structure between domains that causes ferroelectric domain contrast in VDF images.

### 5.4.2 Domain Wall Dynamics and Pinning

The domain walls in $ErMnO_3$ are, as shown in Figure 4.13, mobile and can be influenced by the electron beam in TEM. Ferroelectric domains and domain walls being influenced by the electron beam in TEM has been reported previously by Hart *et al.* [61], where $KTiOPO_4$ was studied, and by Chen *et al.* [62], where $YMnO_3$, which is very similar in structure to $ErMnO_3$, was studied. Chen *et al.* found that secondary electron emissions and oxygen vacancies induced by the electron beam lead to a local net positive charge at the focused electron beam. The electric field from this positive charge was larger than the coercive field of $YMnO_3$, leading to polarization switching and domain wall movement [62]. Their findings are in line with what is observed in Figure 4.13. A schematic of the domains in Figure 4.13(a) is shown in Figure 5.3, where the domains are modeled as consisting of individual dipoles separated by a domain wall (the red line). As shown in Figure 4.24, the domain wall in Figure 4.13(a) is tail-to-tail, which is reflected in Figure 5.3. Between capturing Figure 4.13(a) and (b), the electron beam was focused below the domain wall. Assuming $ErMnO_3$ behaves similar to $YMnO_3$, this induced a local positive charge some distance below the domain wall, as shown schematically in Figure 5.3. The electric field from this bound charge is directed against the dipoles located between the charge and the domain wall, causing them to switch so that the domain wall is moved down towards the electron beam (the blue line in Figure 5.3 represents the new domain wall after switching). The same argument can be used to explain why the domain wall moved back up between Figure 4.13(b) and (c), where the electron beam was focused above the domain wall.

This model can also explain why the domain walls were observed to be more mobile in the $c$-direction. To switch the polarization direction, the component of the electric field directed against the polarization needs to be higher than the coercive field of the material. For the radial symmetrical electric field from the local positive charge, this component is the largest in the $c$-axis direction.

To further test this proposed domain wall dynamics mechanism, head-to-head domain walls should be investigated. The dipoles between the local positive charge and a head-to-head domain wall would already be aligned with the electric field and thus not switch. The head-to-head domain wall should, according to this model, therefore not move towards the electron beam.

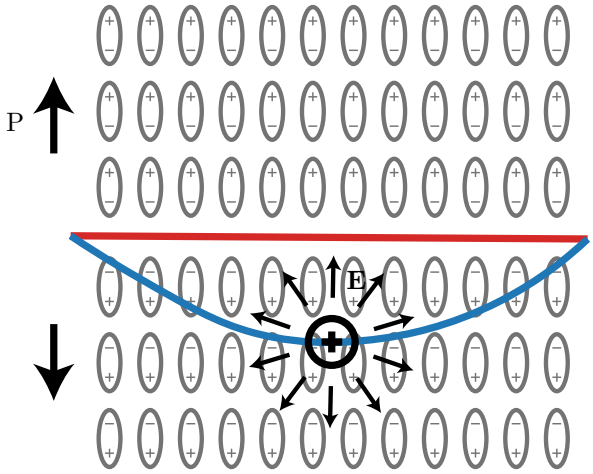


Figure 5.3: Schematic illustrating the assumed mechanism of domain wall movement induced by the electron beam observed in Figure 4.13. The electron beam is focused below a tail-to-tail domain wall (red line), inducing a local positive charge. Dipoles located between the electron beam and domain wall align to the electric field from the positive charge, which moves the domain wall towards the electron beam. The new position of the domain wall after switching is represented by the blue line.

Although domain wall movement is one of the reasons why $ErMnO_3$ is being studied in the first place, from a characterization point of view, it is somewhat undesired. It can be challenging to compare different techniques and results when domain walls are in completely different positions, or have been erased altogether between scans. The pinned domain wall in grain $f$, shown in Figure 4.14, therefore serves as a great starting position for more detailed exploration of the ferroelectric domains and the methods used to visualize them. Similar appearing pinning positions were also observed in grain $m$, as can be seen in Appendix A (Figure A.7). This pinning of the domain wall could be caused by a topologically protected state of domains (such as vortices), which are common in single crystalline $ErMnO_3$ [5, 46, 61], but less so in polycrystalline $ErMnO_3$ with smaller grain sizes like the specimen studied in this thesis [13]. Another possible explanation is that the domain wall is pinned at an imperfection in the lattice. The pinning positions in both grain $f$ and $m$ are at the very top edge of the sample, towards the amorphous protection layer, which is where Ga-ion implantation from the FIB specimen preparation is the most likely. Ga-ion implantation was proposed as a source of pinned domain walls by Roede *et al.* [63]. The domain wall could also be pinned due to a lattice defect at or close to the top of the lamella.

The pinned domain wall in grain $f$ is observed in all VDF images in this thesis. Although, in the composition VDF (Figure 4.16), the structure is not as clearly visible. The shape of the domain does, however, indicate that the domain wall is still pinned, but towards the amorphous protection layer, the domain wall is so thin that it is not visible due to the large step size (calibrated step size 15.4 nm) used for the overview scan.

To summarize, domain wall movement induced by the electron beam has been observed, and can be explained by the proposed mechanism for similar observations in $YMnO_3$ [62]. Further work should try to quantify the dynamics, investigate domain wall dynamics in head-to-head configurations, and identify the cause of domain wall pinning.

### 5.4.3 VDF Domain Contrast With Increasing Angle Between $c$-axis and Imaging Plane

The series of SPED datasets captured from zone axes with increasing angle between the $c$-axis and imaging plane systematically shows that ferroelectric domain contrast in VDF

images can be achieved even when the $c$-axis points well out of the plane. For this series, where the unit cell was tilted from $[2\bar{1}\bar{1}0]$ to $[0001]$ about the $[01\bar{1}0]$ crystal direction, the ferroelectric domain contrast generally decreases as the angle between the $c$-axis and imaging plane increases. This is expected because as the angle increases, the projected displacement of erbium atoms in the unit cell (as viewed from the imaging electrons) decreases. At 0°, the displacement is in the imaging plane (perpendicular to the electron beam) and the projected displacement is therefore at a maximum. At 90°, on the other hand, the displacement of erbium atoms in the unit cell is parallel to the electron beam, and so the projected displacement is zero, thus having no impact on the diffraction intensities.

From the 9 sampled zone axes, the loss of domain contrast was found to be when the angle between the $c$-axis and imaging plane was somewhere between 72.2° and 75°. These 9 zone axes admittedly cover a very limited part of the orientation space. If the series had started at the $[10\bar{1}0]$ zone axis and tilted to $[0001]$ about the $[\bar{1}2\bar{1}0]$ crystal direction (or anywhere in between $[2\bar{1}\bar{1}0]$ and $[10\bar{1}0]$ tilting towards $[0001]$), the maximal angle for domain contrast in VDF images would likely not be the same. Furthermore, it is also possible that there are off-zone crystal orientations in between the 9 sampled zone axes where the angle between the $c$-axis and the imaging plane is still below 72.2°, but where none of the diffraction reflections give ferroelectric domain contrast in the VDF image. Additionally, as shown with the multislice simulations in section 4.4, thickness affects the intensity of diffraction reflections. Thus, samples with different thicknesses may behave differently in terms of domain contrast.

Using the procedure for tilting to arbitrary zone axes presented in subsection 4.2.5, one could extend the ferroelectric domain contrast analysis in subsection 4.3.2 to cover larger parts of the orientation space. Experimentally, this would still be quite tedious even with aid for tilting to zone axes because SPED needs to be realigned before capturing each scan. It is therefore perhaps more beneficial to extend the analysis with dynamical simulations.

The analysis with increasing $c$-axis to imaging plane can be used to draw some conclusions about the grains where no domain contrast was observed (marked with red stars) in the composite VDF image in Figure 4.16. The grains $b$, $t$ and $z$ are all close to zone axes on the form $[2j, \bar{j}, \bar{j}, i]$, and as shown in Figure 4.10, they all have an angle between the $c$-axis and imaging plane below 72.2°, and yet no domain contrast was observed in VDF images. As discussed in this section, there are several possible explanations for this, but it could be an indication that these grains are single domain.

## 5.5 Simulations

To better understand the experimental results and go beyond just observing images, comparison with a model is often required. Here, the CBED and PED multislice simulations of $ErMnO_3$ provide valuable additional insight to the contrast observed in VDF images from SPED. The simulation results, the approach for simulating precession electron diffraction and comparing the model to experiment will be discussed in this section. Note that in template matching, simulations in the form of simple kinematic approximations giving sparse diffraction patterns were also performed, but this section addresses the dynamical multislice simulations presented in section 4.4.

### 5.5.1 The PED Multislice Simulation Method

CBED simulations with both the multislice and Bloch wave solution have become a standard tool supplementing the analysis of experimental CBED patterns [33]. There are many

packages supporting TEM simulations, including JEMS [50], ReciPro [26], Prismatic [64], abTEM [65] and the here used py_multislice (Pyms) [49]. Pyms was chosen because it is written in Python and the code is well documented. With simulations, one can explore how lens aberrations or experimental parameters such as recording noise affects the diffraction patterns. Furthermore, parameters that may be difficult or even impossible to change experimentally (for instance acceleration voltage) can be adjusted, allowing increased understanding of their effect and optimization of experiments. Ultimately, one tries to simulate the electron-sample interactions and the imaging processes in the TEM, in order to better understand experimental results.

When capturing CBED patterns experimentally on a TEM, the recordings will have imperfection due to artifacts in the TEM electron optics and recording devices. The beam tilt parameter in the CBED multislice simulations is probably intended to be used for simulating slightly off-zone CBED patterns. One could therefore argue that utilizing this parameter to simulate PED by sampling a range of beam tilts from a cone with semi-angle of the precession angle might be overextending the intentions of the CBED simulation.

Although thought of independently, using discretely sampled beam tilts to simulate PED patterns has been reported before, as discovered by the author in the final stage of this project. In 2006, C. S. Own *et al.* [66] used a multislice algorithm with $N$ discretely sampled beam tilts from a cone with semi-angle $\phi$ to simulate PED patterns of $(Ga, In)_2SnO_4$ and ZSM-5 zeolite in the [010] zone axis. In that paper, they studied the effect of increasing the number of discretely sampled beam tilts, $N$. They did this by increasing $N$ and comparing the intensities of the reflections $I_{\mathbf{G}}^{N}$ to the intensities $I_{\mathbf{G}}^{N_{max}}$ for a very large $N_{max} = 2048$, for which the simulation was assumed to have converged. They found that for larger thicknesses and higher precession angles, a finer sampling was required to have convergence. The $N_{max}$ used in [66] was an order of magnitude larger than the $N = 100$ that was used for the PED simulation in this thesis, and based on their convergence tests, $N = 100$ was probably a little coarse (at least for the $\phi = 1°$ simulation). In the $\phi = 1°$ PED simulation at the highest thickness of 150 nm, the diffraction discs of the Up-Down difference plot (shown in Figure 5.4) have a peculiar internal structure which could be an indication that the simulation had not converged. A convergence test with increasing $N$ should be performed to confirm this suspicion. Because computation time increases linearly with $N$, and the $\phi = 1°$ simulation with $N = 100$ took 26 hours on a powerful workstation computer, reaching the same $N_{max} = 2048$ for a convergence test would take more than 22 days. The exact details of the multislice implementation used by Own *et al.* is not known, but their paper does not mention the frozen phonon approximation, and so it is probable that they did not include this approximation in their simulation, which partly could explain how they were able to reach $N_{max} = 2048$ in a reasonable timeframe.

The PED simulations were quite computationally intensive. Since the method discretely samples $N$ beam tilts, a CBED multislice simulation is performed $N$ times to form a PED simulation. However, as the results of all individual beam tilt simulations are summed incoherently, they are all independent, and computation time can drastically be reduced by computing each beam tilt in parallel on a cluster. However, this would require saving each CBED simulation individually (before combining them) and thus come at the cost of increased disc space usage. The $\phi = 0.5°$ PED simulation, with $N = 100$ different beam tilts and 300 thickness steps requires about 67 Gb of disc space when the $N$ CBED simulations are saved individually. The $\phi = 1°$ PED simulation (which had a larger grid size giving more pixels in each diffraction pattern) requires approximately 450 Gb of disc space if saved individually. Parallel computation for the $\phi = 1°$ PED simulation was attempted on a cluster, but disc space limitations on the cluster made combining the individual beam tilt

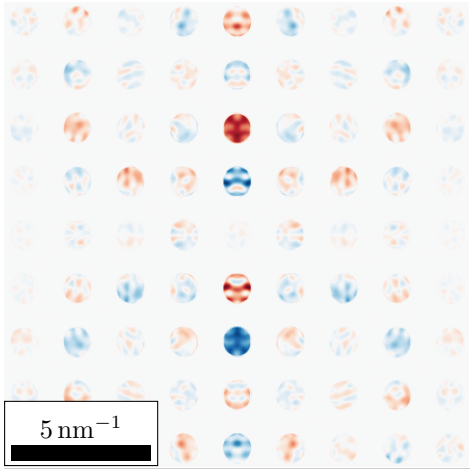


Figure 5.4: Simulated Up-Down diffraction pattern of $ErMnO_3$ in the $[2\bar{1}\bar{1}0]$ zone axis at a thickness of 150 nm. The peculiar internal structure of the diffraction discs could be an indication that the $N = 100$ beam tilt sampling was too coarse and that the simulation has not converged for this thickness.

simulations impractical. Thus, the $N$ beam tilt simulations were computed sequentially on a workstation computer, so that they could be added up as the simulation progressed, reducing the required disc space by roughly a factor $N$.

The python library Pyms which was used for the multislice simulation is built on top of PyTorch [67]. PyTorch was developed as a deep learning framework with focus on both usability and computation speed and is extensively used for neural networks and artificial intelligence. The framework makes hardware acceleration with GPU (i.e. with CUDA) both user-friendly and efficient. As Pyms is built on top of PyTorch, GPU acceleration is readily available for the multislice simulations. GPU acceleration was not used in this thesis as a computer with Nvidia GPUs was not available. If GPU computer hardware could be utilized, computation time would be reduced dramatically.

### 5.5.2 Simulation Results

Examining the results for the CBED ($\phi = 0°$) and $\phi = 0.5°$ and $\phi = 1°$ PED simulations (Figure 4.18), the general effects of precession on diffraction patterns appear to be captured by the simulations. Higher precession angles result in more intensity in the reflections further out in reciprocal space, and the internal structure of the reflection discs are reduced, making them more uniform, as expected with SPED [28]. Going back to the orientation mapping, these two effects are what make precession beneficial for template matching. More intensity further out in reciprocal space gives more information to discriminate between crystal orientations, and reduced internal structure of diffraction discs allows better matching to the position of diffraction reflections.

Comparing Figure 4.18(b) and Figure 4.18(c), it appears that the 1° precession (Figure 4.18(c)) has less intensity noise between the diffraction reflections compared to the 0.5° precession (Figure 4.18(b)). This is not really the case, but appears this way because of the cropping and normalization of Figure 4.18(c). In Appendix A (Figure A.14), the uncropped version of Figure 4.18(c) is shown, where the intensity range is the same as for Figure 4.18(b), and it is clear that the intensities between diffraction reflections are comparable to the $\phi = 0.5°$ simulation.

There is a lot of information that can be extracted from the difference plots of CBED and PED patterns with opposite $c$-axis direction, like the ones in Figure 4.19. The symmetries of these difference diffraction patterns are illustrated in Figure 5.5. From the crystal symmetry of $ErMnO_3$ (6mm) the plane containing $[2\bar{1}\bar{1}0]$ (the zone axis in the simulations) and the $c$-axis is a mirror plane. This is reflected in the difference of PED pattern where the vertical line through the $(00l)$ diffraction reflections (the red line in Figure 5.5) is a mirror line. Additionally, the horizontal line through the $(0h0)$ reflections (the green line in Figure 5.5) is an inversion line, meaning that reflections mirrored about this line are inverted (going from black to white and visa-versa). This is an effect of subtracting two images, with a vertical mirror line, that are 180° rotated with respect to each other. Imagine rotating the images on both sides of the equation in Figure 4.19 180°. This is the same as reversing the subtraction order, and turns the difference diffraction pattern into a Down-Up pattern, thus inverting the pixel values. Combining this 180° rotation with the vertical mirror line, it is clear that all diffraction reflections mirrored through the horizontal $(0h0)$ line must be inverted.

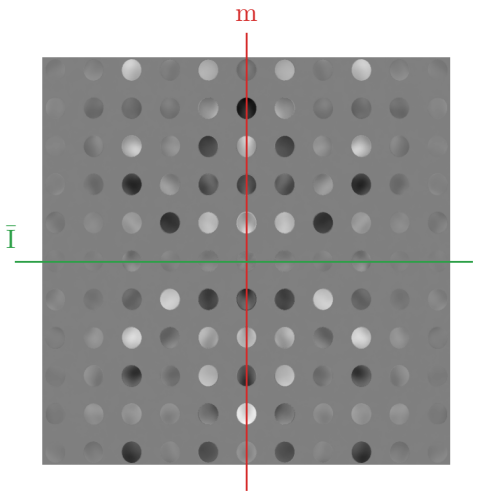


Figure 5.5: The symmetries in a simulated $\phi = 1°$ Up-Down PED pattern. The red line through the $(00l)$ reflections is a mirror line, and the green line through the $(0h0)$ reflections is an inversion line.

Both the CBED and PED simulations have the $ErMnO_3$ unit cell perfectly aligned on the $[2\bar{1}\bar{1}0]$, while experimentally the unit cell will in practice never be exactly on zone over the selected area, breaking the symmetries. The vertical line though $(00l)$ and the horizontal line through $(0h0)$ will therefore not be perfect mirror and inversion lines. Still, the experimental difference of VSADs for the 1° precession angle (Figure 4.20(b) and Figure 4.21(b)) approximately feature these symmetries.

By visually comparing the CBED, the $\phi = 0.5°$ PED, and the $\phi = 1°$ PED simulations to their experimental counterparts (Figure 4.20-4.23), the $\phi = 1°$ simulations appears to match best with experiment. The $\phi = 1°$ simulation gives a definitive answer (a single value has the highest NCC score) both in terms of polarization direction and sample thickness for both the 10 ms (Figure 4.20) and 100 ms (Figure 4.21) datasets. While for the CBED, and the $\phi = 0.5°$ PED simulations, the determined thickness and polarization direction are less conclusive. For the $\phi = 0.5°$ dataset (Figure 4.22), the highest NCC score was found for the Down-Up simulation at a thickness of 96 nm, however, the Down-Up simulation at a thickness of 25 nm had nearly as high NCC score. For the CBED simulation (Figure 4.23), the NCC score oscillates, and although the Up-Down simulation at a thickness of 59 nm had the highest NCC score, there were two other thicknesses (90 nm and 125 nm) for the Up-Down simulation that had nearly as high NCC score. The NCC score for these two can

therefore not really be used to make any conclusions about the polarization direction or sample thickness.

The high resolution HAADF-STEM image (Figure 4.24) and EELS thickness map (Figure 4.25) serve as a ground truth to what the simulations should find, namely that the Up-Down simulation at a thickness around 66 nm (±20%) should have the highest NCC score. For the $\phi = 1°$ simulation analyses, the results agree fairly well with the ground truth. For the $\phi = 0.5°$, however, the polarization direction and thickness are wrongly determined. Considering only the Up-Down $\phi = 0.5°$ simulation, the thickness is actually determined more or less correctly with a peak at 56 nm. And in the expected range of thicknesses between 40 nm and 80 nm, the Up-Down simulation has a higher NCC score than the Down-Up simulation, meaning that polarization direction is found correctly in this range. This shows that the $\phi = 0.5°$ simulation is still useful with certain limitations.

The NCC score is used to quantify similarity between the simulated and experimental difference diffraction patterns, however, it is by no means intelligent and can give misleading results. When there is a fair amount of intensity throughout the entire image, like for the $\phi = 1°$ Up-Down PED simulation (Figure 4.20 and Figure 4.21), the score works reasonably well for describing image similarity. But for the CBED (Figure 4.23) and the $\phi = 0.5°$ PED (Figure 4.22) simulations, there is substantially more intensity in the (00±2) reflections compared to the rest of the image. These two reflections therefore dominate the NCC score, allowing fairly high NCC scores even though the rest of the images are not particularly similar. This explains why the CBED and $\phi = 0.5°$ simulation analyzes gave unreliable results.

Between the two $\phi = 1°$ SPED datasets with 10 ms and 100 ms exposure times, the determined specimen thickness was found to be slightly different at 71 nm and 66 nm, respectively. This discrepancy is hard to explain as the two VSA apertures were placed in approximately the same position for both datasets, and increasing the exposure time should not alter the relative intensities between diffraction reflections, only the total counts. Thus, although the counts in the dataset with 100 ms exposure time on average are 10× higher than in the 10 ms exposure time dataset, the NCC score, which is indifferent to normalization, should be about the same. A possible explanation for the discrepancy in determined thickness is that the two datasets were captured in separate TEM sessions, meaning that experimental parameters such as sample tilt might be slightly different. To further investigate this, two new SPED datasets should be captured right after each other, with exposure time being the only parameter changed between the scans.

### 5.5.3 Simulating PED For Other Crystal Orientations

The PED simulations in this thesis were limited to the $[2\bar{1}\bar{1}0]$ zone axis. This was the reference orientation for grain $f$ where HAADF-STEM could be used to verify the polarization direction (see Figure 4.24). In Figure 4.16 however, ferroelectric domain contrast is observed for a range of different crystallographic orientations, not just the $[2\bar{1}\bar{1}0]$ zone axis. Although the ferroelectric domain contrast of grain $f$ in Figure 4.16 (which is in the $[2\bar{1}\bar{1}0]$ zone axis) can be explained from the PED simulations allowing determination of the polarization direction, explaining the ferroelectric domain contrast and finding the polarization direction for the other grains in Figure 4.16 would be of interest, but the arbitrary grain orientations make this challenging.

As mentioned in section 3.4, Pyms only accepts orthorhombic unit cells, and only allows simulations along the $c$-axis of that orthorhombic unit cell. Simulating $ErMnO_3$, which does not have an orthorhombic unit cell, therefore required a recasting to an orthorhombic unit cell. For the $[2\bar{1}\bar{1}0]$ zone axis, this recasting was done with JEMS [50] which worked well,

and resulted in a length of the $c$-axis in the new unit cell (which is the thickness resolution for the simulations) of 0.60 nm. However, recasting to an arbitrary crystal orientation would result in a very large orthorhombic unit cell to preserve continuity at the boundaries. This would be problematic for the Pyms multislice simulation because after rounding to a whole number times the length of the $c$-axis, the simulation thickness could only be increased in large steps.

The reason Pyms only accepts orthorhombic unit cells is because of the utilization of the fast Fourier transform in the implementation of the multislice solution (Equation 2.36). And the fast Fourier transform is much easier to implement for rectangular shapes. According to Kirkland in his book *Advanced Computing in Electron Microscopy* (chapter 6.7) [33], it is technically possible to define a multidimensional Fourier transform with non-orthogonal coordinates. This would make multislice simulations with non-orthorhombic unit cells easier, but to the best of the author's knowledge, this further development is not commonly implemented in electron diffraction simulation software [26, 49, 50, 64, 65].

## 5.6 Sample and Material Specific Results

With the relatively small grain size of the polycrystalline $ErMnO_3$ specimen used in this work, the ferroelectric domain structure is quite different from what is observed in single crystals or polycrystals with larger grain sizes (e.g. Figure 2 b, c and d in Schultheiß *et al.* [13] and Figure 1 in Sandvik *et al.* [6]). While single crystals usually form vortex and stripe like domains, the formation of such structures are suppressed with the confinement of smaller grain sizes [13]. Such domain structures are not observed in this sample, consistent with the previous PFM studies. Lack of domain contrast in VDF images of certain grains where domain contrast should be observable indicates that smaller grains may be single domain.

Consistent with previous studies [5], it is found diffraction reflections from the $[2\bar{1}\bar{1}0]$ zone axis are well suited for visualizing domain structures. Previous studies have utilized conventional DF TEM imaging [5], while in this work VDF imaging from SPED was used. VDF from SPED averages out strain and thickness contrast, which improves ferroelectric domain contrast compared to conventional DF-TEM. This was also found in the project report preceding this thesis [15]. It is also found that ferroelectric domain contrast is achieved with VDF from SPED for a range of crystallographic orientations, not just the $[2\bar{1}\bar{1}0]$ zone axis. It is found that ferroelectric domain contrast generally decreases as the angle between the $c$-axis and the imaging plane increases (see Figure 4.17).

The domain walls in $ErMnO_3$ are found to be mobile, and their position can be manipulated in a controlled and fairly precise manner using a focused electron beam. The domain walls appear to be more mobile in the $c$-axis direction than the transverse direction under the influence of the electron beam. This is again consistent with previous findings [5, 62].

# Chapter 6

# Conclusion

The aim of this study was to explore crystal orientations, ferroelectric domains and domain walls in polycrystalline $ErMnO_3$ with higher spatial resolution compared to previous studies. The investigated FIB lamella contained around 30 grains, with an average grain cross-section diameter of 1.0±0.6 µm. Smaller grains at the bottom of the specimen were thinner and/or beam damaged and therefore not included in the analysis. The thickness of the FIB lamella was determined using the log ratio method in EELS to be around 66 nm.

Using a SPED dataset of the entire specimen (8.5×4.0 µm), the crystallographic orientation of grains was determined through template matching with the open-source Python library Pyxem. Based on the resulting orientation map of the limited number of studied grains (26), the crystal orientations appear to be random. Deductions about misorientation angles and angles between *c*-axes across grain boundaries were made from the orientation maps.

The reliability in terms of accuracy, precision and misindexations of the results from template matching was explored. A double-axis tilt series of 18 different tilts was used to obtain a measure for the angular accuracy of template matching. The determined orientations of the five grains imaged in the tilt series were transformed back to a reference gonio tilt. Their orientation spread post transformation was used as a measure for angular accuracy, which generally was below 0.7°, depending on the orientation. For orientations close to the [0001] zone axis, template matching was less accurate. By calculating the misorientation angle to the mean grain orientation for each grain in the SPED dataset of the entire specimen, the precision of template matching was estimated to be below around 1-2°. Pseudosymmetries were identified as causes of misindexations, and it was shown that slightly tilting the sample can resolve this specific issue.

The orientation maps and transformation to other gonio tilts were used to develop a semi-automatic method for tilting to desired zone axes. From testing 9 arbitrary zone axes, the predicted specimen tilt had an average deviation from the correct tilt value of 0.73°. This method greatly increased productivity on the TEM, and is believed to be useful for several types of TEM analyses of crystalline materials, including lattice imaging and grain boundary analyses.

Through VDF imaging, it was shown that the SPED datasets contain information about the polarization direction of ferroelectric domains within grains, which template matching based on a kinematic approximation was unable to extract. A composite VDF image showed that ferroelectric domain contrast is present for a range of different crystal orientations, not just the $[2\bar{1}\bar{1}0]$ zone axis, which is the most used orientation for analyzing polarization in hexagonal manganites based on high resolution HAADF-STEM imaging. Ferroelectric domain contrast in VDF images was systematically investigated by tilting the specimen

from the $[2\bar{1}\bar{1}0]$ zone axis to the [0001] zone axis and capturing nine SPED datasets (in four different grains) from different zone axes, using the semi-automatic sample tilt method developed in this thesis. VDF images were generated from all diffraction discs in the nine datasets, and for those where ferroelectric domain contrast was observed, the contrast was quantified by calculating the Michelson contrast. It was found that ferroelectric domain contrast generally decreases as the angle between the $c$-axis and the imaging plane increases. For angles above around 72°, no domain contrast was found.

Multislice CBED and PED pattern simulations of $ErMnO_3$ in the $[2\bar{1}\bar{1}0]$ zone axis were performed to gain further insight into the ferroelectric domain contrast observed in VDF images. These simulations were compared to experimental SPED with $\phi = 0.5°$ and 1°, and SED data of a grain on the same zone axis and used to find the absolute polarization direction of the ferroelectric domains within the investigated grain. The 1° simulations matched best with experiment, and the found polarization direction of domains based on simulations was confirmed by high resolution HAADF-STEM imaging. The simulations could also be used to estimate specimen thickness, the results of which were similar to the thickness measurements with EELS.

SPED thus show great potential as a method for investigating $ErMnO_3$. This thesis presents a novel method for extracting information on the orientation and polarization of ferroelectric domains within grains, beyond what is generally used in published TEM studies of $ErMnO_3$. The variety of information gained from SPED datasets open for a wide range of further research as we continue to work towards novel, domain wall-based electronic devices.

# Chapter 7

# Further Work

The field of charged domain walls in polycrystals is still new and a lot of work, both on the fundamental physics and applications side, remains before electronic devices based on charged domain walls can be realized. In this chapter, a few concrete suggestions for further work to improve understanding of these systems, as well as further developing the methods used in this thesis, are presented.

## 7.1 Material

Although polycrystals of $ErMnO_3$ exhibit interesting properties, the question of how these properties may be applied in electronic devices remains unanswered. The grain boundaries do introduce additional design parameters and degrees of freedom for devices compared to single crystals, as the confinement from grains alter the domain morphology, grain boundaries can be charged, and applied strain on polycrystals affect the domain structure [6, 13, 14]. Polycrystals are also generally easier and cheaper to fabricate than growing single crystals. However, the grain boundaries are stationary after fabrication. This could be beneficial, or problematic depending on the application, and careful consideration should be made as to what the grain boundaries have to offer and how they may be best utilized. A focus for further work should lie in how polycrystals may be synthesized with desirable features utilizing the confinement from grain boundaries without being limited by their stationary nature.

The main material specific results in this thesis showed the structure, or arrangement of atoms, in the specimen using diffraction techniques. Properties of the material are linked to the structure, and it would be interesting to measure a wider range of properties more directly with TEM. For instance, further TEM studies on polycrystalline $ErMnO_3$ could try to measure the built-in electrical fields in the material with STEM differential phase contrast (STEM-DPC) [68]. It would be interesting to study how the bound charge at grain boundaries affects the local fields and domain structure within grains. STEM-DPC is a TEM technique where the deflection of the electron beam due to the Lorentz force (electric or magnetic fields in the specimen) is measured. Like all STEM techniques, the electron beam is focused to a probe on the specimen and scanned, however, to increase the sensitivity to electromagnetic fields, a low convergence angle compared to S(P)ED (small $\alpha$, usually in low-mag mode) is used with a long camera length so that only the direct beam hits the pixelated detector. The low convergence angle makes the diffraction discs small, and the long camera length results in larger shifts on the detector, allowing smaller angular deflections from the fields in the specimen to be measured. STEM-DPC has successfully been used to study ferroelectric materials [69]. In the ferroelectric STEM-DPC studies, the electric

polarization of the studied materials have been substantially higher ($\sim 5\times$) than in $ErMnO_3$, resulting in larger electron deflections than what can be expected in $ErMnO_3$. Attempts were made to use STEM-DPC in this thesis to directly link the determined polar $c$-axis to ferroelectric polarization. Unfortunately, the shift of the direct beam from electric fields was not observable in this specific experimental setup (Low mag mode, 256×256 pixelated direct electron detector). A more parallel beam (even lower $\alpha$) and a detector with more pixels could improve sensitivity to the weak DPC signal. Further STEM-DPC studies on $ErMnO_3$ could use a thicker sample to have a larger volume where the electric field in the material can influence the imaging electrons. Alternatively, the acceleration voltage could be reduced to 60 or 80 kV as this makes the sample appear thicker to the electron beam [70].

The effects of stain in $ErMnO_3$ could also be investigated further. As mentioned, strain has an influence on the size and morphology of ferroelectric domains in $ErMnO_3$ [6, 13]. Strain can be measured in TEM samples by calculating the relative shift of diffraction reflections. For instance if the unit cell is elongated along the $c$-axis, then the diffraction reflections would be closer spaced in this direction. These shifts can for instance be mapped out with S(P)ED. Strain analysis was attempted on the investigated lamella, but no significant relative shift of diffraction reflections was detected. This could be an indication that there is no significant strain, or that the detector has a too low sensitivity to perform the analysis necessary.

Understanding and controlling domain wall dynamics will be important for future applications in devices. In this work, it was observed that domain walls could be moved by the electron beam, which is consistent with previous findings [62, 63]. Pinned domain walls were also observed. Further studies could try to further understand domain wall movement and identify causes of domain wall pinning. The latter could perhaps be achieved by high resolution HAADF-STEM imaging of the pinning positions.

## 7.2 Methods

Several of the methods used and developed in this work could be useful for a range of different studies and should be developed further.

Although template matching works well (i.e. fast and with a decent angular accuracy), the procedure can still be improved. A drastic improvement to the method would be to implement a refinement procedure on the determined orientations. As discussed in subsection 5.2.3, refinement routines exist for orientation mapping by pattern matching on EBSD data (for instance with Kikuchipy [54]), where the correlation score is iteratively maximized by simulating orientations close to the initially determined orientation. Implementing this for template matching on SPED could potentially solve problems related to pseudosymmetries, as well as improve the angular accuracy of the determined orientations. If dynamical simulations are included in the refinement procedure, the manual VDF imaging done in this thesis (to find polarization directions of domains) could be automated. The refinement procedure is in principle easy to implement, and would require sampling orientations that are symmetrically equivalent to the initially determined orientation in the Laue group symmetry (but not equivalent in the non-centrosymmetric crystal point group), followed by dynamical simulations and calculating correlation scores. The challenge will lie in writing efficient code that can do dynamical refinements in a reasonable timeframe. As a workaround, until such refinement routines are developed, grains may be tilted to the $[2\bar{1}\bar{1}0]$ zone axis using the semi-automatic procedure presented in subsection 4.2.5, after which VDF imaging of SPED data with $\phi = 1^\circ$ can be compared to the dynamical PED simulations to find polarization directions. This is more labor-intensive, but a systematic way to determine the polarization

directions in polycrystalline specimens with random grain orientations.

The application of VDF imaging for visualizing domains and determining polarization direction shows that this information is in fact contained in the SPED data. As mentioned in subsection 5.4.3, only a limited part of orientation space was systematically investigated for ferroelectric domain contrast in VDF images. Furthermore, as only a single FIB specimen with relatively even thickness (see Figure 4.25) was used in this thesis, the effect of specimen thickness was not investigated experimentally. The simulations showed that thickness is a crucial parameter, and further work should try to explore these effects, for example by using a tripod polished wedge sample. This would give a more complete picture of the relationship between crystal orientations, thickness and ferroelectric domain contrast in VDF images, and could be used to further refine the dynamical PED multislice simulations.

SPED proves to be very useful for gathering large amounts of information about the studied specimen in an efficient manner. However, extracting and quantifying this information requires accurate models and tools. Template matching works well in this regard as it efficiently determines crystallographic orientations. However, the kinematic approximation largely ignores the finer details contained in the intensity of diffraction reflections. The dynamical multislice PED pattern simulations presented here are a valuable tool for gaining more information from the data and should be further developed. Firstly, the effect of the number of discretely sampled beam tilts in the simulation should be explored through a convergence test similar to was done by Own *et al.* [66]. Secondly, efforts should be made to reduce computation time. As discussed in subsection 5.5.1, this may be as simple as performing the simulations on a CUDA compatible GPU. Computation time could also be reduced by decreasing the number of iterations of the frozen phonon approximation. In the PED simulations presented in this thesis, 25 iterations of the frozen phonon approximation were used per beam tilt. This is the standard number of iterations for CBED simulations with Pyms, but might be excessive for PED simulations. When summing the $N$ beam tilts, there would still be an averaging over multiple random frozen phonons if each individual beam tilt simulation only performed a single frozen phonon approximation iteration. In the present case, this would reduce computation time by a factor of 25. Lastly, as discussed in subsection 5.5.3, efforts should be made to make simulations of arbitrary crystal orientations easier. This may be challenging with the current constriction to orthorhombic unit cells.

The semi-automatic method for finding the required gonio tilt for target zone axes can be very useful in a range of different applications. In particular, it is useful for polycrystals with small grains, or beam sensitive materials where high electron doses can not be used to show kikuchi lines. In order to further develop this method, it must be tested on different crystal structures. Furthermore, the method should be tested in situations where the specimen can not be left in the sample holder between TEM sessions, so that the in-plane rotation of the specimen needs to be corrected for. This method holds great potential, and further developments and applications would be highly beneficial. As a start, a tutorial notebook should be added to the documentation of a suitable python library[1] (e.g. Orix or Pyxem). The tutorial notebook should preferably use test data with an FCC crystal structure to avoid the complexity of hexagonal crystal structures.

Further developments in the methods for studying $ErMnO_3$ will be crucial in understanding and exploiting material properties and ferroelectric domain walls for future electronic devices.

[1]This has been suggested by me in an issue posted to the Github page of Orix https://github.com/pyxem/orix/issues/452

# Bibliography


[1] B. Hoefflinger. *IRDS—International Roadmap for Devices and Systems, Rebooting Computing, S3S*, pages 9–17. IRDS, 06 2020.

[2] S. Stemmer and S.A. James. Two-dimensional electron gases at complex oxide interfaces. *Annual Review of Materials Research*, 44(1):151–171, 2014.

[3] D. Meier and S.M. Selbach. Ferroelectric domain walls for nanotechnology. *Nature Reviews Materials*, 7:1–17, 10 2021.

[4] P. Bednyakov, B. Sturman, T. Sluka, A. Tagantsev, and P. Yudin. Physics and applications of charged domain walls. *npj Computational Materials*, 4, 12 2018.

[5] M.G. Han, Y. Zhu, L. Wu, T. Aoki, V. Volkov, X. Wang, S.C. Chae, Y.S. Oh, and S.W. Cheong. Ferroelectric switching dynamics of topological vortex domains in a hexagonal manganite. *Advanced Materials*, 25(17):2415–2421, 2013.

[6] O.W. Sandvik, A.M. Müller, H.W. Ånes, M. Zahn, J. He, M. Fiebig, Th. Lottermoser, T. Rojac, D. Meier, and J. Schultheiß. Pressure-control of non-ferroelastic ferroelectric domains in $ErMnO_3$, 2023.

[7] A.A. Grekov, A.A. Adonin, and N.P. Protsenko. Encountering domains in SbSl. *Ferroelectrics*, 13(1):483–485, 1976.

[8] J. Seidel, L. Martin, Q. he, Q. Zhan, Y.H. Chu, A. Lubk, M. Hawkridge, P. Maksymovych, P. Yu, M. Gajek, N. Balke, S. Kalinin, S. Gemming, F. Wang, G. Catalan, J. Scott, N. Spaldin, J. Orenstein, and R. Ramesh. Conduction at domain walls in oxide multiferroics. *Nature materials*, 8:229–34, 02 2009.

[9] D. Meier, J. Seidel, A. Cano, K. Delaney, Y. Kumagai, M. Mostovoy, N. Spaldin, R. Ramesh, and M. Fiebig. Anisotropic conductance at improper ferroelectric domain walls. *Nature Materials 11, 284 (2012)*, 02 2012.

[10] K.A. Hunnestad, E.D. Roede, A.T.J. van Helvoort, and D. Meier. Characterization of ferroelectric domain walls by scanning electron microscopy. *Journal of Applied Physics*, 128(19), 11 2020. 191102.

[11] A. Mosberg, E. Roede, D. Evans, T. Holstad, E. Bourret, Z. Yan, A. Helvoort, and D. Meier. Fib lift-out of conducting ferroelectric domain walls in hexagonal manganites. *Applied Physics Letters*, 115:122901, 09 2019.

[12] J. Schaab, I.P. Krug, F. Nickel, D.M. Gottlob, H. Doğanay, A. Cano, M. Hentschel, Z. Yan, E. Bourret, C.M. Schneider, R. Ramesh, and D. Meier. Imaging and characterization of conducting ferroelectric domain walls by photoemission electron microscopy. *Applied Physics Letters*, 104(23), 06 2014. 232904.

[13] J. Schultheiß, F. Xue, E. Roede, H.W. Ånes, F.H. Danmo, S.M. Selbach, L. Chen, and D. Meier. Confinement-driven inverse domain scaling in polycrystalline $ErMnO_3$. *Advanced Materials*, 34(45):2203449, 2022.

[14] K.A. Hunnestad, J. Schultheiß, A.C. Mathisen, C. Hatzoglou, A.T.J. van Helvoort, and D. Meier. Quantitative 3D mapping of chemical defects at charged grain boundaries in a ferroelectric oxide, 2022.

[15] A.C. Mathisen. Invesitgations of polycrystalline ferroelectric $ErMnO_3$ by TEM. Project report in TFY4520 nanoteknologi fordypningsprosjekt, Department of Physics, NTNU – Norwegian University of Science and Technology, Dec. 2022.

[16] C. Kittel. *Introduction to Solid State Physics*. Wiley, 8 edition, 2004.

[17] D. Rowenhorst, A.D. Rollett, G. Rohrer, M. Groeber, M. Jackson, P. Konijnenberg, and M. Graef. Consistent representations of and conversions between 3D rotations. *Modelling and Simulation in Materials Science and Engineering*, 23, 12 2015.

[18] IUCr. *International Tables for Crystallography, Volume A: Space Group Symmetry*. International Tables for Crystallography. Kluwer Academic Publishers, Dordrecht, Boston, London, 5. revised edition edition, 2002.

[19] O. Engler and V. Randle. *Introduction to Texture Analysis: Macrotexture, Microtexture, and Orientation Mapping, Second Edition*. CRC Press, 2009.

[20] C. Esling, E. Ferry, and H. Bunge. Three-dimensional texture analysis after Bunge and Roe: Correspondence between the respective mathematical techniques. *Textures and Microstructures*, 5, 07 1982.

[21] H.W. Ånes, B. Martineau, P. Harrison, P. Crout, D. Johnstone, N. Cautaerts, A. Gerlt, S. Høgås, and A. Clausen. pyxem/orix: orix 0.10.2, October 2022.

[22] D.N. Johnstone, B.H. Martineau, P. Crout, P.A. Midgley, and A.S. Eggeman. Density-based clustering of crystal (mis)orientations and the orix python library. *Journal of Applied Crystallography*, 53(5):1293–1298, Oct 2020.

[23] F. Bachmann, R. Hielscher, and H. Schaeben. Texture Analysis with MTEX–Free and Open Source Software Toolbox. *Solid State Phenomena*, 160, 02 2010.

[24] D.B. Williams and C.B. Carter. *Transmission Electron Microscopy: A Textbook for Materials Science*. Number v. 1 in Cambridge library collection. Springer, 2009.

[25] L. Qing, M. Qing-Chang, and H. Bande. Calculation of tilt angles for crystal specimen orientation adjustment using double-tilt and tilt-rotate holders. *Micron and Microscopica Acta*, 20(3):255–259, 1989.

[26] Y. Seto and M. Ohtsuka. ReciPro: free and open-source multipurpose crystallographic software integrating a crystal model database and viewer, diffraction and microscopy simulators, and diffraction data analysis tools. *Journal of Applied Crystallography*, 55(2):397–410, Apr 2022.

[27] P.D. Nellist and S.J. Pennycook. The principles and interpretation of annular dark-field Z-contrast imaging. volume 113 of *Advances in Imaging and Electron Physics*, pages 147–203. Elsevier, 2000.

[28] R. Vincent and P.A. Midgley. Double conical beam-rocking system for measurement of integrated electron diffraction intensities. *Ultramicroscopy*, 53(3):271–282, 1994.

[29] P. Midgley and A. Eggeman. Precession electron diffraction - A topical review. *IUCrJ*, 2:126–36, 01 2015.

[30] J.S. Barnard, D.N. Johnstone, and P.A. Midgley. High-resolution scanning precession electron diffraction: Alignment and spatial resolution. *Ultramicroscopy*, 174:79–88, 2017.

[31] R.F. Egerton. *Electron Energy-Loss Spectroscopy in the Electron Microscope*. SpringerLink : Bücher. Springer US, 2011.

[32] K. Iakoubovskii, K. Mitsuishi, Y. Nakayama, and K. Furuya. Thickness measurements with electron energy loss spectroscopy. *Microscopy research and technique*, 71:626–31, 08 2008.

[33] J. Kirkland. *Advanced Computing in Electron Microscopy*. SpringerLink: Springer e-Books. Springer US, 2010.

[34] H. Bethe. Theorie der beugung von elektronen an kristallen. *Annalen der Physik*, 392(17):55–129, 1928.

[35] F. de la Peña, E. Prestat, V.T. Fauske, P. Burdet, J. Lähnemann, P. Jokubauskas, T. Furnival, M. Nord, T. Ostasevicius, K.E. MacArthur, D.N. Johnstone, M. Sarahan, J. Taillon, T. Aarholt, pquinn dls, V. Migunov, A. Eljarrat, J. Caron, C. Francis, T. Nemoto, T. Poon, S. Mazzucco, actions user, N. Tappy, N. Cautaerts, S. Somnath, T. Slater, M. Walls, F. Winkler, and H.W. Ånes. hyperspy/hyperspy: Release v1.7.3, October 2022.

[36] D.N. Johnstone, P. Crout, M. Nord, J. Laulainen, S. Hogaas, E. Opheim, B. Martineau, T. Bergh, C. Francis, S. Smeets, E. Prestat, A. ross1, S. Collins, I. Hjorth, Mohsen, T. Furnival, D. Jannis, E. Jacobsen, A. Herzing, H.W. Ånes, J. Morzy, T. Doherty, affaniqbal, T. Ostasevicius, mvonlany, T. Tovey, and T. Poon. pyxem/pyxem: pyxem 0.12.2, October 2020.

[37] N. Cautaerts, P. Crout, H.W. Ånes, E. Prestat, J. Jeong, G. Dehm, and C.H. Liebscher. Free, flexible and fast: Orientation mapping using the multi-core and GPU-accelerated template matching capabilities in the python-based open source 4D-STEM analysis toolbox pyxem. *Ultramicroscopy*, page 113517, 2022.

[38] E. Peli. Contrast in complex images. *J. Opt. Soc. Am. A*, 7(10):2032–2040, Oct 1990.

[39] E.F. Rauch and M. Veron. Coupled microstructural observations and local texture measurements with an automated crystallographic orientation mapping tool attached to a tem. *Materialwissenschaft und Werkstofftechnik*, 36(10):552–556, 2005.

[40] M. Li, H. Tan, and W. Duan. Hexagonal rare-earth manganites and ferrites: a review of improper ferroelectricity, magnetoelectric coupling, and unusual domain walls. *Physical Chemistry Chemical Physics*, 22:14415–14432, 2020.

[41] $ErMnO_3$ Crystal Structure: Datasheet from Pauling File Multinaries Edition – 2012 in SpringerMaterials (https://materials.springer.com/isp/crystallographic/docs/sd_1502735). Copyright

2016 Springer-Verlag Berlin Heidelberg & Material Phases Data System (MPDS), Switzerland & National Institute for Materials Science (NIMS), Japan. Part of SpringerMaterials, accessed 2022-12-06.

[42] H.L. Yakel, W.C. Koehler, E.F. Bertaut, and E.F. Forrat. On the crystal structure of the manganese(III) trioxides of the heavy lanthanides and yttrium. *Acta Crystallographica*, 16(10):957–962, Oct 1963.

[43] C.M. Fernandez-Posada, C.R.S. Haines, D.M. Evans, Z. Yan, E. Bourret, D. Meier, and M.A. Carpenter. Magnetoelastic properties of multiferroic hexagonal $ErMnO_3$. *Journal of Magnetism and Magnetic Materials*, 554:169277, 2022.

[44] A. Kalashnikova and R. Pisarev. Electronic structure of hexagonal rare-earth manganites $RMnO_3$. *Jetp Letters - JETP LETT-ENGL TR*, 78:143–147, 08 2003.

[45] S. Skjærvø, E. Wefring, S. Nesdal, N. Gaukås, G. Olsen, J. Glaum, T. Tybell, and S. Selbach. Interstitial oxygen as a source of p-type conductivity in hexagonal manganites. *Nature Communications*, 7:13745, 12 2016.

[46] M.E. Holtz, K. Shapovalov, J.A. Mundy, C.S. Chang, Z. Yan, E. Bourret, D.A. Muller, D. Meier, and A. Cano. Topological defects in hexagonal manganites: Inner structure and emergent electrostatics. *Nano Letters*, 17(10):5883–5890, 2017. PMID: 28872318.

[47] J. Mundy, J. Schaab, Y. Kumagai, A. Cano, M. Stengel, I. Krug, D. Gottlob, H. Gökdemir, M. Holtz, R. Held, Z. Yan, E. Bourret, C. Schneider, D. Schlom, D. Muller, R. Ramesh, N. Spaldin, and D. Meier. Functional electronic inversion layers at ferroelectric domain walls. *Nature Materials*, 16, 03 2017.

[48] M. Tomczyk, A.M. Senos, P.M. Vilarinho, and I.M. Reaney. Origin of microcracking in $YMnO_3$ ceramics. *Scripta Materialia*, 66(5):288–291, 2012.

[49] H.G. Brown and T. Aarholt. Hamishgbrown/pymultislice: For publication with measureice. Dec 2021.

[50] P. A. Stadelmann. Jems- ems java version, 2004.

[51] P. Virtanen, R. Gommers, T.E. Oliphant, M. Haberland, T. Reddy, D. Cournapeau, E. Burovski, P. Peterson, W. Weckesser, J. Bright, S.J. van der Walt, M. Brett, J. Wilson, K.J. Millman, N. Mayorov, A.R.J. Nelson, E. Jones, R. Kern, E. Larson, C.J. Carey, I. Polat, Y. Feng, E.W. Moore, J. VanderPlas, D. Laxalde, J. Perktold, R. Cimrman, I. Henriksen, E.A. Quintero, C.R. Harris, A.M. Archibald, A.H. Ribeiro, F. Pedregosa, P. van Mulbregt, and SciPy 1.0 Contributors. SciPy 1.0: Fundamental Algorithms for Scientific Computing in Python. *Nature Methods*, 17:261–272, 2020.

[52] L. Clément, R. Pantel, L.F.Tz. Kwakman, and J.L. Rouvière. Strain measurements by convergent-beam electron diffraction: The importance of stress relaxation in lamella preparations. *Applied Physics Letters*, 85(4):651–653, 07 2004.

[53] H. Ånes, A. Helvoort, and K. Marthinsen. In-situ observations of dislocation recovery and low angle boundary formation in deformed aluminium. *Journal of Physics Conference Series*, 1270:012010, 08 2019.

[54] H.W. Ånes, L. Lervik, O. Natlandsmyr, T. Bergh, Z. Xu, E. Prestat, and M. Nord. pyxem/kikuchipy: kikuchipy 0.7.0, October 2022.

[55] S. Zaefferer. A critical review of orientation microscopy in sem and tem. *Crystal Research and Technology*, 46(6):607–628, 2011.

[56] G. Nordahl, L. Jones, E.F. Christiansen, K.A. Hunnestad, and M. Nord. Correcting for probe wandering by precession path segmentation. *Ultramicroscopy*, 248:113715, 2023.

[57] A. Morawiec, E. Bouzy, H. Paul, and J.J. Fundenberger. Orientation precision of tem-based orientation mapping techniques. *Ultramicroscopy*, 136:107–118, 2014.

[58] B. Wang. *Development of rotation electron diffraction as a fully automated and accurate method for structure determination.* PhD thesis, Stockholm University, Department of Materials and Environmental Chemistry (MMK), 2019. At the time of the doctoral defense, the following papers were unpublished and had a status as follows: Paper 2: Submitted. Paper 4: Manuscript. Paper 5: Manuscript.

[59] G. Nolze, A. Winkelmann, and A.P. Boyle. Pattern matching approach to pseudosymmetry problems in electron backscatter diffraction. *Ultramicroscopy*, 160:146–154, 2016.

[60] R. Krakow, R.J. Bennett, D.N. Johnstone, Z. Vukmanovic, W. Solano-Alvarez, S.J. Lainé, J.F. Einsle, P.A. Midgley, C.M.F. Rae, and R. Hielscher. On three-dimensional misorientation spaces. *Proceedings of the Royal Society A: Mathematical, Physical and Engineering Sciences*, 473(2206):20170274, 2017.

[61] J.L. Hart, S. Liu, A.C. Lang, A. Hubert, A. Zukauskas, C. Canalias, R. Beanland, A.M. Rappe, M. Arredondo, and M.L. Taheri. Electron-beam-induced ferroelectric domain behavior in the transmission electron microscope: Toward deterministic domain patterning. *Phys. Rev. B*, 94:174104, Nov 2016.

[62] Z. Chen, X. Wang, S.P. Ringer, and X. Liao. Manipulation of nanoscale domain switching using an electron beam with omnidirectional electric field distribution. *Phys. Rev. Lett.*, 117:027601, Jul 2016.

[63] E. Roede, A. Mosberg, D. Evans, E. Bourret, Z. Yan, A. Helvoort, and D. Meier. Contact-free reversible switching of improper ferroelectric domains by electron and ion irradiation. *APL Materials*, 9:021105, 02 2021.

[64] L. Rangel DaCosta, H.G. Brown, P.M. Pelz, A. Rakowski, N. Barber, P. O'Donovan, P. McBean, L. Jones, J. Ciston, M.C. Scott, and C. Ophus. Prismatic 2.0 – simulation software for scanning and high resolution transmission electron microscopy (STEM and HRTEM). *Micron*, 151:103141, 2021.

[65] J. Madsen and T. Susi. The abTEM code: transmission electron microscopy from first principles [version 2; peer review: 2 approved]. *Open Research Europe*, 1(24), 2021.

[66] C.S. Own, L.D. Marks, and W. Sinkler. Precession electron diffraction 1: multislice simulation. *Acta Crystallographica Section A*, 62(6):434–443, Nov 2006.

[67] A. Paszke, S. Gross, F. Massa, A. Lerer, J. Bradbury, G. Chanan, T. Killeen, Z. Lin, N. Gimelshein, L. Antiga, A. Desmaison, A. Köpf, E. Yang, Z. DeVito, M. Raison, A. Tejani, S. Chilamkurthy, B. Steiner, L. Fang, J. Bai, and S. Chintala. *PyTorch: An Imperative Style, High-Performance Deep Learning Library.* Curran Associates Inc., Red Hook, NY, USA, 2019.

[68] M. Krajnak, D. McGrouther, D. Maneuski, V. O Shea, and S. McVitie. Pixelated detectors and improved efficiency for magnetic imaging in stem differential phase contrast. *Ultramicroscopy*, 165:42–50, 2016.

[69] N. Shibata, S.D. Findlay, Y. Kohno, H. Sawada, Y. Kondo, and Y. Ikuhara. Differential phase-contrast microscopy at atomic resolution. *Nature Physics*, 8(8):611–615, August 2012.

[70] K. Moore, U. Bangert, and M. Conroy. Aberration corrected STEM techniques to investigate polarization in ferroelectric domain walls and vortices. *APL Materials*, 9(2), 02 2021. 020703.

# Appendix A

# Complementary Results

In this appendix, complementary data and details are given that support the main text. This includes SPED data with descan off, SAD patterns from selected zone axes, a conventional DF-TEM image with ferroelectric domain contrast, VDF images from Friedel pairs with inverted ferroelectric domain contrast, summed PED patterns and VDF images from the analysis in subsection 4.3.2, and an uncropped PED pattern from the $\phi = 1°$ PED simulation.

## A.1 Descan Off SPED

When SPED data is captured with descan turned off, the direct beam moves around in a circle on the detector. The radius of this circle is the precession angle, and so SPED data with descan-off can be used to measure the precession angle. In Figure A.1, two such descan-off SPED datasets are plotted for a nominal precession angle of 0.5° (a) and 1° (b). These diffraction patterns are the sum over the PED patterns in a small 11×11 probe positions scan. The circle has a certain thickness which is caused by the convergence angle of the electron beam (same reason default descan-on SPED data has diffraction discs and not points), and the precession angle is the radius to the center of this thickness. In order to representatively measure the precession ($\phi$) and convergence ($\alpha$) angles, an azimuthal integration of the image is performed using the `get_azimuthal_integral1d` function in Pyxem [36], which gives image intensity as a function of radius from the center. This is the graph plotted on top of the images in Figure A.1. Figure A.1(a) is from a scan in vacuum and so only the direct beam circle is present, while Figure A.1(b) is from a scan on the thin specimen, which is why weaker circles from diffracted beams are present in addition to the strongest direct beam circle. For the nominal precession angle of 0.5°, $\phi$ was measured to be 0.52°, and for the nominal precession angle of 1°, $\phi$ was measured to be 0.96°. $\alpha$ was measured to be 0.12° for both nominal precession angles.

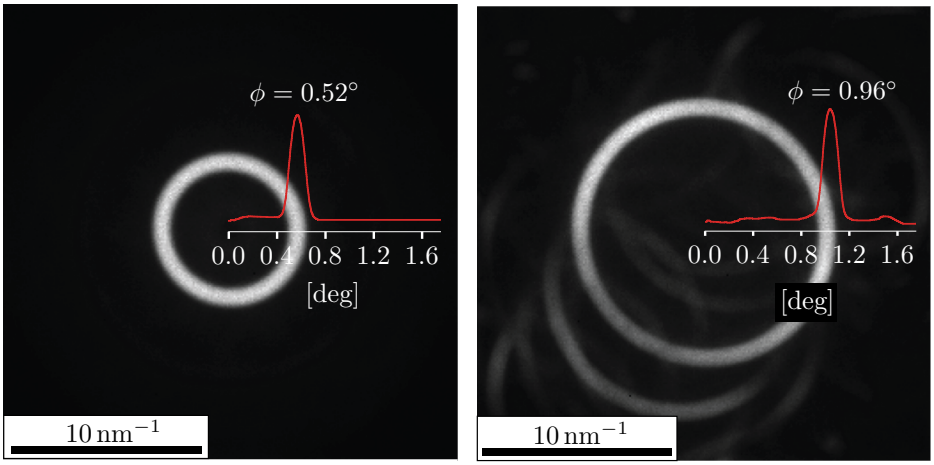


(a) (b)

Figure A.1: Summed PED patterns from SPED data with descan-off. (a) SPED data with a nominal precession angle of 0.5°. (b) SPED data with a nominal precession angle 1°. The plotted graph is intensity as a function of radius from the center, and is used to measure the precession and convergence angles. These PED patterns were captured with the same nominal camera length as the other S(P)ED datasets in this thesis.

## A.2 Verification of Predicted Gonio Tilts For Target Zone Axes

In subsection 4.2.5, a semi-automatic method for determining the sample tilt required to orient a grain in the sample to a desired zone axis was presented. This method utilized crystallographic orientations found through template matching on SPED data and the transformation in Equation 2.25. The semi-automatic method was tested by choosing 9 arbitrarily zone axes in 7 different grains and comparing the predicted $x$- and $y$-tilt to the actual $x$- and $y$-tilt of the zone axes (the results of which are presented in Table 4.1). The SAD patterns from these 9 zone axes are shown in Figure A.2, where the experimental $x$- and $y$-tilt is indicated in the lower left of the diffraction patterns.

## A.3 Conventional DF-TEM Domain Contrast

Figure A.3 features a conventional DF-TEM image of grain $f$ and a SAD pattern displaying the size and position of the objective aperture used to capture the DF-TEM image. The diffraction pattern in Figure A.3(a) consists of two images. The first is plotted in the white image channel, and is a normal SAD pattern with no objective aperture. The second was captured with the objective aperture centered on the (022) diffraction reflection, and is plotted in the red image channel. Although ferroelectric domain contrast is clearly visible in Figure A.3(b), there is a lot of bending and strain contrast in the image.

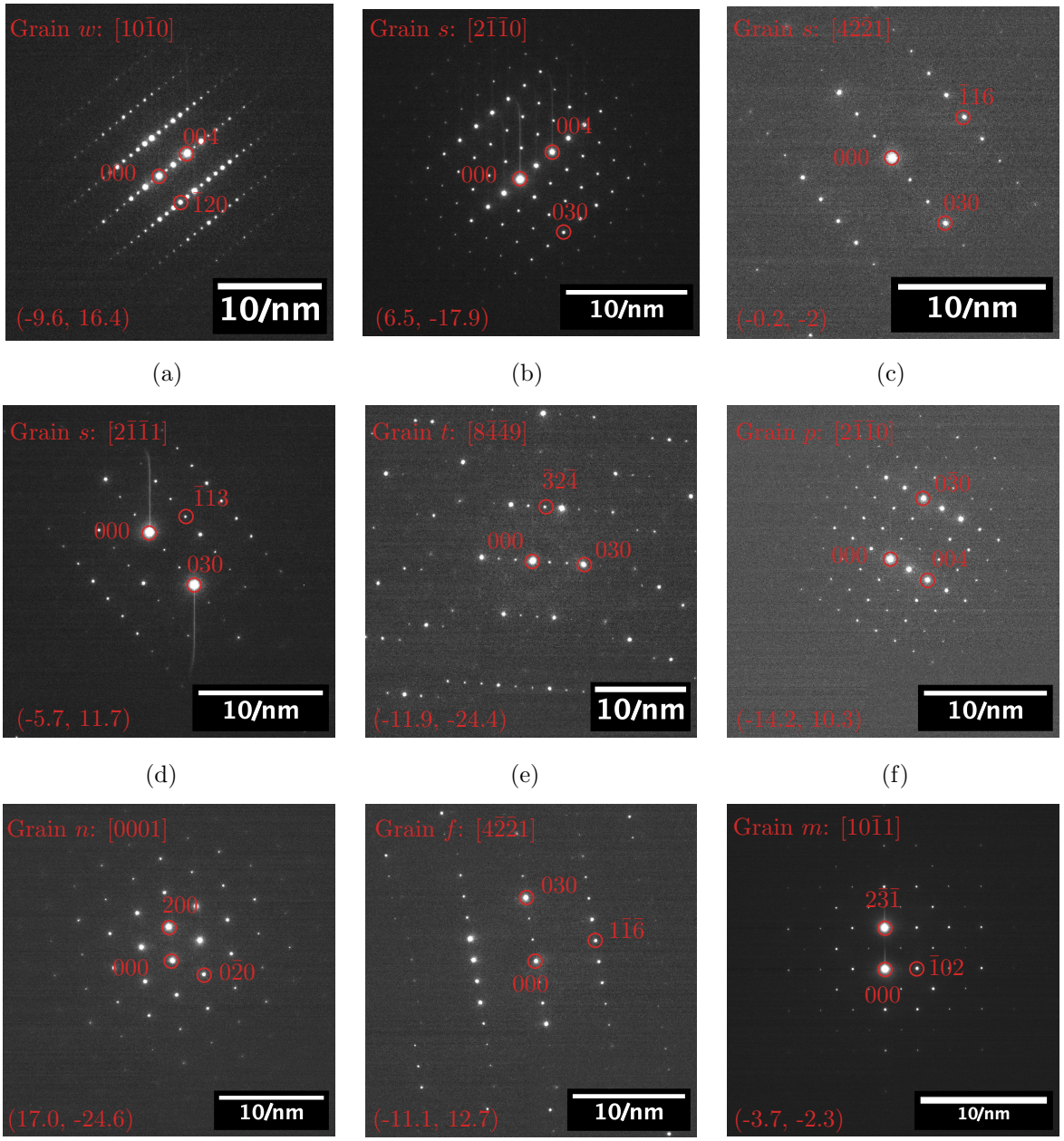


Figure A.2: SAD patterns from 9 zone axes in 7 different grains. The grain and zone axis is indicated in the top left of the images. The direct beam (000) and two diffraction reflections are marked in all diffraction patterns. In the lower left, the experimental $x$- and $y$-tilt at which each SAD pattern was captured is indicated as $(x, y)$.

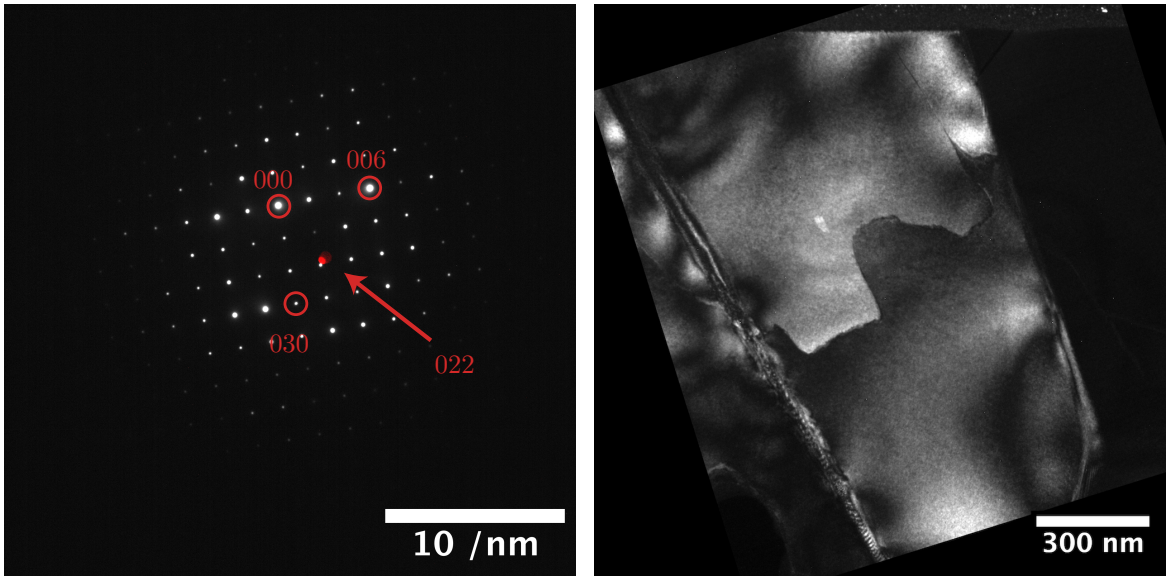


(a) (b)

Figure A.3: Ferroelectric domain contrast in conventional DF-TEM imaging. (a) SAD pattern from grain $f$ with and image of the objective aperture centered on the (022) reflection plotted on top in the red color channel. (b) DF image of grain $f$ from the (022) diffraction reflection (marked with red arrow in (a)). These images were captured on the 2100 TEM. This figure is adapted from the project report for TFY4520 [15].

## A.4 Contrast Inversion in VDF Images From Friedel Pairs

Figure A.4 illustrates how the ferroelectric domain contrast is inverted in VDF images generated from Friedel pairs in SPED datasets. The images in this figure are generated from the same SPED dataset of grain $f$ with 1° precession angle. Figure A.4(a) and (b) were generated from the $(01\bar{1}2)$ and $(0\bar{1}12)$ diffraction reflections, respectively. In subsection 4.3.2, domain contrast in VDF images is addressed further.

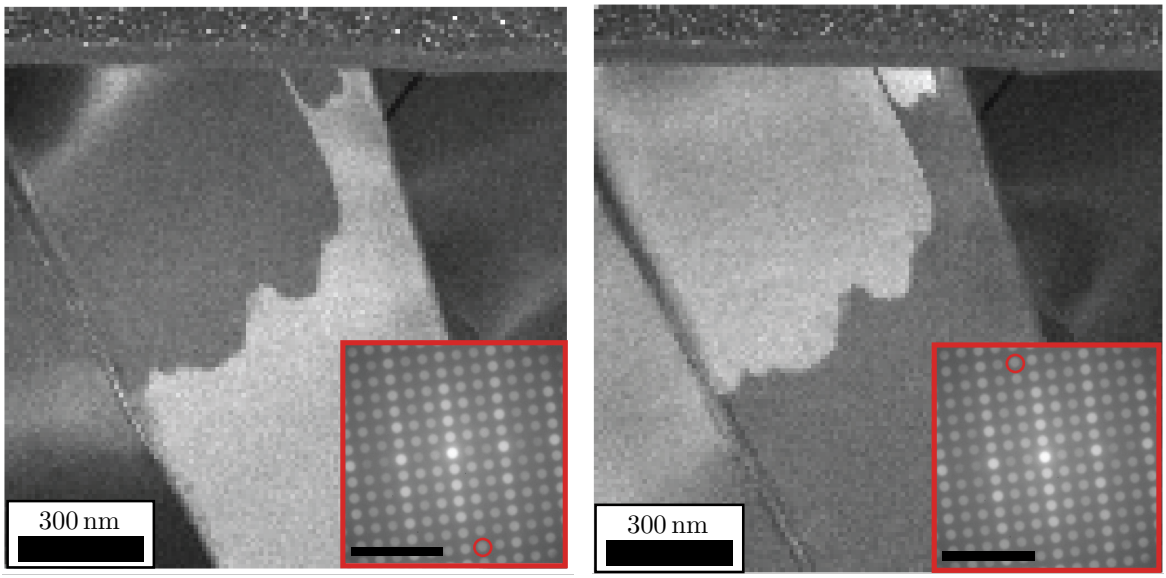


(a) (b)

Figure A.4: VDF image contrast inversion between Friedel pairs. These images are generated from the same SPED dataset with $\phi = 1°$ covering grain $f$ on the $[2\bar{1}\bar{1}0]$ zone axis. (a) VDF image generated with the $(01\bar{1}2)$ diffraction reflection. (b) VDF image generated with the $(0\bar{1}12)$ diffraction reflection. (b) is the same figure as Figure 4.15(b). The used diffraction reflection is marked with the red circle in the inserts. The scale bar in the insert is $10\,\mathrm{nm}^{-1}$ in both (a) and (b).

## A.5 VDF Image Contrast With Increasing Out-of-Plane $c$-axis

In subsection 4.3.2, a series of nine SPED datasets from zone axes between $[2\bar{1}\bar{1}0]$ and [0001] were used to explore how ferroelectric domain contrast changes as the angle between the $c$-axis and the imaging plane increases. Each of the figures in this section (Figure A.5-A.13) displays (a) summed PED patters over the specific grain, and (b) the highest domain contrast VDF images for the nine SPED datasets.

The $N$ total ($N$ is given in Table 4.2) virtual objective apertures that resulted in ferroelectric domain contrast in the VDF image are plotted as the green circles on top of the summed PED patterns in Figure A.5-A.13(a), and the red circle marks the diffraction reflection which gave the highest ferroelectric domain contrast. This is the virtual objective aperture that was used to generate the VDF image in Figure A.5-A.13(b). In the summed PED patterns in Figure A.5-A.13(a), the scale bar has been omitted to avoid obstructing the view of the virtual objective apertures. The scale of these PED patterns can be inferred from for instance Figure 4.3 as the PED patterns there were captured with the same camera length.

For Figure A.11-A.13, no ferroelectric domain contrast was found for any of the diffraction reflections. In these figures the image in (b) is therefore a VBF image, with the virtual objective aperture selecting the direct beam in the summed PED pattern (a). The contrast values (Equation 2.42) in the VDF images generated from all the virtual objective apertures in Figure A.5-A.13 are shown in Figure 4.17.

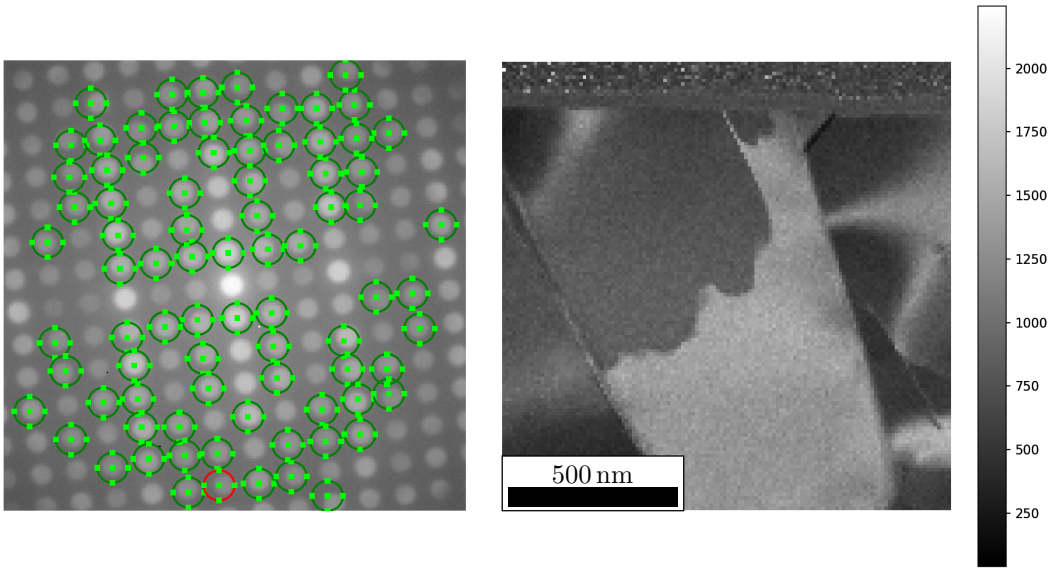


(a) (b)

Figure A.5: (a) Summed PED pattern from grain $f$ in the $[2\bar{1}\bar{1}0]$ zone axis with green circles representing the 82 total virtual objective apertures that resulted in ferroelectric domain contrast in the VDF image. The red circle is the virtual objective aperture that resulted in the highest ferroelectric domain contrast. (b) VDF image generated from the red virtual objective aperture in (a).

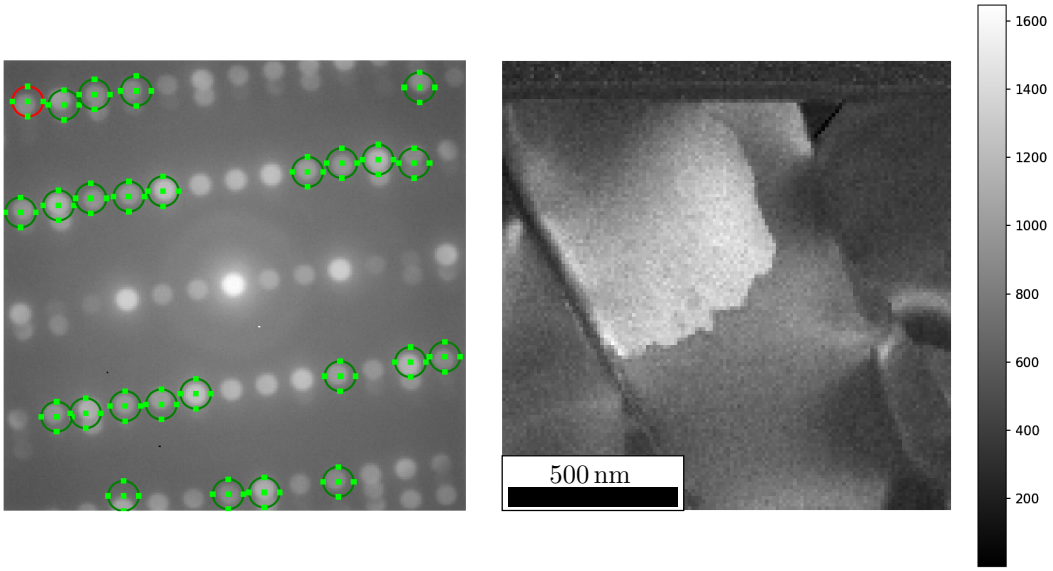


(a) (b)

Figure A.6: (a) Summed PED pattern from grain $f$ in the $[4\bar{2}\bar{2}1]$ zone axis with green circles representing the 26 total virtual objective apertures that resulted in ferroelectric domain contrast in the VDF image. The red circle is the virtual objective aperture that resulted in the highest ferroelectric domain contrast. (b) VDF image generated from the red virtual objective aperture in (a).

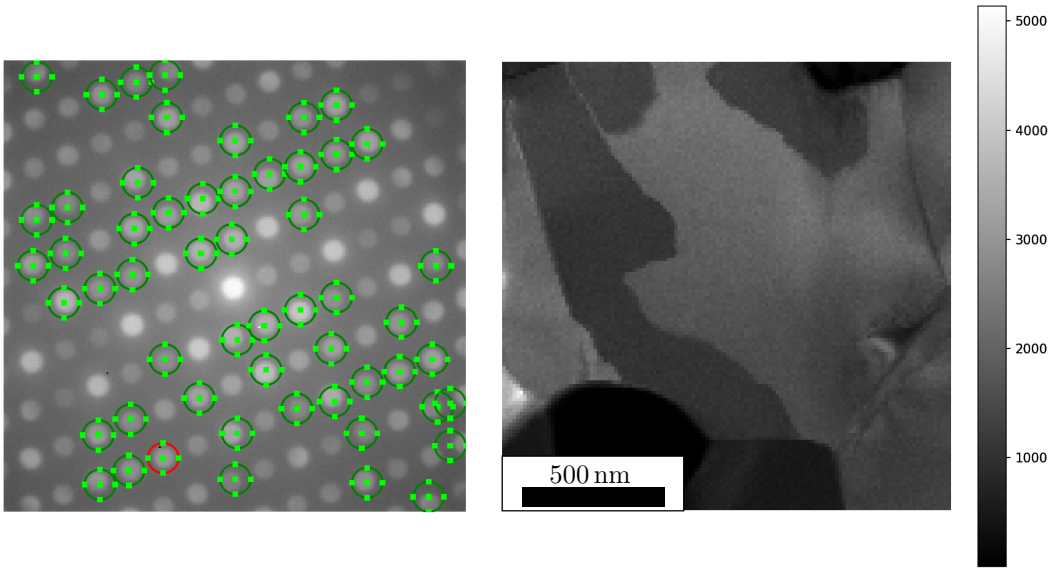


(a) (b)

Figure A.7: (a) Summed PED pattern from grain $m$ in the $[4\bar{2}\bar{2}3]$ zone axis with green circles representing the 55 total virtual objective apertures that resulted in ferroelectric domain contrast in the VDF image. The red circle is the virtual objective aperture that resulted in the highest ferroelectric domain contrast. (b) VDF image generated from the red virtual objective aperture in (a).

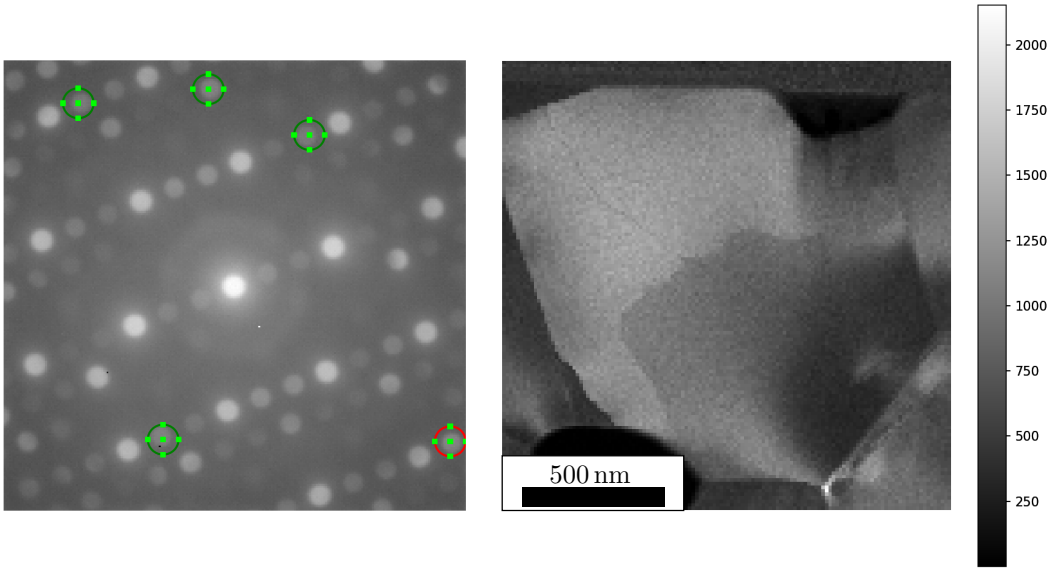


(a) (b)

Figure A.8: (a) Summed PED pattern from grain $m$ in the $[4\bar{2}\bar{2}5]$ zone axis with green circles representing the 5 total virtual objective apertures that resulted in ferroelectric domain contrast in the VDF image. The red circle is the virtual objective aperture that resulted in the highest ferroelectric domain contrast. (b) VDF image generated from the red virtual objective aperture in (a).

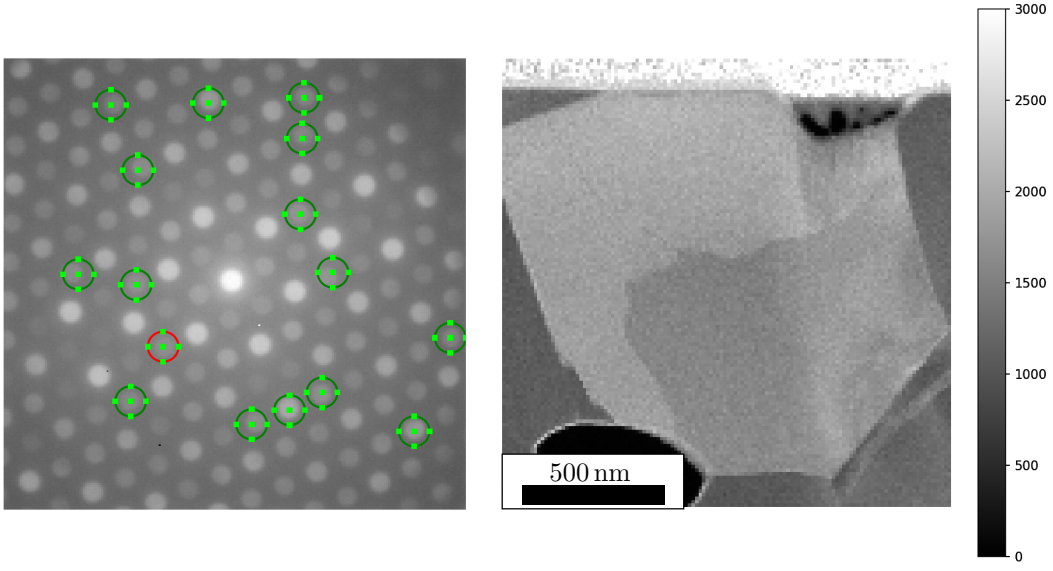


(a) (b)

Figure A.9: (a) Summed PED pattern from grain $m$ in the $[2\bar{1}\bar{1}3]$ zone axis with green circles representing the 16 total virtual objective apertures that resulted in ferroelectric domain contrast in the VDF image. The red circle is the virtual objective aperture that resulted in the highest ferroelectric domain contrast. (b) VDF image generated from the red virtual objective aperture in (a).

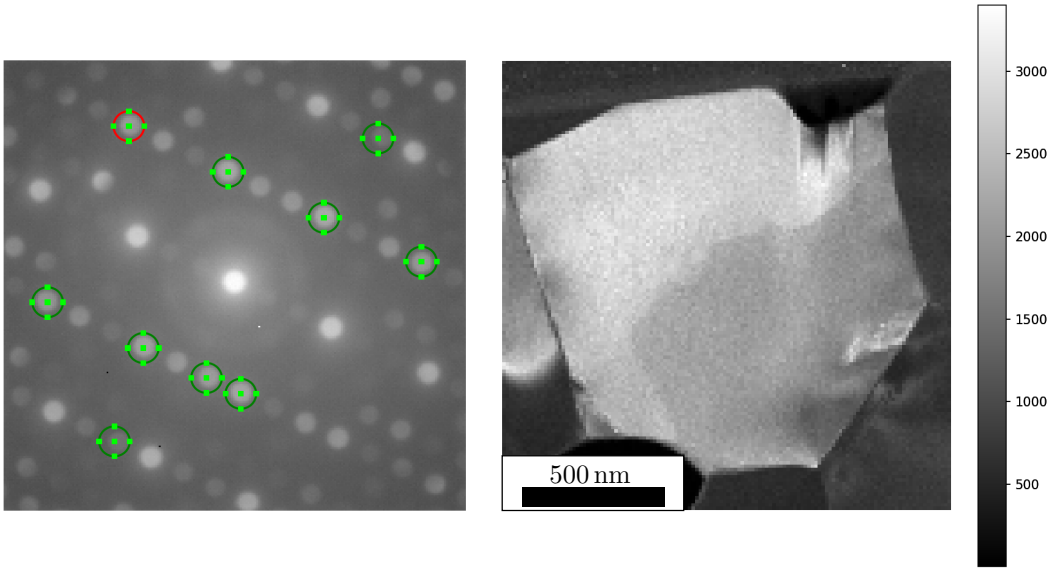


(a) (b)

Figure A.10: (a) Summed PED pattern from grain $m$ in the $[2\bar{1}\bar{1}5]$ zone axis with green circles representing the 10 total virtual objective apertures that resulted in ferroelectric domain contrast in the VDF image. The red circle is the virtual objective aperture that resulted in the highest ferroelectric domain contrast. (b) VDF image generated from the red virtual objective aperture in (a).

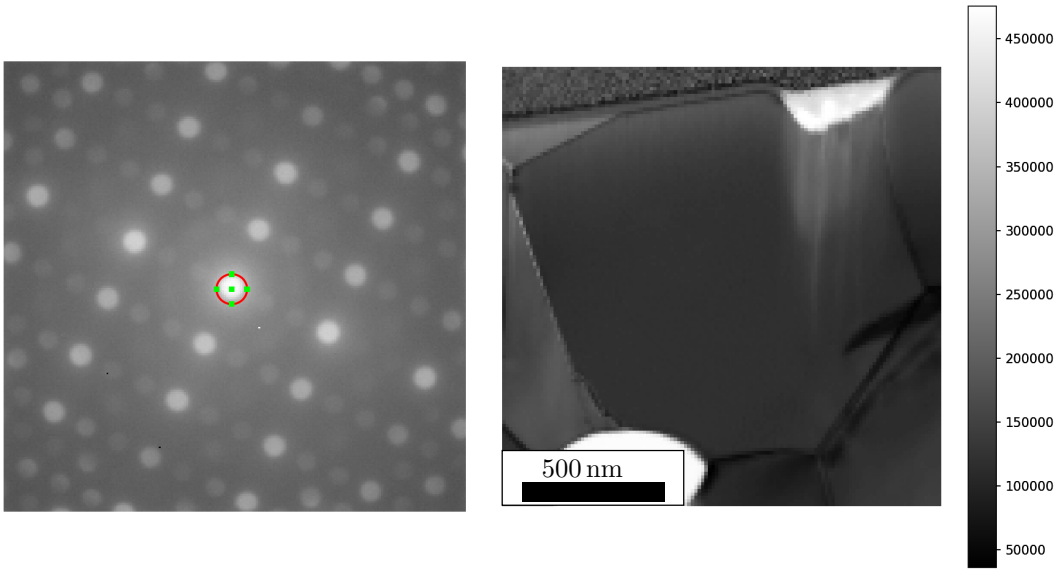


(a) (b)

Figure A.11: (a) Summed PED pattern from grain $m$ in the $[2\bar{1}\bar{1}6]$ zone axis. No ferroelectric domain contrast was observed for any of the diffraction reflections in this PED pattern. The red circle therefore marks the direct beam. (b) VBF image generated from the direct beam.

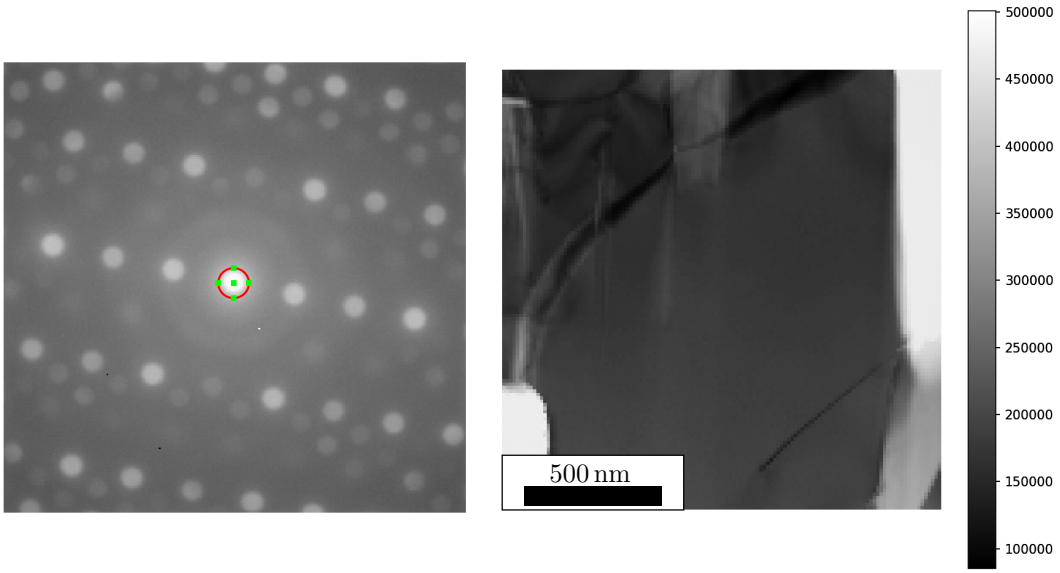


(a) (b)

Figure A.12: (a) Summed PED pattern from grain $j$ in the $[2\bar{1}\bar{1}0]$ zone axis. No ferroelectric domain contrast was observed for any of the diffraction reflections in this PED pattern. The red circle therefore marks the direct beam. (b) VBF image generated from the direct beam.

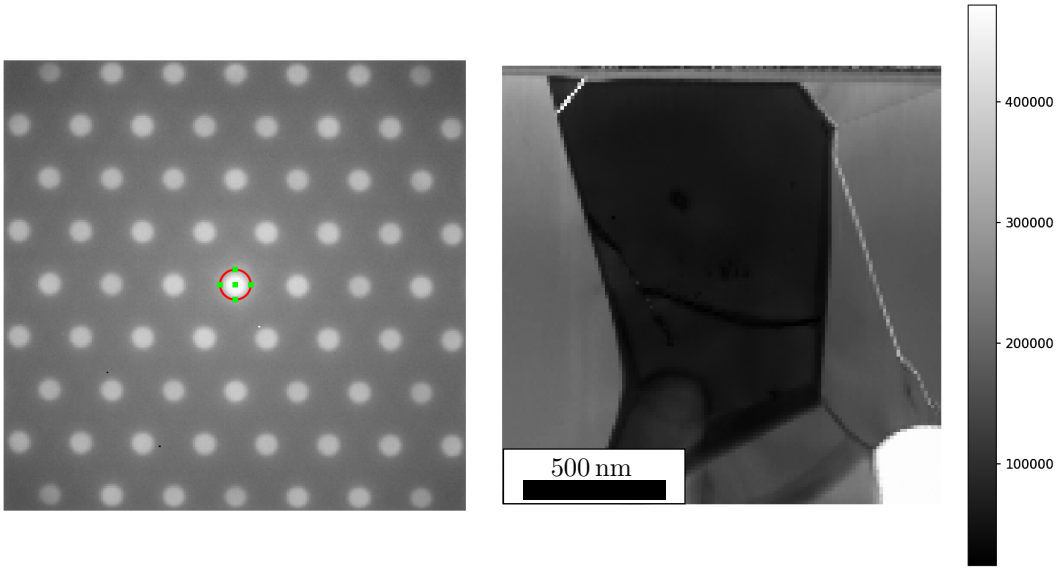


(a) (b)

Figure A.13: (a) Summed PED pattern from grain $h$ in the [0001] zone axis. No ferroelectric domain contrast was observed for any of the diffraction reflections in this PED pattern. The red circle therefore marks the direct beam. (b) VBF image generated from the direct beam.

## A.6 PED $\phi = 1°$ Simulation

In Figure 4.18(c), a cropped version of the $\phi = 1°$ PED simulation of $ErMnO_3$ in the $[2\bar{1}\bar{1}0]$ zone axis was shown. The diffraction pattern in that figure was cropped to have the same field of view as the CBED and $\phi = 0.5°$ simulations. In Figure A.14, the uncropped version of Figure 4.18(c) is shown, showing the full field of view of the simulation. The thickness for this simulation was 71 nm and the $c$-axis is pointing vertically up. The orange circle marks the (008) reflection, and the blue marks the (030) reflection. The green rectangle marks the field of view in Figure 4.18.

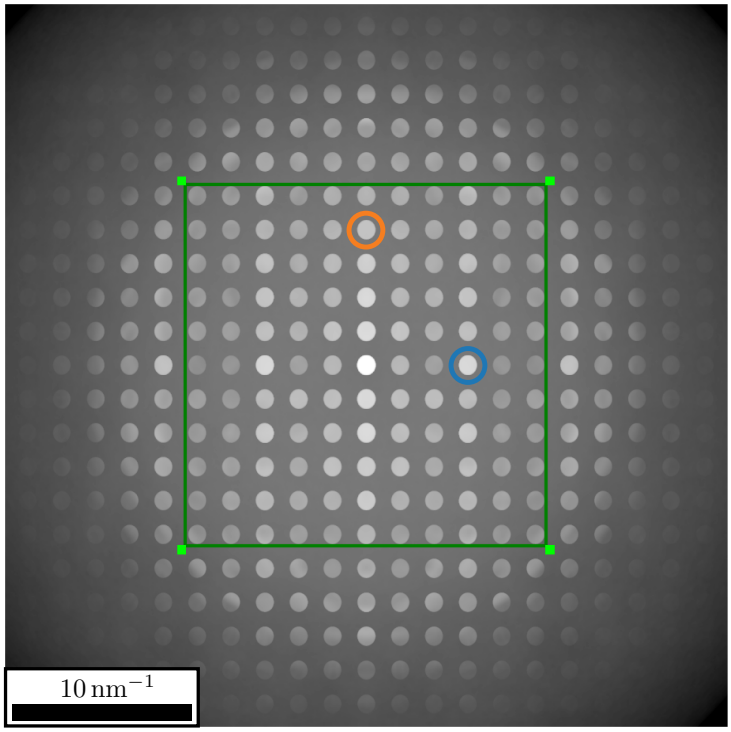


Figure A.14: Simulated PED pattern with $\phi = 1°$ of $ErMnO_3$ in the $[2\bar{1}\bar{1}0]$ zone axis at a thickness of 71 nm. The orange and blue circles mark the (008) and (030) diffraction reflections, respectively. The green rectangle marks the field of view in Figure 4.18.

# Appendix B

# Finding The Tilt Axes of a TEM

This appendix will show a method for determining the location of the tilt axes $T_1$ and $T_2$ by using two SPED tilt series and template matching. In the first tilt series, the $y$-tilt was fixed at 1.8°, and 14 samples of the $x$-tilt between -30.7° and 30.2° were chosen with approximately 5° between each point. The SPED scans were made with 128x128 probe positions, 1° precession angle at 100 Hz, and covering the five grains $f$, $g$, $h$, $i$ and $j$. Before capturing each SPED dataset in the tilt series, SPED was realigned as described in section 3.3. Because of this realignment of the SPED and subsequent repositioning of the sample, the scans are slightly shifted between tilts.

The result of the template matching done on the 14 SPED datasets is presented in Figure B.1. By examining the orientation of the different grains as the $x$-tilt increases, one can clearly see that the plotted unit cells are rotating, and the axis about which they are rotating is the $T_1$ tilt axis. From visual inspection, this axis appears to lie close to the $x$-axis of the image.

Upon close inspection of the template matching, there appears to be some grains where template matching did not work very well. For instance, grain $h$ appears to be on the [0001] zone axis in Figure B.1(e), (h) and (k). This can not be correct as these three SPED scans were captured at different tilts, which should be reflected in the determined orientations. The reason for this issue was addressed in subsection 5.2.3. Because of these problems, grain $h$ will be disregarded in the further analysis. In addition, the template matching for certain grains in certain tilts appears to have issues with pseudosymmetries (e.g. two or more unit cells plotted in the grain, for instance grain $j$ in Figure B.1(g) and (l)). To resolve these issues, the orientation most probable considering the determined orientation of the same grain in other sample tilts was chosen for further analysis.

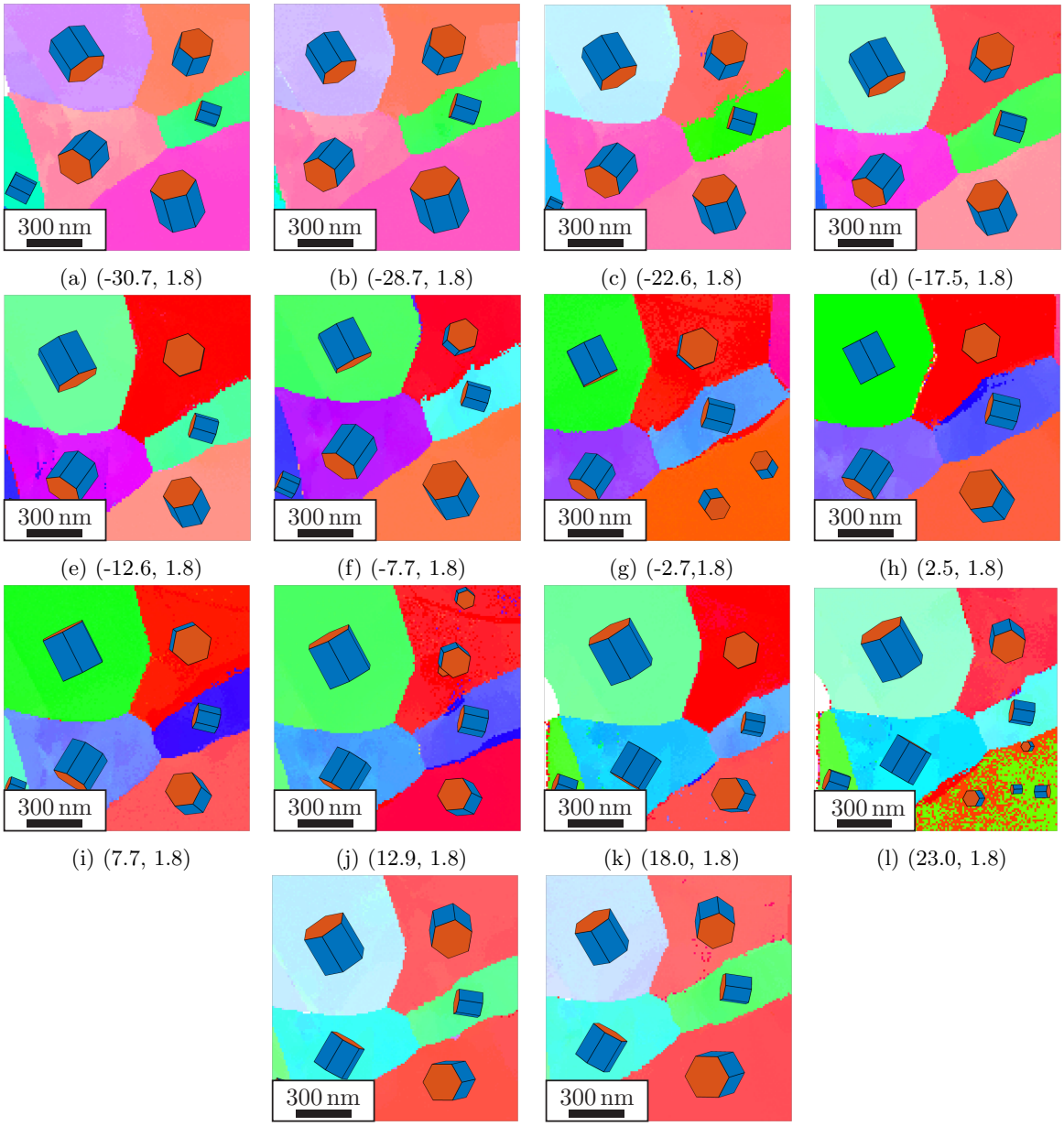


(a) (-30.7, 1.8) (b) (-28.7, 1.8) (c) (-22.6, 1.8) (d) (-17.5, 1.8)

(e) (-12.6, 1.8) (f) (-7.7, 1.8) (g) (-2.7,1.8) (h) (2.5, 1.8)

(i) (7.7, 1.8) (j) (12.9, 1.8) (k) (18.0, 1.8) (l) (23.0, 1.8)

(m) (28.1, 1.8) (n) (30.2, 1.8)

Figure B.1: Template matching results for $x$-tilt series. The $x$- and $y$-tilt for each SPED dataset are indicated in the captions as $(x, y)$.

In order to quantify the position of the $T_1$ axis, the first step is to find the mean orientation for the grains in the 14 different scans. The template matching routine finds the orientation of the crystal pixel-by-pixel, but using only a single pixel for each grain would increase the noise in the result, and so the MTEX functions `calcGrains` and `grains.meanOrientation` were used to calculate the mean orientation over all pixels in each grain. The mean orientation for grain $\gamma$ at step $i$ in the tilt series is referred to as $O_\gamma^i$. The misorientation

$$m_\gamma^{i,i+1} = (O_\gamma^i)^{-1}(O_\gamma^{i+1}) \tag{B.1}$$

describes the rotation which takes grain $\gamma$ from the orientation in step $i$ to the orientation in step $i+1$. This misorientation, in the axis-angle representation, will have $T_1$ as the

misorientation axis, and the misorientation angle will be the difference between the $x$-tilt in step $i$ and $i+1$.

In Figure B.2, the $x$-tilt predicted by the misorientation angle is plotted for the four grains. Here, the $x$-tilt of the first data point (index 0) was set to the known starting position -30.7°, and each subsequent data point is found by taking the $x$-tilt in the previous data point, and adding the misorientation angle. The $x$-tilt read of the goniometer is also plotted (the blue dashed line), and it is clear that the misorientation angle is consistent with the actual sample tilt for the four grains.

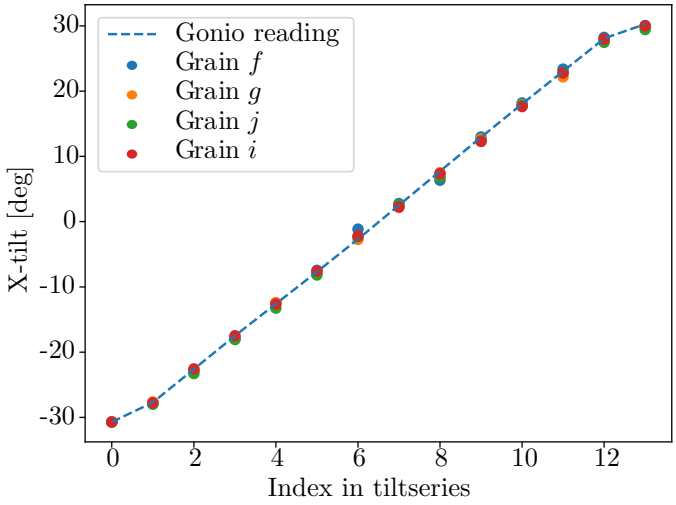


Figure B.2: $X$-tilt for the SPED datasets in the $x$-tilt series as read of the goniometer (blue dashed line), and predicted from misorientation angles.

From the 4 grains and the 14 steps in the tilt series, a total of 52 misorientations were calculated. And from this, the average misorientation axis (the $T_1$ axis) was found to lie $9.6° \pm 3.3°$ degrees rotated counterclockwise from the $x$-axis of the images in Figure B.1. The $T_2$ tilt axis ($y$-tilt) can of course for the double tilt holder be assumed to lie perpendicular to the $T_1$ tilt axis. However, a SPED $y$-tilt series of 5 tilts ranging from -18.2° to 17.5° with $x$-tilt fixed at 2.5° was captured to verify the position of the $T_2$ tilt axis. The results of template matching on those SPED scans are presented in Figure B.3. A similar misorientation analysis as was done with the $x$-tilt series found that the $T_2$ tilt axis lies a $99.4° \pm 1.4°$ counterclockwise rotation from the $x$-axis of the image. This confirms that the two tilt axes are perpendicular.

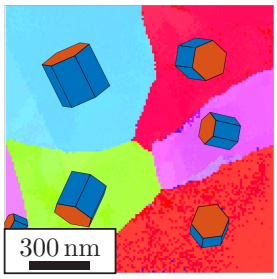


(a) (2.5, -18.2)

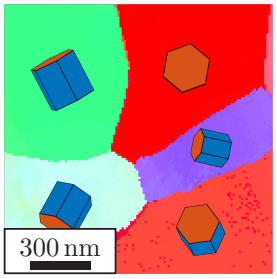


(b) (2.5, -8.2)

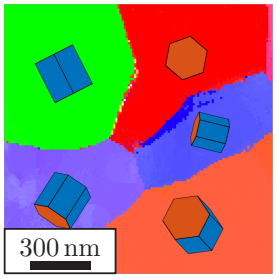


(c) (2.5, 1.8)

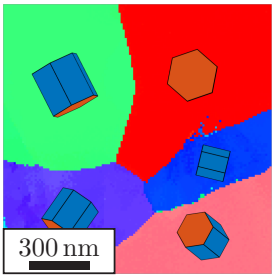


(d) (2.5, 11.8)

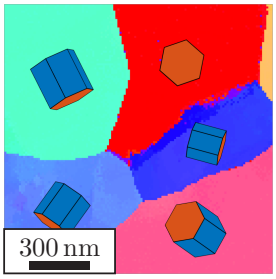


(e) (2.5, 17.5)

Figure B.3: Template matching results for $y$-tilt series. The $x$- and $y$-tilt for each SPED dataset are indicated in the captions as $(x, y)$.

The position of the $T_1$ and $T_2$ tilt axes with respect to the scan orientation is presented graphically in Figure B.4, where the plotted image is the (2.5°, 1.8°) point in the tilt series. The SPED data in both the $x$-tilt series and the $y$-tilt series were, as all the other SPED data in this thesis, captured with a scan rotation of 19°. This scan rotation was chosen to have the lamella aligned to the scan. The double tilt holder tilt axes in the TEM are of course stationary, and not affected by the scan rotation, and so their position with respect to the scan will be a linear function of scan rotation. From the analysis here, we can conclude that for a scan rotation of $\theta$, the position of the $T_1$ tilt axis will be -9.4° + $\theta$.

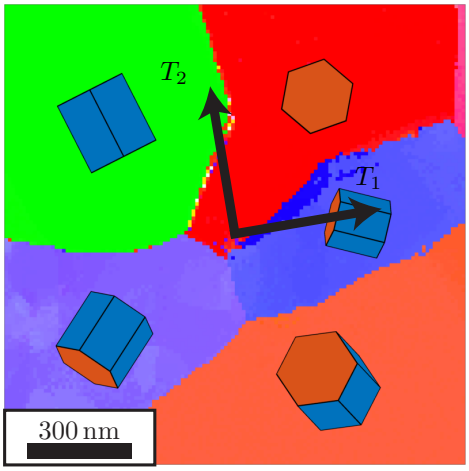


Figure B.4: The result of template matching on the SPED data set with x-tilt of 2.5° and y-tilt of 1.8° with the position of the double tilt holder tilt axes plotted on top.

# Appendix C

# Presentations of the Work

The results of this work have been presented and used in several occasions and formats. These include oral presentations given by me at internal TEM group meetings, and dedicated SPED users meetings. I also presented the work at the Gray Goo Symposium organized by TIMINI, the student organization for Nanotechnology at NTNU. The work has further contributed to a submitted manuscript and two talks. This appendix includes the abstracts for the manuscript and the two talks:

C.1: The first page of the manuscript *Quantitative mapping of chemical defects at charged grain boundaries in a ferroelectric oxide*, which I co-authored as a byproduct of the work done in this thesis (manuscript available through ArXive [14], see Bibliography above). The manuscript has been submitted to *Advanced Materials*.

C.2: The abstract for *4DSTEM for a more complete characterization of ferroelectrics*, which was given by my supervisor, Antonius van Helvoort, at the Ferroelectrics Domains and Domain Walls Workshop organized by the Department of Physics and the Department of Materials Science and Engineering (NTNU) in April 2023.

C.3: The abstract for *Scanning precession electron diffraction for structural analysis of polycrystalline ferroelectrics*, in which the work in this thesis will be presented by my supervisor, Antonius van Helvoort, on the 6$^{\text{th}}$ of July in Manchester (UK) at the MMC/EMAG 2023 conference. This conference is organized by the Institute of Physics's Electron Microscopy and Analysis Group (EMAG) in conjunction with mmc series from the Royal Microscopical Society.

# Quantitative mapping of chemical defects at charged grain boundaries in a ferroelectric oxide

K. A. Hunnestad[1], J. Schultheiß[1], A. C. Mathisen[2], I. Ushakov[1], C. Hatzoglou[1], A. T. J. van Helvoort[2], and D. Meier[1]

[1] Department of Materials Science and Engineering, Norwegian University of Science and Technology (NTNU), 7491 Trondheim, Norway

[2] Department of Physics, Norwegian University of Science and Technology (NTNU), 7491 Trondheim, Norway

KEYWORDS. Atom probe tomography, ferroelectric, grain boundaries, polar materials, impurity, polycrystalline, hexagonal manganite

**Polar discontinuities and structural changes at oxide interfaces can give rise to a large variety of electronic and ionic phenomena. Related effects have been intensively studied in epitaxial systems, including ferroelectric domain walls and interfaces in superlattices. Here, we investigate the relation between polar discontinuities and the local chemistry at grain boundaries in polycrystalline ferroelectric $ErMnO_3$. Using orientation mapping and different scanning probe microscopy techniques, we demonstrate that the polycrystalline material develops charged grain boundaries with enhanced electronic conductance. By performing atom probe tomography measurements, we find an enrichment of erbium and a depletion of oxygen at all grain boundaries. The observed compositional changes translate into a charge that exceeds possible polarization-driven effects, demonstrating that structural phenomena rather than electrostatics determine the local chemical composition and related changes in the electronic transport behavior. The study shows that the charged grain boundaries behave distinctly different from charged domain walls, giving additional opportunities for property engineering at polar oxide interfaces.**

C.2

# 4DSTEM for a more complete characterization of ferroelectrics

Ferroelectrics Domains and Domain Walls workshop, Tromsø to Trondheim 22.-25.04.2023

Speaker: Ton van Helvoort
Contributions from Anders C. Mathisen, Jan Schultheiss, Kasper A. Hunnestad, Dennis Meier, Leonardo Correa and Daniel Ugarte

Understanding and utilizing ferroelectricity takes place over different length scales. At sub-nm spatial resolution, scanning transmission electron microscopy (STEM) imaging and spectroscopy techniques have become routine. This contribution will demonstrate that scanning electron diffraction is an extremely powerful addition. Being able to collect and interpret the intense coherent scattering signal is the basis for nm-scale phase, orientation, strain and field mapping. These techniques are collected under the term *4DSTEM*. We will show that by precessing the electron beam, a more stable diffraction intensity distribution is obtained, which is highly beneficial for deducing the relevant structural characteristics of the material. This will be demonstrated in the analysis of polycrystalline ferroelectric h-ErMnO3.

# C.3

# Scanning precession electron diffraction for structural analysis of polycrystalline ferroelectrics

A. C. Mathisen[1], L. M. Côrrea[2], K. A. Hunnestad[3], J. Schultheiß[3,4], E. F. Christiansen[1], D. Meier[3], D. Ugarte[2], A. T. J. van Helvoort[1]
[1] Department of Physics, Norwegian University of Science and Technology (NTNU), Trondheim, Norway. [2] Instituto de Fisica “Gleb Wataghin”, Universidade Estadual de Campinas (UNICAMP), Campinas, Brazil. [3] Department of Materials Science and Engineering, Norwegian University of Science and Technology (NTNU), Trondheim, Norway. [4] Experimental Physics V, University of Augsburg, Augsburg, Germany

Abstract Text

In this contribution we will demonstrate that through scanning precession electron diffraction (SPED), detailed structural information can be extracted regarding crystal orientation over relatively large areas. This will be demonstrated for a ferroelectric *h*-$ErMnO_3$ polycrystal [1]. We will discuss how intensities in the diffraction patterns can be used to refine the structural analysis, increasing orientation precision and crystal description with the aim of mapping ferroelectric domains, even for grains in off-zone-axis crystal orientations.

For this work, a commercial scanning precession set-up on a standard 200 kV field emission transmission electron microscope along with a focus ion beam prepared lamella specimen are used. Our results will demonstrate the importance of precession of the electron beam and data collection using a direct electron detector. In the present work, the precession angle is limited to 1˚ to preserve sufficient spatial resolution. All analysis is done in open-source software, primarily the phyton library pyXem [2,3] and a home-made software for diffracted intensity analysis [3].

After pre-prossessing the stack of diffraction patterns, such as aligning the frames and background subtraction, an orientation map can be constructed using template matching where each experimental pattern is compared to a library of kinematically simulated patterns [4]. The ranking of the solutions is based on a normalized cross correlation. Figure 1(a) depicts the resulting orientation map with a model unit cell depicting the crystal orientation. We estimate the angular resolution of template orientation matching routine just below 1˚. The matching results can be used to calculate the component of the polar *c*-axis within the lamella plane. Furthermore, the angle between *c*-axis of adjacent grains and thereby the induced charging of a grain boundary due to the ferroelectric polarization in grains can be estimated.

# C.3

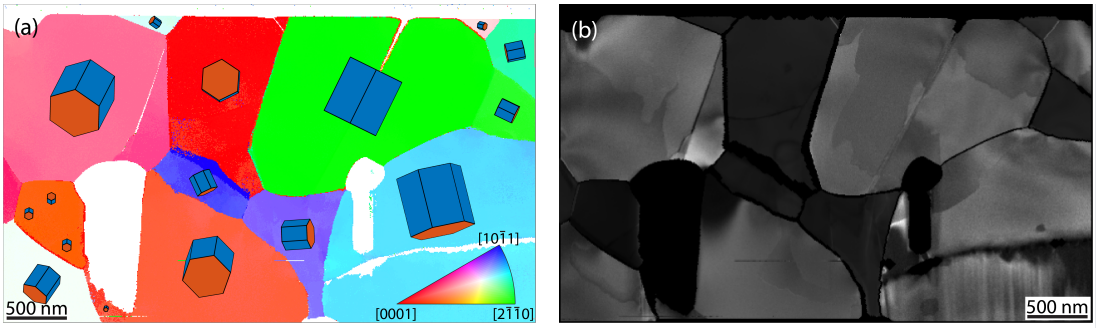


*Figure 1: (a) Orientation map (in beam direction) with model unit cells plotted on top of each grain. (b) Ensemble of manually constructed virtual dark-field images which depicts clear domain contrast for some grains.*

By capturing the SPED data at higher camera lengths, the strain and the polarization can potentially be analyzed [5]. However, in default template matching, and strain and field analysis, the information contained in the intensity variations of diffraction reflections is often disregarded. Using this valuable parameter can improve the structure analysis. For example, to deduce the polarization direction in the non-centrosymmetric structure, dynamical intensity variations between *g* and *-g* reflection pairs with a component along the polarization direction (*c*-axis) must be considered. Constructing virtual dark-fields from different grains reveals that domain specific intensity variations are present in the precession data (Fig.1(b)). In comparison, non-precessed beam data and conventional dark-field transmission electron microscopy have a weaker domain contrast, as dynamical intensity variations due to small orientation, thickness and strain variations across the grain can dominate overall contrast.

We will propose an analytical two-beam dynamic diffraction model to perform a quantitative analysis of diffraction intensities and refine the structural analysis with crystal orientation and specimen thickness as parameters [3]. In the present case, the aim is to deduce, beside the grain orientations, the polarization direction within a domain. Furthermore, the orientation and strain analysis might be improved compared to the initial analysis primarily based on the (relative) reflection positions. We will discuss why this quantitative refinement of crystal characteristics based on diffraction intensities can be applied for precession electron diffraction data. For ferroelectric materials simultaneous and accurate understanding of crystal orientation, strain and polarization is important. Moreover, scanning electron diffraction as preformed here has advantages compared to atomically resolved high-angle annular dark-field scanning transmission electron microscopy, routinely used for ferroelectrics. These advantages include a larger field-of-view, analyzing in off-zone orientations and significantly lowering the electron dose and are particularly beneficial in measuring structural details of polycrystalline ferroelectric materials.

Keywords

Ferroeelectrics, $ErMnO_3$, precession, diffraction, open-source

References

# C.3

[1] Schultheiß, J., Xue, F., Roede, E., Ånes, H. W., Danmo, F. H., Selbach, S. M., Chen, L.-Q., Meier, D., Confinement-Driven Inverse Domain Scaling in Polycrystalline ErMnO3. Adv. Mater., 34, 2203449, 2022. https://doi.org/10.1002/adma.202203449

[2] pyxem, DOI 10.5281/zenodo.2649351.

[3] Corrêa L., Ortega, E., Ponce A., Cotta M., Ugarte D. M., arXiv, 2023, https://doi.org/10.48550/arxiv.2301.10286.

[4] Cautaerts N., Crout P., Ånes H., Prestat E., Jeong J., Dehm G., Liebscher C. H., Ultramicroscopy, 237, 113517, 2022. Doi: 10.1016/j.ultramic.2022.113517

[5] Ophus C., Microscopy and Microanalysis, 25(3), 563-582, 2019. doi:10.1017/S1431927619000497

[6] Acknowledgements: NRF for support for NORTEM-facility (197405). LMC and DU thank support from CNPq, CAPES and FAPESP and DM acknowledges funding from the European Research Council (ERC) under the European Union's Horizon 2020 research and innovation program (Grant Agreement No. 863691).

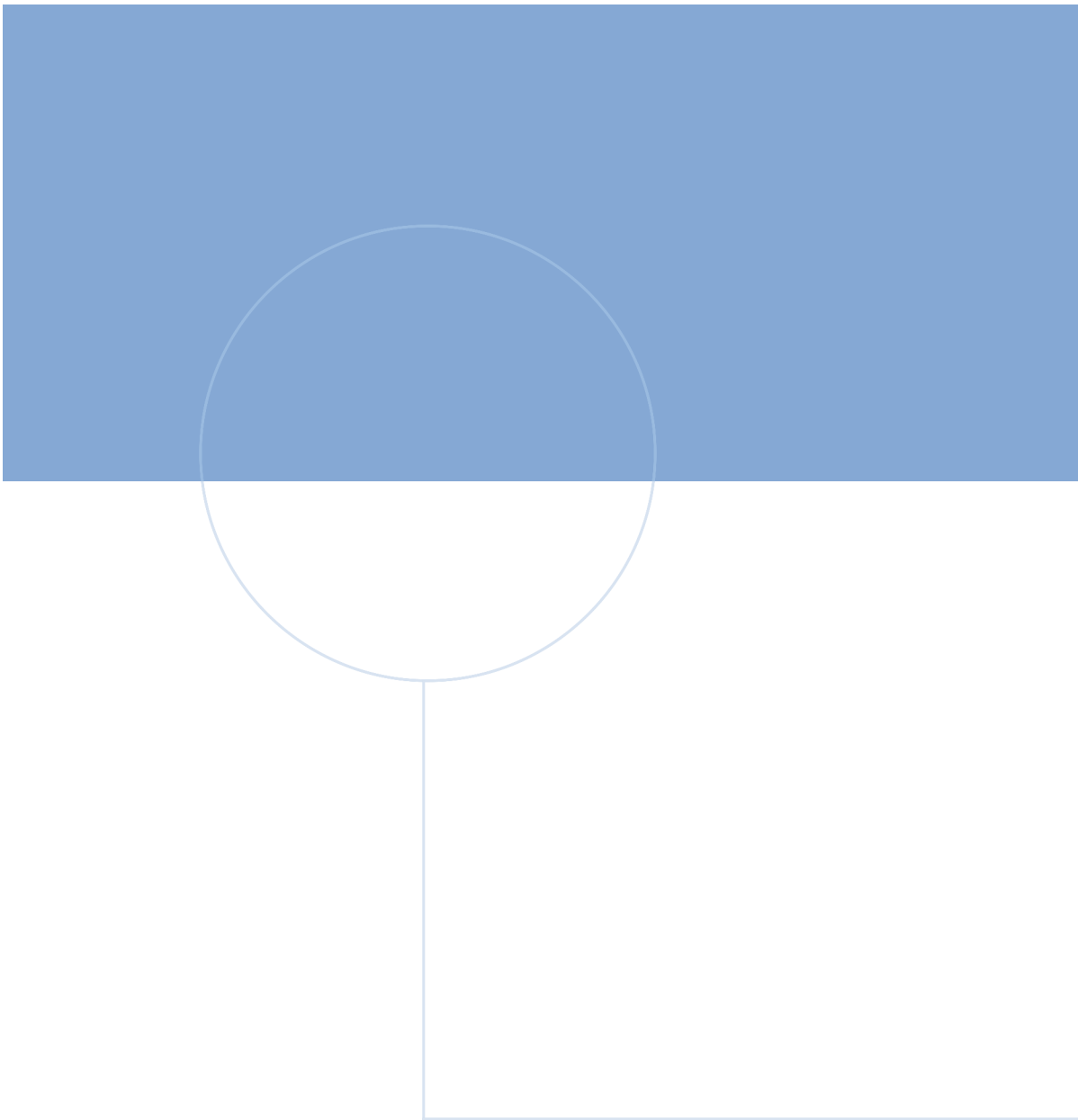

NTNU

Norwegian University of
Science and Technology